ANL-6581

Argonne National Laboratory

A STUDY OF VAPOR CARRYUNDER AND ASSOCIATED PROBLEMS

by

Michael Petrick

ANL-6581
Engineering and Equipment
(TID-4500, 17th Ed.)
AEC Research and
Development Report

ARGONNE NATIONAL LABORATORY
9700 South Cass Avenue
Argonne, Illinois

A STUDY OF VAPOR CARRYUNDER AND ASSOCIATED PROBLEMS

by

Michael Petrick

Reactor Engineering Division

July 1962

Operated by The University of Chicago
under
Contract W-31-109-eng-38

TABLE OF CONTENTS

	Page
NOMENCLATURE	7
ABSTRACT	11
I. INTRODUCTION	12
II. THEORETICAL ANALYSES	14
III. DIMENSIONAL ANALYSIS	29
IV. LABORATORY APPARATUS AND EXPERIMENTAL PROCEDURE	31
V. COMPARISON OF AIR-WATER DATA WITH THE THEORETICAL ANALYSIS	40
VI. EMPIRICAL CORRELATION OF CARRYUNDER DATA	48
ACKNOWLEDGEMENTS	61
APPENDICES	
A. Transport of Gas Bubbles through a Stagnant Fluid	63
B. Bubble Size and Distribution	71
C. Phase Distributions	84
D. Slip Ratios in Down Flow	105
BIBLIOGRAPHY	116

LIST OF TABLES

No.	Title	Page
I	Calculated and Measured Volumetric Entrainment Ratios . .	43
II	Data for Air-Water System	59
III	High-pressure Data	60
B-I	Average Bubble Size in the Riser and Flow Conditions Therein	82
B-II	Average Bubble Size in the Downcomer and Flow Conditions Therein	83
C-I	Phase Distributions and Flow Conditions for a Rectangular Section	86-97
C-II	Table of the Exponent m in Eq. (C-1) and Correlating Parameters for a Pressure of 14.7 psi	98
C-III	Phase Distributions and Flow Conditions in a Circular Pipe.	98
C-IV	Comparison of $\bar{\alpha}_{meas}$ Versus $\bar{\alpha}_{calc}$ for a Circular Section Using the Method of Haywood et al. and of Schwarz.	101
C-V	Table of Values for the Exponent m in Eq. (C-11) and Correlating Parameters (P = 600 psi)	102
C-VI	Comparison of Average Voids with Maximum and Center-line Voids	103
D-I	600-psi Downflow Slip Data	113
D-II	1000-psi Downflow Slip Data.	114
D-III	1500-psi Downflow Slip Data.	115

LIST OF FIGURES

No.	Title	Page
1.	Schematic of a Typical Separation Plenum	14
2.	Fluid Streamlines in the Separation Plenum for $A_D/A_R = 2$	15
3.	Fluid Streamlines in the Separation Plenum for $A_D/A_R = 1$	15
4.	Bubble Trajectory in Separation Plenum	16
5.	Trace Photograph of Separation Plenum	22
6.	Schematic of Air-Water Loop	31
7.	Air-Water Loop Pressure Tap Layout	32
8.	Schematic of High-pressure Loop	34
9.	Schematic of Power Supply for High-pressure Loop	35
10.	High-pressure Test Section	36
11.	High-pressure Downcomer Condenser	36
12.	A Gamma Intensity Versus Height Trace for Interface Determination	37
13.	Average Bubble Size Versus Terminal or Relative Gas Velocity	44
14.	Error Plot of the Predicted Versus Measured Volumetric Carryunder Ratio α_D/α_R	45
15.	Error Plot of the Predicted and Measured Weight Fraction Carryunder Ratio	46
16.	Effect of Interface Height on the Volumetric Carryunder	48
17.	Effect of Interface Height on the Weight Fraction Carryunder	49
18.	Effect of Temperature on Carryunder	49
19.	Effect of Superficial Downcomer Velocity on Carryunder	50
20.	Effect of Riser Quality on Carryunder	50
21.	The Weight Fraction Carryunder Ratio Versus V_g/V_{ent}	51
22.	Dimensionless Correlation of Air-Water Carryunder Data	52
23.	Nondimensionless Correlation of Air-Water Carryunder Data	53
24.	Effect of Power on the Weight Fraction Carryunder Ratio	54
25.	Effect of Superficial Downcomer Velocity on the Weight Fraction Carryunder Ratio	54

LIST OF FIGURES

No.	Title	Page
26.	Effect of Pressure on the Weight Fraction Carryunder Ratio	55
27.	Correlation of 600-psi Carryunder Data	55
28.	Correlation of 1000-psi Carryunder Data	55
29.	Correlation of 1500-psi Carryunder Data	56
30.	Dimensionless Correlation of High-pressure Data	56
31.	Nondimensionless Correlation of all Carryunder Data	57
A-1	Bubble Size Versus Bubble Velocity	68
A-2	Drag Coefficient as a Function of the Reynolds Number	70
B-1	Typical Bubble Photograph	72
B-2	Typical Bubble Photograph	73
B-3	Typical Bubble Photograph	73
B-4	Typical Bubble Photograph	74
B-5	Bubble Diameter Versus Quality in Riser	75
B-6	Bubble Diameter Versus Quality in Downcomer	75
B-7	Bubble Diameter Versus True Liquid Velocity	75
B-8	Enlarged Bubble Photograph (Magnification - 2.175)	76
B-9	Distribution of Bubble Sizes Obtained from Fig. B-8.	77
B-10	Normalized Bubble-size Distribution	77
B-11	C Versus $[(c^{c+1}e^{-c})/\Gamma(c+1)]$	79
B-12	Comparison of Measured Bubble Sizes and Correlation	80
B-13	Comparison of Measured Bubble Sizes and Correlation	80
B-14	Comparison of Measured Bubble Sizes and Correlation	81
B-15	Comparison of Measured Bubble Sizes and Correlation	81
B-16	Comparison of Measured Bubble Sizes and Correlation	82
C-1	Typical Phase Distribution in a Rectangular System	85
C-2	Effect of Void Fraction and Liquid Velocity on Slope m of Eq. (C-1)	99
C-3	Cross-sectional Diagram of Circular Conduit	100

LIST OF FIGURES

No.	Title	Page
C-4	Effect of Steam Volume Fraction and Liquid Velocity on Slope m of Eq. (C-11)	102
C-5	Variation of the Ratio $\bar{\alpha}/\bar{\alpha}_{CL}$ with $\bar{\alpha}$	104
D-1	Schematic of Loop Arrangement	106
D-2	Air-Water Slip Ratios Versus Superficial Downcomer Velocity	106
D-3	Air-Water Slip Ratios Versus True Downcomer Liquid Velocity	107
D-4	Slip Ratio Versus Superficial Downcomer Velocity at 600 psi	108
D-5	Slip Ratio Versus Superficial Downcomer Velocity at 1000 psi	108
D-6	Slip Ratio Versus Superficial Downcomer Velocity at 1500 psi	108
D-7	Slip Ratio Versus True Downcomer Velocity at 600 psi	109
D-8	Slip Ratio Versus True Downcomer Velocity at 1000 psi	109
D-9	Slip Ratio Versus True Downcomer Velocity at 1500 psi	109
D-10	Correlation of Down Flow Slip Ratio	111
D-11	Comparison Between the High Pressure Down Flow Slip Ratio Data and the Correlation	112

NOMENCLATURE

A	area
A_C	area from which carryunder emanates
A_{CH}	area from which carryunder emanates when $f^* < f$
b	constant in Poisson's distribution function
c	exponent in Poisson's distribution function
D	diameter
F	bubble flow
F_B	number of bubbles susceptible to entrainment
F_b	buoyant force
F_G	gravity force
F_{net}	net force
F_R	frictional force or resisting force
f	fractional distance in riser (Eq. 1)
f^*	fractional distance in riser (Eq. 40)
f_D	drag coefficient
G	mass velocity
g	gravitational constant
H	height of free surface above riser (interface height)
k_1	correction factor for height
k_2	correction factor for height
L	length
ℓ	variable distance into channel
N	number of bubbles
$N(R)$	bubble-size distribution function
n	number of bubbles in any interval
M	mass
m	exponent of void distribution function
p	pressure
P	constant in Poisson's distribution function
R	radius dimension
R_e	Reynolds Number

r	variable radius
$\bar{r}$	fluid streamline radius
s	channel spacing
t	time
V	velocity
W	flow rate
W_A	width of annular downcomer
X	quality
x	fractional distance of $\bar{r}_1$ from R_1
Y	half-length of chord
y	variable length of chord
z	distance from center of pipe to chord

α	void volume fraction
θ	angular dimension in the flow streamline
ρ	density
χ	radius of bubble
η	$(V_{L2} - V_0)/(V_{L1} + V_0)$
μ	viscosity
σ	surface tension

Subscripts

1	section of plenum where $\theta = 0$
2	section of plenum where $\theta = \pi$
3	section of plenum where $\theta = \pi/2$
B	bubble
b	buoyancy
c	critical
CF	cross flow
D	downcomer
ent	entrained
f	frictional

G	gravitational
g	gas
L	liquid
ℓ	variable length
max	maximum
o	terminal or final
R	riser
$\overline{r}$	fluid streamline radius
S	superficial
t	tangential
T	true
TP	two phase

A STUDY OF VAPOR CARRYUNDER AND ASSOCIATED PROBLEMS

by

Michael Petrick

ABSTRACT

A simple model for the carryunder phenomena is presented, and an analytical expression for the quality ratio X_D/X_R is derived. The dominating factor in this analysis is the definition of a specific area in the riser from which carryunder emanates. Data taken from an atmospheric air-water loop are compared with the predicted values for weight percent carryunder for the parameter range studied ($0.2 \times 10^{-3} < x < 2.0 \times 10^{-3}$, 1 ft/sec $< V_D <$ 2.5 ft/sec). The proposed model proved to be quite successful, and good agreement between measured and calculated values was obtained.

A dimensional analysis of the pertinent parameters affecting carryunder was also made, and a series of dimensionless groupings were derived. These groupings were then used to develop empirical correlations for predicting carryunder. The empirical correlation adequately represents a series of high-pressure data over the following parameter range: $0.1 < \alpha_R < 0.5$, $0.5 < V_D <$ 2.5 ft/sec, pressure = 600, 1000, 1500 psi, but the air-water data taken at atmospheric pressure deviate substantially. A nondimensionless empirical correlation, however, was developed for the X_D/X_R ratio, and the predicted values compared well with the data from both the atmospheric air-water and high-pressure loop. Fair agreement was obtained also with preliminary data taken with a large system (EBWR).

A series of appendices are included to provide information necessary for the development or utilization of the proposed correlations. The subjects covered in the appendices are: 1) bubble-size distribution ($0.01 \times 10^{-3} < x < 2.0 \times 10^{-3}$, 0.9 ft/sec $< V_s <$ 2.8 ft/sec); 2) bubble size versus bubble velocity relationship; 3) phase distributions within a conduit (1.15 $< V_s <$ 9.25 ft/sec, $0.0004 < x < 0.004$); and 4) downflow slip ratios (P = 600, 1000, and 1500 psi, $0.003 < x < 0.12$, 19 ft/sec $< V_s <$ 4.5 ft/sec). All data derived for the studies are tabulated.

I. INTRODUCTION

In a two-phase system in which the circulating coolant is boiled, it becomes increasingly difficult to achieve effective primary separation of the phases as the volumetric capacity of the system decreases and power density increases. When it is desired to effect this separation by purely natural means (such as gravity), the problem becomes acute. It is virtually impossible to effect a complete separation of the phases without the use of mechanical devices. A certain fraction of the vapor phase will be entrained in the downcomer with the recirculating liquid phase. The fraction of the vapor phase that is entrained in the downcomer is generally referred to as the percent carryunder.

In boiling systems in which the fluid flows by natural convection, the carryunder problem can become especially crucial. This stems from the fact that the recirculation flow rates are a function of the density difference existing between the upcomer (riser) and downcomer segments of the system. Should substantial quantities of vapor be entrained by the circulating fluid in the downcomer, the performance of the system could suffer significantly.

An excellent example of such a system would be a natural-circulation boiling water reactor. Steam carryunder can readily occur in this system because of high total power, geometric configuration of the internals, minimum coolant requirements, and limitations of pressure vessel size. Even though colder makeup water may be added at the top of the downcomer, it is conceivable that a substantial quantity of the entrained steam bubbles will not be collapsed immediately because of insufficient mixing. As a result, the net driving head and the flow rate would decrease, and the power level would drop. Similar detrimental results could occur in other two-phase systems where the circulating coolant is boiled, such as steam boilers, and evaporators. Forced-circulation systems could also be adversely affected, since excessive carryunder into the suction lines could lead to cavitation problems.

A schematic of a typical plenum in which the vapor-liquid separation process takes place is shown in Fig. 1. The two-phase mixture enters the plenum through a riser and the recirculating coolant leaves the plenum through the downcomer. The separation of the vapor phase from the liquid phase must, therefore, occur by means of buoyant and hydrodynamic forces in the time interval between entrance and discharge of the coolant into and from the plenum. The "average" time interval can be relatively long or short and is determined primarily by the physical dimensions of the system and by the volumetric flow of the vapor and liquid phases. There is virtually no information available which can be used for estimating the amount of carryunder that would be obtained in a given system for varying operating conditions. As a result, an analytical and experimental study was initiated to provide data on the magnitude of carryunder and to establish both quantitatively and qualitatively the effect of pertinent parameters.

Prior to initiating the experimental phase of the program, an analytical study of carryunder was made. During the study, it became apparent that rigorous analyses would be very difficult because of the complexity of the overall problem and the lack of pertinent general two-phase data in a number of associated problem areas. Therefore, the carryunder study was broken down into 5 separate, though interrelated, areas: (1) transport of gas bubbles through a liquid medium, (2) relation between bubble size and terminal velocity of the bubble, (3) bubble size and distribution, (4) gas- and liquid-phase distribution, and (5) slip ratios in downflow.

Each of these problem areas was then analyzed separately; available literature was searched for data, and, when no data were found, limited experimental studies were carried out to provide the minimal information desired. The pertinent information was then utilized in the development of the theoretical equation for the prediction of carryunder. The results of these studies are presented in the Appendices.

The experimental phase of the program was carried out with an atmospheric air-water loop and a high-pressure steam-water loop. The air-water studies were primarily aimed at establishing the pertinent parameters that affect the magnitude of carryunder. The purpose of the steam-water test was to determine the pressure effect on carryunder.

II. THEORETICAL ANALYSES

Consider a typical plenum, as depicted in Fig. 1, in which the vapor-liquid separation process occurs. The steam-water mixture enters the plenum through the riser, and the recirculating water and that portion of the vapor phase carried under discharge through the downcomer. It is readily apparent that the amount of vapor-phase entrainment that occurs should be sensitive to the flow path of the liquid phase. As a result, the first step in the analysis was a study of the fluid streamlines in a plenum. The analysis was made on on a pseudo-ideal, two-dimensional system, whereas the plenum is in fact an axisymmetrical three-dimensional geometrical arrangement. However, the results were thought to be indicative of the true fluid streamlines. The fluid streamlines were determined by an electrical potential analog. Basically, the method consisted of determining the equipotential lines on Teledeltos paper (paper of uniform resistivity).

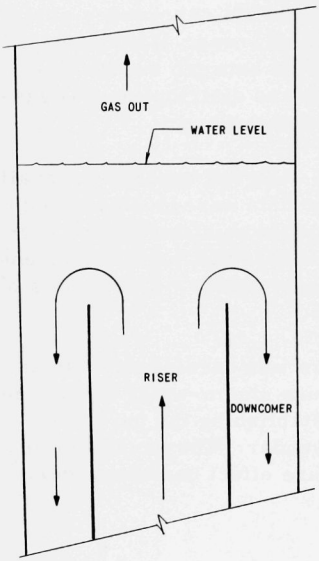

Fig. 1. Schematic of a Typical Separation Plenum

Figures 2 and 3 show the fluid streamlines that were determined for a plenum in which the area ratio between the downcomer and riser was 2/1 and 1/1, the true interface heights were $H = R/4$, $H = R$, $H = 2R$, and $H \to \infty$. As can be seen, there is very little change in the flow pattern beyond an interface height $H = 2R$. Also, the streamlines indicate that the liquid flowing out of the common riser into the downcomer follows circular-type paths. For the case in which $H \geq 2R$, the radius of the circular streamlines can be approximated by the following relationship:

$$\bar{r} = f(R_1 + W_A)/2 \quad , \tag{1}$$

where

R_1 = the radius of the riser

W_A = the width of the annulus downcomer

f = the fractional distance from the peripheral edge of the riser.

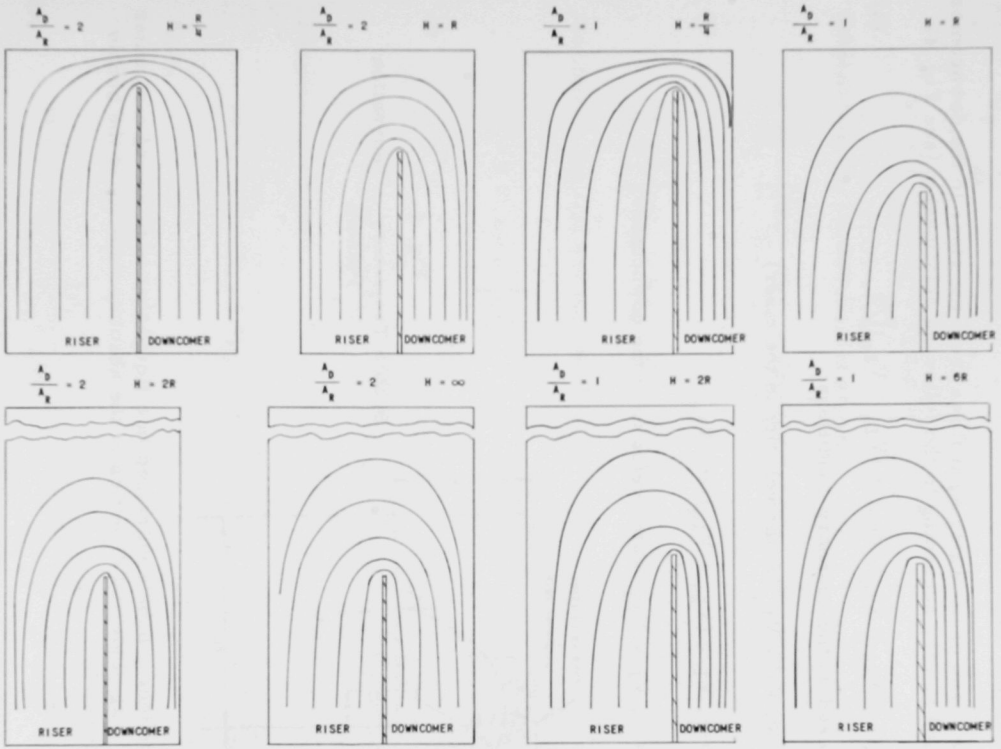

Fig. 2. Fluid Streamlines in the Separation Plenum for $A_D/A_R = 2$.

Fig. 3. Fluid Streamlines in the Separation Plenum for $A_D/A_R = 1$.

The center of the circle would then be located at a distance x from the riser wall, where

$$x = [f(R_1 - W_A)]/2 \quad . \tag{2}$$

The speed of the water as it flows from the riser to the downcomer was assumed to vary according to the following relationship (see Fig. 4):

$$V_L = \left[(V_{L_1} - V_{L_2}) \cos\theta + (V_{L_1} + V_{L_2})\right]/2 \quad , \tag{3}$$

which is based on the boundary conditions:

$\theta = 0$, $V_L = V_{L_1}$ (water velocity in the riser)

$\theta = \frac{\pi}{2}$, $V_L = (V_{L_1} + V_{L_2})/2 = V_{L_3}$

$\theta = \pi$, $V_L = V_{L_2}$ (water velocity in the downcomer) .

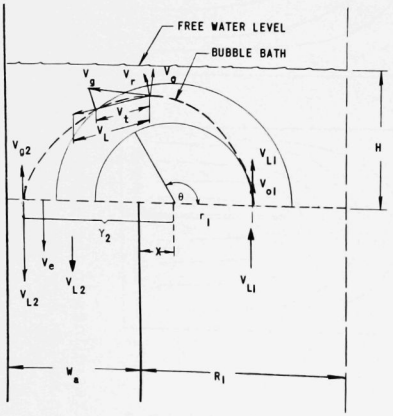

Fig. 4
Bubble Trajectory in Separation Plenum

Consider a bubble entrained in a liquid that is following a circular path. The magnitude and direction of the absolute velocity of the bubble are determined by

$$\vec{V}_g = \vec{V}_L + \vec{V}_0 \quad , \tag{4}$$

where $\vec{V}_0$ is the terminal velocity of the bubble. It is assumed that the terminal velocity is reached rather quickly. This assumption is based on the data of Miyagi[1] which shows that the vertical position at which the terminal velocity is attained is about 3 to 4 cm above the air-nozzle

discharge. The absolute velocity of the bubble considered has the following two components:

$$V_{\bar{r}} = \frac{d\bar{r}}{dt} = V_0 \sin \theta \tag{5}$$

$$V_t = \bar{r} \frac{d\theta}{dt} = V_L + V_0 \cos \theta \quad . \tag{6}$$

Substituting Eq. (3) into Eq. (6) yields

$$\bar{r} \frac{d\theta}{dt} = \left[(V_{L_1} - V_{L_2} + 2V_0) \cos \theta + (V_{L_1} + V_{L_2}) \right] \Big/ 2 \tag{7}$$

or

$$\frac{d\theta}{dt} = \frac{1}{\bar{r}} \left[(V_{L_1} - V_{L_2} + 2V_0) \frac{\cos \theta}{2} + V_{L_3} \right] \quad . \tag{8}$$

Combining Eqs. (5) and (8) one obtains

$$\frac{d\bar{r}}{d\theta} = \bar{r} V_0 \sin \theta \left[(V_{L_1} - V_{L_2} + 2V_0) \frac{\cos \theta}{2} + V_{L_3} \right]^{-1} \tag{9}$$

or

$$\frac{d\bar{r}}{\bar{r}} = V_0 \sin \theta \left[(V_{L_1} - V_{L_2} + 2V_0) \frac{\cos \theta}{2} + V_{L_3} \right]^{-1} d\theta \quad . \tag{10}$$

Integrating, we get

$$\ln \bar{r} = -2V_0 (V_{L_1} - V_{L_2} + 2V_0)^{-1} \ln \left[(V_{L_1} - V_{L_2} + 2V_0) \frac{\cos \theta}{2} + V_{L_3} \right] + C.$$

When

$$\theta = 0, \ \bar{r} = \bar{r}_1$$

$$\ln \bar{r}_1 = - \frac{2V_0}{V_{L_1} - V_{L_2} + 2V_0} \ln \left(\frac{V_{L_1} - V_{L_2} + 2V_0}{2} + V_{L_3} \right) + C \quad ,$$

since

$$V_{L_3} = (V_{L_1} + V_{L_2})/2$$

$$\ln \bar{r}_1 = - \frac{2V_0}{V_{L_1} - V_{L_2} + 2V_0} \ln \left(\frac{V_{L_1} - V_{L_2} + 2V_0 + V_{L_1} + V_{L_2}}{2} \right) + C$$

$$\ln \bar{r}_1 = \frac{-2V_0}{V_{L_1} - V_{L_2} + 2V_0} \ln (V_{L_1} + V_0) + C$$

$$C = \ln \bar{r}_1 + \frac{2V_0}{V_{L_1} - V_{L_2} + 2V_0} \ln (V_{L_1} + V_0)$$

$$\ln\left(\frac{\bar{r}}{\bar{r}_1}\right) = - \frac{2V_0}{V_{L_1} - V_{L_2} + 2V_0} \ln \left\{\left[(V_{L_1} - V_{L_2} + 2V_0) \frac{\cos \theta}{2} + V_{L_3}\right] \Big/ (V_{L_1} + V_0)\right\} .$$

Simplifying further

$$\frac{\bar{r}}{\bar{r}_1} = \left\{\left[(V_{L_1} - V_{L_2} + 2V_0) \frac{\cos \theta}{2} + V_{L_3}\right] \Big/ (V_{L_1} + V_0)\right\}^{-2V_0/(2V_0 + V_{L_1} - V_{L_2})} \quad (11)$$

$\theta = \pi$, $V_r = 0$.

It can be seen that when

$\theta = 0$, $\bar{r}_1 = \bar{r}_1$

$\theta = \pi/2$, $\bar{r}_3 = \bar{r}_1 \left[(V_{L_1} + V_{L_2})/2(V_{L_1} + V_0)\right]^{-2V_0/(2V_0 + V_{L_1} - V_{L_2})}$

$\theta = \pi$, $\bar{r}_2 = \bar{r}_1 \left[(V_{L_2} - V_0)/(V_{L_1} + V_0)\right]^{-2V_0/(2V_0 + V_{L_1} - V_{L_2})}$.

Consequently, the motion of the bubble can be considered to be analogous to the motion of a particle which is moving on a circular-type path with the tangential velocity component V_t varying according to the equation

$$V_t = \left[(V_{L_1} - V_{L_2} + 2V_0) \cos \theta + (V_{L_1} + V_{L_2})\right] \Big/ 2 \quad . \quad (12)$$

Thus, when

$\theta = 0$, $V_t = V_{L_1} + V_0 = V_{g_1}$, the gas velocity in riser

$\theta = \pi/2$, $V_t = (V_{L_1} + V_{L_2})/2 = V_{L_3}$, water velocity at $\theta = \pi/2$

$\theta = \pi$, $V_t = V_{L_2} - V_0 = V_{ent}$, entrainment velocity in downcomer .

The radial component of the bubble velocity is

$$V_{\bar{r}} = V_0 \sin \theta$$

and when

$\theta = 0$, $V_{\bar{r}} = 0$

$\theta = \pi/2$, $V_{\bar{r}} = V_0$

$\theta = \pi$, $V_{\bar{r}} = 0$.

The magnitude of the absolute velocity of the bubble is given by

$$V_g = \sqrt{V_t^2 + V_r^2} \quad ;$$

hence

$$V_g = \left\{ \left[\frac{V_{L_1} - V_{L_2} + 2V_0}{2} \cos\theta + \frac{V_{L_1} + V_{L_2}}{2} \right]^2 + \left[V_0 \sin\theta \right]^2 \right\}^{1/2} \quad , \qquad (13)$$

and when:

$$\theta = 0, \; V_g = V_{t_1} = V_{L_1} + V_0 = V_{g_1}$$

$$\theta = \pi/2, \; V_g = \left\{ \left[\frac{V_{L_1} + V_{L_2}}{2} \right]^2 + V_0^2 \right\}^{1/2} = \left(V_{L_3}^2 + V_0^2 \right)^{1/2}$$

$$\theta = \pi, \; V_g = V_{t_2} = V_{L_2} - V_0 = V_{ent} \quad .$$

The time-dependent equation of θ could be obtained by integrating the following equation, which is derived from a combination of the above equations:

$$\frac{d\theta}{dt} = \frac{\left\{ \left[(V_{L_1} - V_{L_2} + 2V_0) \cos\theta + (V_{L_1} + V_{L_2}) \right] / 2 \right\}^{1 + (2V_0 + V_{L_1} - V_{L_2})/2}}{\bar{r}_1 \, (V_{L_1} + V_0)^{2V_0/(2V_0 + V_{L_1} - V_{L_2})}} \qquad (14)$$

Entrainment Conditions

Suppose that a bubble following the above-described motion completed a 180° rotation and attained a speed $V_{ent} = V_{t_2} = V_{L_2} - V_0$ at the section $\theta = \pi$. If $V_{L_2} > V_0$, the bubble will be entrained with the speed $V_{ent} = V_{L_2} - V_0$; if $V_{L_2} < V_0$, the bubble will rise with a speed $V_g = V_0 - V_{L_2}$. Consequently for entrainment we must have $V_0 < V_{L_2}$. By means of Eq. (A-6) in Appendix A, the condition becomes

$$\sqrt{4(\rho_L - \rho_g) \, g \, D_0 / 3 \rho_L f_D} < V_{L_2}$$

or

$$D_0 < 3 f_D \rho_L V_{L_2}^2 / 4g(\rho_L - \rho_g) \quad . \qquad (15)$$

A second condition of entrainment is that the radius of the circular-type trajectory that the bubble follows, as given by Eq. (11), must fall within the downcomer annulus (see Fig. 4). Therefore,

$$\bar{r}_2 \leqq \frac{f(R_1 - W_A)}{2} + W_A \quad . \tag{16}$$

Substituting Eq. (1) into Eq. (11) with $\theta = \pi$,

$$r_2 \leqq \frac{f(W_A + R_1)}{2} \left[(V_{L_1} + V_0)/(V_{L_2} - V_0)\right]^{2V_0/(2V_0 + V_{L_1} - V_{L_2})} \quad . \tag{17}$$

Equating (16) and (17),

$$\frac{f(W_A + R_1)}{2} \left[\frac{V_{L_1} + V_0}{V_{L_2} - V_0}\right]^{2V_0/(2V_0 + V_{L_1} - V_{L_2})} = \frac{f(R_1 - W_A)}{2} + W_A \quad . \tag{18}$$

Equation (18) specified the second entrainment condition. When $V_0 = V_{L_2}$, Eq. (18) implies

$$f = 0 \quad .$$

Therefore, at the periphery of the riser, the maximum diameter of the bubble that will be entrained is given by Eq. (15). When $V_0 = 0$, Eq. (18) reduces to

$$f = 1 \quad ,$$

which satisfies the obvious condition that not even the bubble of smallest size emerging from the center of the riser can be carried under. Equation (18) thus establishes the relationship between the maximum critical bubble diameter, through the terminal velocity $\vec{V}_0$, which can be entrained and the position from which the bubble starts its motion. Unfortunately, Eq. (18) cannot be solved for V_0 and hence $D_c(f)$, the critical diameter as defined in Appendix A, since the relationship is not explicit in V_0. The expression is

$$V_0 = \frac{V_{L_2} - V_{L_1}\left[\dfrac{R_1 + W_A}{R_1 - W_A + 2W_A/f}\right]^{(2V_0 + V_{L_1} - V_{L_2})/2V_0}}{1 + \left[\dfrac{R_1 + W_A}{R_1 - W_A + 2W_A/f}\right]^{(2V_0 + V_{L_1} - V_{L_2})/2V_0}} \quad .$$

However, an explicit relationship can be obtained by solving Eq. (18) for f:

$$f = \frac{2W_A\left[(V_{L_2} - V_0)/(V_{L_1} + V_0)\right]^a}{W_A\left\{1 + \left[(V_{L_2} - V_0)/(V_{L_1} + V_0)\right]^a\right\} + R_1\left\{1 - \left[(V_{L_2} - V_0)/(V_{L_1} + V_0)\right]^a\right\}} , \quad (19)$$

where

$$a = 2V_0/(2V_0 + V_{L_1} - V_{L_2}) \quad .$$

Equation (19) can then be used in conjunction with the average bubble size and liquid velocities to calculate a pseudo area in the riser from which the carryunder emanates; that is, a point is reached, when one progresses from the periphery of the riser to its center, beyond which the average-sized bubble will not be carried under, since its trajectory exceeds the width of the annulus. The distance in from the riser edge where this occurs is

$$L_c = fR_1 \quad . \quad (20)$$

The "area" of the riser from which carryunder occurs is given by

$$A_c = \int_{R_1 - fR_1}^{R_1} 2\pi r dr \quad . \quad (21)$$

Therefore,

$$A_c = \pi R_1^2 (2f - f^2) = \pi R_1^2 [1 - (1 - f)^2] \quad . \quad (22)$$

Substituting Eq. (19) into Eq. (22) yields

$$A_c = \pi R_1^2 \left\{ 1 - \left[1 - \frac{2W_A\left(\frac{V_{L_2} - V_0}{V_{L_1} + V_0}\right)^a}{W_A\left[1 + \left(\frac{V_{L_2} - V_0}{V_{L_1} + V_0}\right)^a\right] + R_1\left[1 - \left(\frac{V_{L_2} - V_0}{V_{L_1} + V_0}\right)^a\right]} \right]^2 \right\} \quad . \quad (23)$$

A more rigorous analysis was believed to be unwarranted because of the fact that the calculation procedure would become unduly complex. It would be necessary to establish the critical bubble diameter versus

riser position relationship, by tedious trial-and-error techniques, and the fraction of the bubble population which exists below the critical diameters. Such analysis would be extremely time consuming and could not be justified because of the many uncertainties concerning the bubble-size distribution, buoyancy, velocity, water flow path, etc.

Some credulity is lent to the concept of a specific area of the riser from which the major portion of the carryunder occurs [as specified by Eq. (23)] by the photographs that were taken of a plenum during operation. In a typical photo, such as shown in Fig. 5, the circular-type trajectories of the bubble are readily apparent. These trajectories become wider and wider as they originate closer and closer to the center of the riser, intercept the wall of the plenum, and become engulfed in the large turbulent eddies existing near the surface. The major portion of the gas phase carried under appears to emanate from the peripheral region of the riser. A pattern of this type is predicted by Eq. (23).

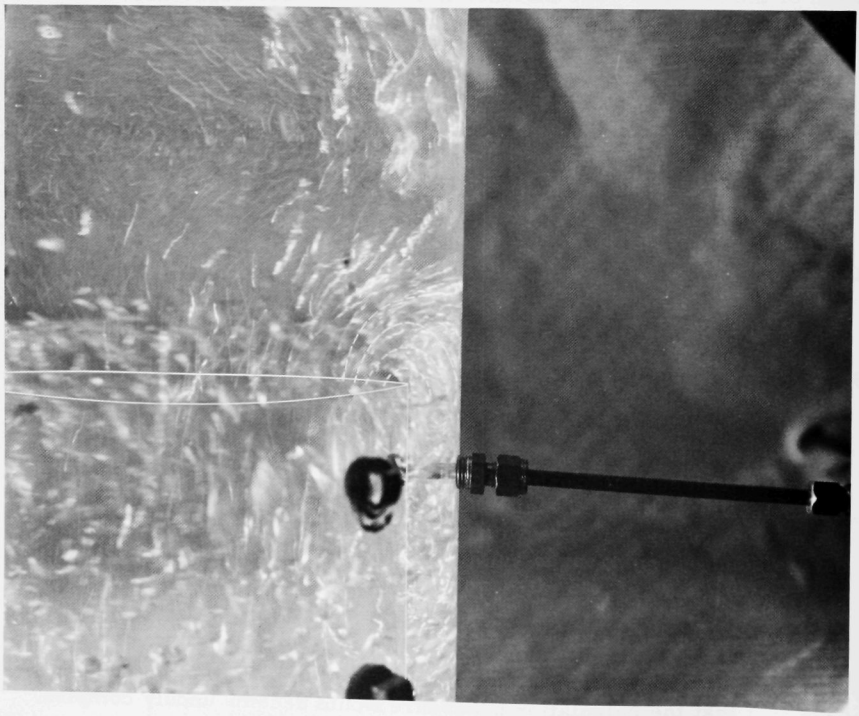

Fig. 5. Trace Photograph of Separation Plenum

Prediction of Carryunder

All bubbles having $D < D_c$ in that region of the riser specified by Eq. (23), will be entrained. If the water speed V_{L_2} at the inlet of the downcomer is known, the critical diameter D_c can be found by using Eq. (15) with the proper value of f_D or by using the proposed bubble velocity vs bubble diameter relationship that has been presented in Fig. A-1 of Appendix A. The latter relationship is used in this analysis. The fraction of the total number of bubbles that are susceptible to entrainment can then be calculated from the bubble-size distribution functions that are described in Appendix B. As discussed in Appendix B, the bubble-size distribution can be represented by Poisson's equation. Therefore, F_B, the number of bubbles susceptible to entrainment, can be represented by the equation

$$F_B = \frac{\int_0^{D_c/2} P(b\chi)^c \, e^{-b\chi} \, d\chi}{\int_0^{\infty} P(b\chi)^c \, e^{-b\chi} \, d\chi} \quad , \tag{24}$$

where χ is the bubble radius and the constants P, b, and c are functions of the liquid and gas mass velocity, void fraction, etc. They are given in Eqs. (B-17), (B-18) and (B-19) of Appendix B.

The volume of bubbles in a unit volume of riser is $\bar{\alpha}_R$; then, if χ_1 is the average bubble radius in the riser, the number of bubbles in this unit volume is

$$\frac{N}{ft^3} = \frac{\bar{\alpha}_R}{4\pi\chi_1^3/3} \quad . \tag{25}$$

The bubble flux is

$$\frac{N}{ft^2\text{-sec}} = \frac{\bar{\alpha}_R}{4\pi\chi_1^3/3} V_g \quad , \tag{26}$$

and the bubble flow is

$$\frac{N}{sec} = \frac{\bar{\alpha}_R}{4\pi\chi_1^3/3} V_g A \quad . \tag{27}$$

Therefore the bubble flow out from the region of the riser producing the carryunder is

$$F_1 = \frac{\bar{\alpha}_R V_{g_1} A_c}{4\pi\chi_1^3/3} \tag{28}$$

or, upon combining Eq. (23) with Eq. (28),

$$F_1 = \frac{\bar{\alpha}_R V_{g_1} R_1^2}{4\chi_1^3/3}\left\{1 - \left[1 - \frac{2W_A\,\eta^a}{W_A(1+\eta^a) + R_1\,(1 - \eta^a)}\right]^2\right\} \quad , \tag{29}$$

where

$$\eta = \left(V_{L_2} - V_0\right)\Big/\left(V_{L_1} + V_0\right)$$

and

$$a = 2V_0\Big/\left(2V_0 + V_{L_1} - V_{L_2}\right) \quad .$$

In Eq. (29), $\bar{\alpha}_R$ represents a mean void fraction across the entire riser. However, the void fraction is not a constant across the radius, as shown in Appendix C. The void distribution is affected by the liquid and gas mass velocities, mixture quantity, etc. The true mean void fraction in the riser region defined by Eq. (23) is therefore

$$\bar{\alpha}_C = \bar{\alpha}_R\,(\bar{\alpha}_C/\bar{\alpha}_R) \quad . \tag{30}$$

Assuming that the void distribution is described by the following relationship (See Appendix C):

$$\alpha_r = \alpha_{max}\left(\frac{R-r}{R}\right)^m \quad , \tag{31}$$

then

$$\frac{\bar{\alpha}_c}{\bar{\alpha}_R} = \left\{\frac{\int_{R_1-fR_1}^{R_1} 2\pi r\,\alpha_{max}\,[(R_1-r)/R_1]^m\,dr}{\int_{R_1-fR_1}^{R_1} 2\pi r\,dr}\right\}\Bigg/\left\{\frac{\int_0^{R_1} 2\pi r\,\alpha_{max}\,[(R_1-r)/R_1]^m\,dr}{\int_0^{R_1} 2\pi r\,dr}\right\} . \tag{32}$$

Equation (32) simplifies to

$$\frac{\bar{\alpha}_C}{\bar{\alpha}_R} = \frac{f^{(m+1)}\,[m+2 - f\,(m+1)]}{1 - (1-f)^2} \quad , \tag{33}$$

where f is given by Eq. (19) and m is given in Appendix C by Eq. (C-2). Therefore, the mean void fraction in the region of interest in the riser is

$$\bar{\alpha}_C = \frac{\bar{\alpha}_R f^{(m+1)} [m+2 - f(m+1)]}{1 - (1-f)^2} \quad . \tag{34}$$

The bubble flow from the carryunder-producing region in the riser becomes

$$F_1 = \frac{\bar{\alpha}_R f^{(m+1)} [m+2 - f(m+1)] R_1^2}{4\chi_1^3 [1 - (1-f)^2]/3} V_{g_1} \left\{ 1 - \left[1 - \frac{2W_A \eta^a}{W_A(1+\eta^a) + R_1(1-\eta^a)} \right]^2 \right\} . \tag{35}$$

The bubble flow in the downcomer is given by

$$F_2 = 3\alpha_D V_{g_2} (R_2^2 - R_1^2)/4\chi_2^3 \quad . \tag{36}$$

Therefore, the following equality must hold:

$$F_2 = F_B F_1 \quad ,$$

where F_B is the fraction of bubbles having $D < D_c$ as defined by Eq. (24). Consequently,

$$\frac{3\alpha_D V_{g_2}}{4\pi\chi_2^3} \pi(R_2^2 - R_1^2) = \frac{3V_{g_1}}{4\pi\chi_1^3} \bar{\alpha}_C A_C F_B \quad , \tag{37}$$

where α_C is defined by Eq. (34), A_C is defined by Eq. (23), and F_B is defined by Eq. (24). After solving for the downcomer void fraction, Eq. (37) becomes

$$\alpha_D = \left(\frac{\chi_2}{\chi_1} \right)^3 \frac{V_{g_1}}{V_{g_2}} \bar{\alpha}_C \frac{A_C}{A_D} F_B \quad , \tag{38}$$

where

$$A_D = \pi(R_2^2 - R_1^2) \quad .$$

Equation (38) states that the void fraction in the downcomer is a function of system geometry, bubble size in the riser and downcomer, the true gas velocity in the riser and downcomer, and the mean void fraction in the riser. Equation (38) is essentially valid only when the interface height is much greater than the riser diameter. When the interface height approaches a height equivalent to the riser diameter, Eq. (38) must be modified to include several competing height factors.

As the interface height continues to decrease, a point is reached where the trajectories of the gas bubbles begin to intercept the water interface in the plenum and escape. Therefore, a third entrainment condition must be specified, which takes into account the influence of the water level in the plenum in regard to the carryunder.

In order to make this entrainment condition somewhat simpler, one may define the third entrainment condition as follows: the radius r_3 of the bubble trajectory at $\theta = \pi/2$ has to be smaller than the interface height in the upper plenum or the bubble will escape (see Fig. 4). By defining the entrainment condition in this way, the carryunder will be underestimated because at $\theta = \pi/2$ the bubble has not yet reached its highest point. However, this difference in the heights is not very significant. From Eq. (11) one gets

$$r_3 = r_1 \left[\frac{V_{L_1} + V_0}{(V_{L_1} + V_{L_2})/2} \right]^{2V_0/(2V_0 + V_{L_1} - V_{L_2})} \leqq H \quad . \tag{39}$$

Defining

$$r_1 = \frac{f^* (R_1 + W_A)}{2} \quad , \tag{40}$$

Equation (39) becomes

$$f^* = \frac{H}{\left[(R_1 + W_A)/2\right] \left[2\left(V_{L_1} + V_0\right) \Big/ \left(V_{L_1} + V_{L_2}\right)\right]^{2V_0/(2V_0 + V_{L_1} - V_{L_2})}} \quad , \tag{41}$$

where f^* is the fractional distance from the riser periphery beyond which the trajectory of the average bubble will intercept the water surface and thus escape. Therefore, when $f^* < f$, which means that the area of the riser from which carryunder occurs becomes smaller due to the height effect, Eq. (38) must be multiplied by a factor k_1, which is defined as

$$k_1 = A_{CH}/A_C \quad , \tag{42}$$

where A_{CH} is the area from which carryunder emanates if $f^* < f$. The area A_{CH} is computed as follows:

$$A_{CH} = \int_{R_1 - f^* R_1}^{R_1} 2\pi r \, dr \quad . \tag{43}$$

Integrating Eq. (43) and substituting Eq. (41),

$$A_{CH} = \pi R_1^2 \left\{ 1 - \left[1 - \frac{H}{[(R_1 + W_A)/2]\left[2\,(V_{L_1} + V_0)/(V_{L_1} + V_{L_2})\right]^{2V_0/(2V_0 + V_{L_1} + V_{L_2})}} \right]^2 \right\} \qquad (44)$$

It should be noted that $f^* \leq f$ only when H becomes very small ($H \approx R_1$).

The second height factor, which is perhaps the more important, stems from the effect of the interface height on the average cross-flow velocity in the upper plenum. As can be seen in Figs. 2 and 3, the average cross-flow velocity starts to increase significantly below the position $H = 2R_1$. As a result, the bubble trajectories would tend to be shortened. The average cross-flow area is defined as

$$A_{CF} = 2\pi R_1 H \quad .$$

When $H < 2R_1$, the magnitude of the gas velocity is increased by the ratio $2R_1/H$ or D_1/H. Since the entrainment is proportional to the original gas velocity, an increase in entrainment would be expected in about the same ratio. Therefore, Eq. (38) must be multiplied by a factor k_2 when $H_T(1 - \alpha_R) < D_1$:

$$k_2 = D_1/H_T\,(1 - \alpha_R) \quad , \qquad (45)$$

where H_T is the true interface height.

The final form of Eq. (38) is, therefore,

$$\alpha_D = (\chi_2/\chi_1)^3\,(V_{g_1}/V_{g_2})\,\bar{\alpha}_C\,\frac{A_C}{A_D}\,F_B\,k_1\,k_2 \quad , \qquad (46)$$

where k_1 and k_2 are 2 correction factors to take into account the 2 opposite effects of height:

$$k_1 = \frac{A_{CH}}{A_C} = \frac{\text{Eq. (44)}}{\text{Eq. (23)}} \quad , \quad \text{to be used when } f^* < f;$$

$$k_2 = \frac{D_1}{H(1 - \alpha_1)} \quad , \quad \text{to be used when } H(1 - \alpha_1) < D_1 \quad .$$

Equation (46) can be transformed to give the percent carryunder (X_D/X_R) in the following manner. Since

$$V_{g_1}/V_{g_2} = \left[V_{L_1}/(1 - \alpha_R)\right]\left[(V_L/V_g)_R\,(1 - \alpha_D)/V_{L_2}\,(V_g/V_L)_D\right] \quad , \qquad (47)$$

Equation (46) becomes

$$\frac{\alpha_D}{\alpha_R} = \frac{V_{L_1}}{(1-\alpha_R)} \frac{(V_g/V_L)_R}{(V_g/V_L)_D} \frac{(1-\alpha_D)}{V_{L_2}} \left(\frac{\chi_2}{\chi_1}\right)^3 \frac{\bar{\alpha}_C}{\alpha_R} \frac{A_C}{A_D} F_B k_1 k_2 \quad . \tag{48}$$

Rearrangement yields

$$\frac{\alpha_D/(1-\alpha_D)}{\alpha_R/(1-\alpha_R)} = \left(V_{L_1}/V_{L_2}\right) \frac{(V_g/V_L)_R}{(V_g/V_L)_D} \left(\frac{\chi_2}{\chi_1}\right)^3 \frac{\bar{\alpha}_C}{\alpha_R} \frac{A_C}{A_D} F_B k_1 k_2 \quad . \tag{49}$$

Since

$$\frac{V_g}{V_L} = \left(\frac{X}{1-X}\right)\left(\frac{1-\alpha}{\alpha}\right)\left(\frac{\rho_L}{\rho_g}\right) \quad ,$$

it follows that

$$\frac{\alpha}{1-\alpha} = \frac{X}{(V_g/V_L)} \frac{\rho_L}{\rho_g} \tag{50}$$

when X is very small. Upon substituting Eq. (50) into Eq. (49) and also noting that

$$V_{L_1}/V_{L_2} = A_D/A_R \quad ,$$

Equation (49) becomes

$$\frac{X_D}{X_R} = \left(\frac{\chi_2}{\chi_1}\right)^3 \frac{\bar{\alpha}_C}{\alpha_R} \frac{A_C}{A_R} F_B k_1 k_2 \quad . \tag{51}$$

Equations (46) and (51) are compared with the air-water data in Section V.

III. DIMENSIONAL ANALYSIS

In addition to the preceding theoretical study, a dimensional analysis was also carried out on the carryunder problem. It was believed that such an analysis would produce significant dimensionless groupings which would be useful in the correlation of the data. It was assumed that the following group of variables affected the separation of the vapor and liquid in a typical plenum:

V_D = Liquid velocity in the downcomer, ft/sec

V_R = Liquid velocity in the riser, ft/sec

H = Height of the interface, ft

D = Diameter of the riser, ft

μ_L = Viscosity of the liquid, lb/(sec)(ft)

σ_L = Surface tension of the liquid, lb/sec^2

ρ_g = Density of the gaseous phase, lb/cu ft

ρ_L = Density of the liquid phase, lb/cu ft

V_{gR} = Gas velocity in the riser, ft/sec

V_{gD} = Gas velocity in the downcomer, ft/sec

W_R = Mass flow rate of the gaseous phase in the riser, lb/sec

W_D = Mass flow rate of the gaseous phase in the downcomer, lb/sec

W_T = Mass flow rate of the liquid phase, lb/sec

Any product Π of the above-listed variables has the following form:

$$[\Pi] = (W_R)^{k_1} (\rho_L)^{k_2} (\rho_g)^{k_3} (V_{gD})^{k_4} (V_{gR})^{k_5} (H)^{k_6} (D)^{k_7} (\sigma)^{k_8} (V_D)^{k_9}$$

$$(W_T)^{k_{10}} (\mu_L)^{k_{11}} (V_R)^{k_{12}} (W_D)^{k_{13}} \quad .$$

The corresponding dimension of Π is therefore

$$\left[\Pi\right] = \left[MT^{-1}\right]^{k_1} \left[ML^{-3}\right]^{k_2} \left[ML^{-3}\right]^{k_3} \left[LT^{-1}\right]^{k_4} \ldots\ldots \left[MT^{-1}\right]^{k_{13}} \quad .$$

In accordance with the properties of exponents,

$$\left[\Pi\right] = \left[M^{(k_1 + k_2 + k_3 + k_8 + k_{10} + k_{11} + k_{13})}\right]$$

$$\left[L^{(-3k_2 - 3k_3 + k_4 + k_5 + k_6 + k_7 + k_9 + k_{11} + k_{12})}\right]$$

$$\left[t^{(-k_1 - k_4 - k_5 - 2k_8 - k_9 - k_{10} - k_{11} - k_{12} - k_{13})}\right] \quad .$$

If Π is to be dimensionless, the exponents of M, L, T must then be zero. Therefore,

$$k_1 + k_2 + k_3 + k_8 + k_{10} + k_{11} + k_{13} = 0$$

$$-3k_2 - 3k_3 + k_4 + k_5 + k_6 + k_7 + k_9 - k_{11} + k_{12} = 0$$

$$-k_1 - k_4 - k_5 - 2k_8 - k_9 - k_{10} - k_{11} - k_{12} - k_{13} = 0 \quad .$$

The set of 3 equations contains 13 unknowns and, as a result, possesses an infinite number of solutions. Therefore, any value may be assigned to 10 unknowns and the resulting 3 equations may then be solved simultaneously. The following dimensionless products were obtained:

$$\Pi_1 = W_R/W_D \qquad \Pi_2 = \rho_L V_R W_D/\mu_L^2$$

$$\Pi_3 = \rho_g V_R W_D/\mu_L^2 \qquad \Pi_4 = V_D/V_R$$

$$\Pi_5 = V_R/V_{gR} \qquad \Pi_6 = H\mu_L/W_D$$

$$\Pi_7 = D\mu_L/W_D \qquad \Pi_8 = \sigma_L/\mu_L V_R$$

$$\Pi_9 = V_{gD}/V_{gR} \qquad \Pi_{10} = W_T/W_D \quad .$$

The above 10 groupings were then combined and the following dimensionless products were derived

$$\Pi_1' = (\Pi_1\, W_R/W_D)^{-1} = W_D/W_R = (W_D/W_T)/(W_R/W_T) = X_D/X_R$$

$$\Pi_2' = \Pi_2/\Pi_3 = \rho_L/\rho_g$$

$$\Pi_3' = \Pi_6/\Pi_7 = H/D$$

$$\Pi_4' = 1/\Pi_9 = V_{gR}/V_{gD}$$

$$\Pi_5' = 1/\Pi_4 = (V_R W_T)/(V_D W_T) = A_D/A_R$$

$$\Pi_6' = \Pi_8 = \sigma_L/\mu_L V_R$$

or

$$\frac{X_D}{X_R} = f\left(\frac{V_{gR}}{V_{gD}} \;,\; \frac{H}{D} \;,\; \frac{A_D}{A_R} \;,\; \frac{\sigma_L}{\mu_L V_R} \;,\; \frac{\rho_L}{\rho_g}\right) \quad .$$

The significance of these groupings in the correlation of the data is discussed in Section VI.

IV. LABORATORY APPARATUS AND EXPERIMENTAL PROCEDURES

The carryunder studies were carried out with 2 laboratory loops, an atmospheric air-water loop and a 200-psi steam-water loop. Each of these systems and the experimental procedures associated with them are described below.

Atmospheric Air-Water Loop

The air-water loop basically consisted of a water-circulation and air-injection system, a mixing chamber, a separation plenum, an air-water separator, and associated instrumentation. The experimental apparatus is schematically illustrated in Fig. 6.

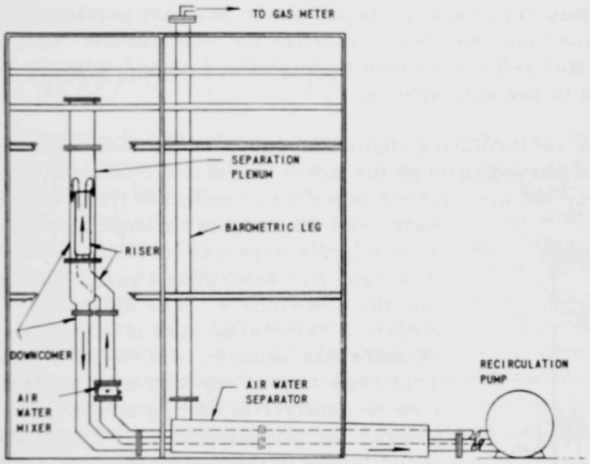

Fig. 6. Schematic of Air-Water Loop

Water was circulated through the loop by means of 2 turbine-type pumps having a total combined capacity of approximately 300 gpm. The water flow rate was regulated by means of a bypass system on the pump and metered by means of a calibrated orifice.

The air supply was obtained from the main laboratory 100-psi supply line. A constant pressure of 60 psi was maintained upstream of the air orifice by means of an air regulator. Immediately preceding the regulator was an air filter which removed excess moisture and foreign matter. The air flow rate was regulated by a series of 3 valves and measured by either of 2 calibrated orifices, 0.0961 and 0.2705 in. in diameter.

The air-water mixing chamber was constructed from 2 concentric pipes. The inner aluminum pipe, $5\frac{1}{8}$-in. ID x $12\frac{3}{16}$-in. long, included a mixing section, $6\frac{1}{8}$-in. long, containing 300 randomly distributed holes, each 0.06 in. in diameter. The outer pipe, 8 in. in diameter, was the annular plenum chamber through which high-pressure air was fed. The air was injected into the annular plenum through 3 openings located 120° apart to insure an equal distribution. This type of mixing chamber was used on other air-water loops and proved to be effective.

The separation plenum basically consisted of a Lucite tube placed within a second larger Lucite tube. The inner tube was the riser or upcomer. The annular region between the 2 tubes was the downcomer. The geometric parameters could be adjusted to any desired value by varying the tube diameters. The 2-phase mixture entered the plenum through the upcomer; this recirculating liquid phase and that portion of the gas phase carried under left the plenum through the downcomer. The gas phase that was separated left the plenum through the 2-phase mixture interface and discharged to the atmosphere.

The recirculating liquid and gas carried under left the separation plenum and passed through the lower downcomer into the air-water separator. Here the air carried under was separated from the recirculating water and discharged through a barometer leg into a cumulative-type gas meter, where the volumetric flow rate was determined before being discharged into the atmosphere. The air-water separator was merely a very large tank in which the liquid-phase velocity was reduced to a very low value (~0.2 ft/sec). This reduction of velocity allowed the gas phase to rise and collect at the top of the tank, from where it entered the barometric leg. The residence of the liquid phase in the separator was ~30 sec.

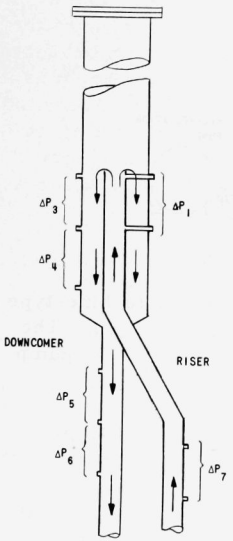

Fig. 7. Air-Water Loop Pressure Top Layout

The operating procedure followed was quite simple. The desired air and water flow rates were set and the loop allowed to come to equilibrium. The temperature of the recirculating water was followed closely and maintained by adjustment of the rate of flow of cooling water. Equilibrium was established when the fluid temperature and the flow rate of the gas phase carried under, measured on the gas meter, approached constant values. The desired data were then recorded. The mixture qualities in the riser and downcomer were obtained from the measured gas and liquid flow rates. The void fractions were calculated from differential pressure drops taken at strategic positions about the system, as shown in Fig. 7.

The differential pressure-drop readings were converted to void fractions in the following manner. For any system,

$$\Delta P_T = \Delta P_{acc} + \Delta P_H + \Delta P_f \quad .$$

Since the void fraction varied very little, if at all, in the regions where measurements were taken, the acceleration pressure drop, ΔP_{acc}, was essentially zero. Also, since the equivalent diameter of the conduits through which the fluid was flowing was quite large and because the velocity studied was quite small, it can be shown that the frictional pressure drop, ΔP_f, was also essentially zero. Therefore,

$$\Delta P_T = \Delta P_H = \left[(1 - \alpha)\, \rho_L + \alpha \rho_g \right] L = \rho_{TP} L \quad . \tag{52}$$

Solving for α gives

$$\alpha = \left[1 - (\rho_{TP}/\rho_L) \right] \Big/ \left[1 - (\rho_g/\rho_L) \right] \quad . \tag{53}$$

This procedure for determining the void fraction was corroborated by obtaining density traverses with a gamma source. The gamma-attenuation techniques utilized have been previously described.[2,3] Briefly, the equipment consisted of a thulium source, a photomultiplier tube with a thallium-activated, NaI scintillation crystal, a linear current amplifier, and a recorder. The gamma rays were directed through the test section to the photomultiplier tube, where the unattenuated portion of the beam produced a signal. The signal was amplified and sent to the recorder. The voids determined by this technique checked extremely well with those evaluated from the pressure-drop measurements. Because of the excellent agreement between the 2 methods and the tedium of the calculation by gamma attenuation, the use of the gamma system for void determination was discontinued midway through the study.

Data were taken over the following parameter ranges with the air-water loop:

Riser void fraction	α_R	0.1 - 0.50
Downcomer velocity	V_D	$\frac{1}{2}$ - $2\frac{1}{2}$ ft/sec
Riser quality	X_R	0.0002 - 0.003
Height of interface	H	4 in. - 19 in.
Area ratio between downcomer and riser	A_D/A_R	1.70

High-pressure Steam-Water Loop

The high-pressure loop is schematically illustrated in Fig. 8. Basically, this loop consisted of a heated section where the 2-phase

mixture was generated, a separation plenum similar to the one used on the air-water loop, a heat exchanger in the downcomer for measuring the quality of the mixture carried under, a make-up water system, and a steam condenser.

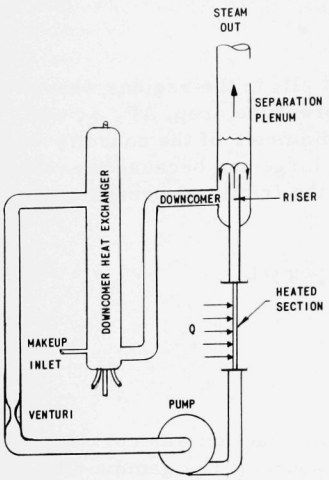

Fig. 8. Schematic of High-pressure Loop

Water was pumped from the makeup tank through the test section, where it was boiled. The 2-phase mixture then passed upward to the separation plenum, where the separation of the phases occurred by gravity. The steam that was separated left the separation plenum, was metered, condensed, and sent back to the makeup tank. The recirculation water and the steam carried under discharged through the annular downcomer to a heat exchanger where the mixture composition was determined by means of a heat balance. From the downcomer heat exchanger the fluid (now single phase) flowed to the suction side of the recirculating pumps.

Demineralized water was circulated through the loop by 100-gpm canned rotor pumps. There are 4 of these pumps available in the system with a combined capacity of 400 gpm. The water flow was regulated by air-operated control valves and a pump-bypass flow system.

The high-pressure loop was coupled to a 1500-kw dc power supply that was used for resistance heating of the test section. The metallic rectifier apparatus consisted of 4 oil-immersed, dc power supplies, 4 oil-to-air heat exchangers and associated oil pumps, a rectifier control cabinet, and external copper bus sections. Figure 9 shows these units in simplified block form as well as the main oil circuit breaker. Each of the power supplies was designated to deliver from 5,000 to 30,000 amp continuously and a maximum of 40,000 amp for one out of every 10 sec. The voltage ranged from 2 to 13 v. The 4 outputs could be connected in series, parallel, or series-parallel to deliver the following output: (1) parallel - 13 v at 120,000 amp; (2) series - 52 v at 30,000 amp; and (3) series-parallel - 26 v at 60,000 amp. The rectifier units operated from a 3-phase, 60-cycle, 12,800-v grounded neutral system. The oil was forced through the rectifier units and the heat exchangers to keep the operating temperature below 140°F, which is safely below the maximum permissible operating temperature of the selenium rectifier cells. The output power of the rectifier was manually controlled by means of a magnetic amplifier circuit. Current transducers are used to measure the output voltage of each unit and the total voltage applied to the load.

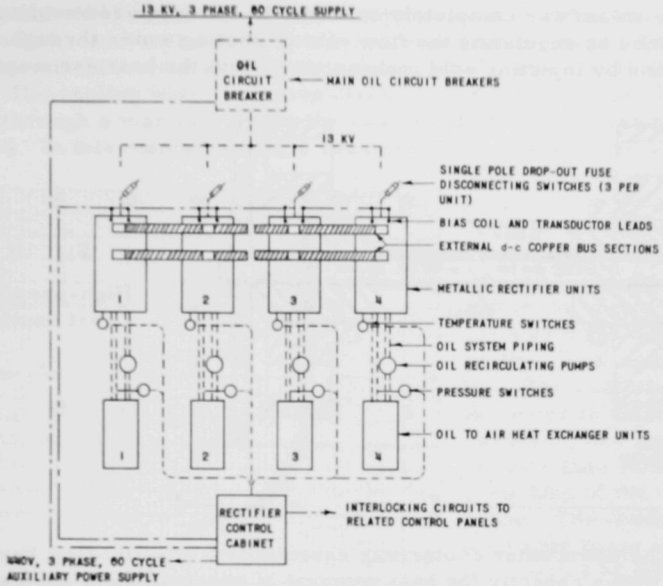

Fig. 9. Schematic of Power Supply for High-pressure Loop

The design of the test section was of a tube within a tube. The heated section consisted of a $1\frac{1}{2}$-in., schedule 40, $51\frac{5}{8}$-in. long, stainless steel pipe, the ends of which had brazed copper terminal plates. The heated section was inserted into and supported by a 2-in., schedule 80, stainless steel pipe. Prior to insertion, the heated section was wrapped with 2 thicknesses of a Durabla gasket material along the axial length. The function of the Durabla material was to insulate the inner tube electrically from the outer tube. The main function of the outer tube, as mentioned above, was to serve as the supporting member for the heated section. In this manner, the pressure range over which the section could be used was increased substantially. A drawing of the test section is presented in Fig. 10.

The separation plenum was basically the same as that employed in the air-water studies. The plenum was formed from a 6-in.-diameter, schedule 160, outer pipe with an internal 3.0-in.-diameter pipe acting as the upcomer or riser. The area ratio between the annular downcomer and the riser was 2:1. The steam-water mixture generated in the heated section entered the separation plenum through the upcomer. The steam which escaped from the plenum was discharged to the air-cooled condenser through a pressure-regulating valve. The steam carried under and the recirculating water were then passed through the downcomer heat exchanger,

where the steam was completely condensed. The required cooling capacity was obtained by regulating the flow rate of cooling water through the exchanger and by injecting cold makeup water into the heat exchanger.

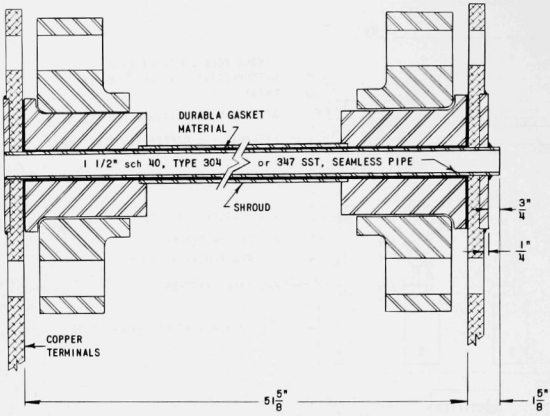

Fig. 10

High-pressure Test Section

The downcomer cooler was essentially a parallel-flow heat exchanger with a capacity for heat removal of approximately 230 kw. A drawing of the exchanger is given in Fig. 11.

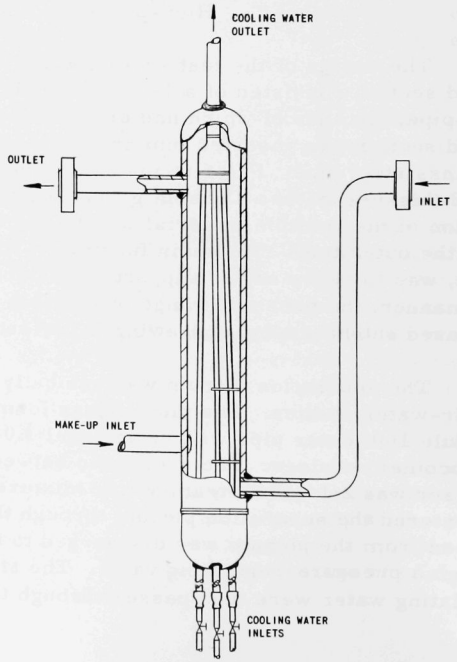

Fig. 11

High-pressure Downcomer Condenser

The external shell of the cooler was a 6-in., schedule 160, steel pipe, the ends of which were enclosed by two 6-in., schedule 160 caps. The cooling water entered the cooler through four $\frac{7}{16}$ -in. pipes, which were individually valved. The cooling water was then discharged through a 1-in. pipe after passing through a manifold inside the cooler, where the 4 streams were combined. In this manner a single reading of exit temperature was obtained. Also, such an arrangement provided for greater flexibility of operation. The recirculating loop water entered the cooler at the bottom through a 2-in. line, and was discharged through another 2-in. opening at the top. The residence time of the water in the cooler was approximately 5 sec, which is more than adequate for quenching of the vapor phase. The condensation of the vapor phase was followed by a series of differential pressure readings, which were taken along the length of the cooler.

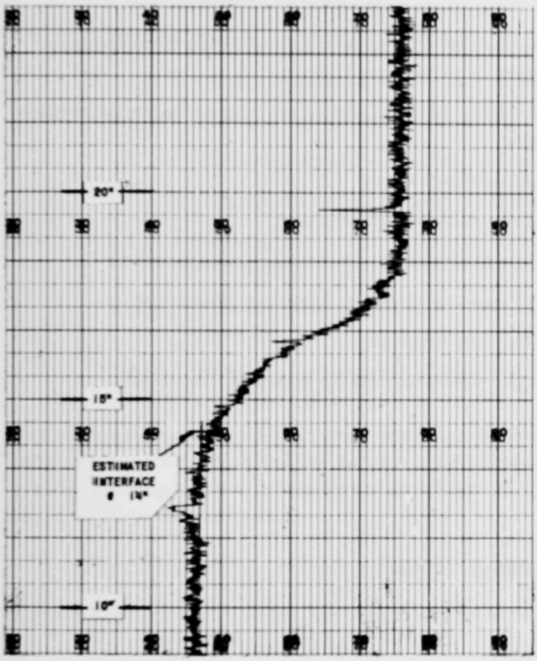

Fig. 12. A Gamma Intensity Versus Height Trace for Interface Determination

Briefly, the operating procedure was as follows. The loop was gradually brought to saturation conditions at the desired pressure. When saturation conditions were reached, the recirculating flow rate was adjusted to the desired value and the power was adjusted to yield the predetermined quality. The interface height was then varied slowly by creating an unbalance in the discharge rate of makeup water and steam. The true interface height was determined by employing a gamma traverse. The interface was considered reached when a sharp increase in gamma intensity was observed, as shown in Fig. 12. Concurrent with these operations, the cooling water to the downcomer heat exchanger was adjusted continually to provide an adequate subcooling margin of ~5°F. The loop was then allowed to stabilize completely. After equilibrium was established, the following data were recorded:

T_1 - inlet temperature of cooling water to downcomer heat exchanger

T_2 - outlet temperature of cooling water from downcomer heat exchanger

T_3 - inlet temperature to test section

T_4 - steam dome temperature

T_5 - inlet temperature of 2-phase mixture into downcomer heat exchanger

T_6 - outlet temperature of recirculating water in downcomer heat exchanger

T_7 - makeup-water temperature

ΔP_1 - differential pressure drop in riser

ΔP_2 - differential pressure drop in annular downcomer

ΔP_3 - differential pressure drop in annular downcomer

$P_{T.S.}$ - power input to test section

H_T - interface height determined by gamma traverse.

The quality of the 2-phase mixture entering the separation plenum through the riser, X_R, was obtained by a heat balance on the test section. If the heat losses, which were found to be negligible, were ignored, this balance is

$$3413\ P/3600 = W_T\ (\Delta h_{Sub} + X h_{fg}) \quad .$$

Rearrangement yields

$$X_R = \frac{(3413\ P/3600\ W_T) - \Delta h_{Sub}}{h_{fg}} \tag{54}$$

where

P = power delivered to test section, kw

W_T = recirculating flow rate, lb/sec

Δh_{Sub} = subcooling of liquid entering the heated section, Btu/lb

h_{fg} = latent heat of vaporization, Btu/lb.

The quality of the 2-phase mixture leaving the separation plenum through the downcomer, X_D, was calculated from a heat balance on the downcomer heat exchanger as follows:

$$(W_T - W_S - W_{cu})\, h_{sat} + W_s h_m + W_{cu} h_g = W_T h_{sub} + W_{cool}\,(h_{out} - h_{in}) + Q_{loss} \quad , \qquad (55)$$

where

W_T = total recirculating water flow rate, lb/sec

W_S = steam discharged from loop, lb/sec

W_{cu} = steam carried under in downcomer, lb/sec

W_{cool} = cooling water flow rates to heat exchanger, lb/sec

h_{sat} = saturation enthalpy, Btu/sec

h_m = makeup-water enthalpy, Btu/sec

h_g = saturated vapor-phase enthalpy, Btu/sec

h_{sub} = enthalpy of recirculating fluid leaving downcomer heat exchanger, Btu/lb

h_{out} = cooling-water enthalpy leaving downcomer heat exchanger, Btu/lb

h_{in} = cooling-water enthalpy entering downcomer heat exchanger, Btu/lb

Q_{loss} = heat loss from system between discharge points of downcomer and heat exchanger, Btu/sec.

Rearranging and defining,

$$W_{cu}/W_T = X_D; \quad h_{sat} - h_{sub} = \Delta h_{sub} \quad ,$$

and noting that $W_s = W_m$, Eq. (55) reduces to

$$X_D = \frac{(W_m/W_T)(h_{sat} - h_m) - \Delta h_{sub} + (W_{cool}/W_T)(h_{out} - h_{in}) + (Q_{loss}/W_T)}{h_{fg}} \quad . \qquad (56)$$

The steam volume fractions were again calculated from differential pressure-drop measurements as described for the air-water system and corroborated by gamma traverse where possible.

The parameter ranges studied with the high-pressure loop were

Riser void fractions	α_e:	$0.1 < \alpha_e < 0.50$
Pressures	P:	600, 1000, and 1500 psi
Downcomer velocities	V_D:	$0.5 < V_D < 2.5$ ft/sec
Interface heights	H:	$6 < H < 15$ in.
Downcomer to riser area ratios	A_D/A_R:	2

V. COMPARISON OF AIR-WATER DATA WITH THE THEORETICAL ANALYSIS

A comparison was made between the air-water data and Eqs. (46) and (51) of Section III to check the validity of the analysis. The entrainment volume fraction ratio α_D/α_R and the weight fraction ratio X_D/X_R were computed for approximately 30 runs and compared with the experimental values. The runs selected for comparison covered virtually the entire parameter range studied.

The following procedure was followed in computing the entrainment volumetric ratios as outlined in Section II:

1. In agreement with the assumed fluid behavior (see Section II), a mean fluid velocity $(V_{L_1} + V_{L_2})/2$ in the plenum was computed by averaging the true fluid velocities in riser and downcomer. By means of this mean fluid velocity, an average bubble diameter in the plenum was obtained from the bubble size vs true liquid velocity correlation described in Appendix B, Fig. B-7, and the corresponding value of the terminal bubble velocity was found from the proposed relationship for D_0 vs V_0 given in Appendix A, Fig. A-1.

2. Factors $\eta = (V_{L_2} - V_0)/(V_{L_1} + V_0)$ and $a = 2V_0/(2V_0 + V_{L_1} - V_{L_2})$ were then computed from the true fluid velocities in the riser and downcomer. From a knowledge of the geometrical dimensions of the riser and downcomer, W_A and R_1, the factor f was calculated from Eq. (19) of Section II.

3. The expression for the area ratio A_C/A_D is given in Section II, Eq. (23), and was calculated from the factor f and the geometrical dimensions of the system.

4. The quantity $\bar{\alpha}_C/\bar{\alpha}_R$ was computed from Eq. (34) in Section II. The exponent m is given by Eq. (C-2) in Appendix C and requires only that the true liquid velocity and void fraction in the riser be determined.

5. The equation for F_B, the total number of bubbles that are susceptible to entrainment, as given by Eq. (24) in Section III, can be rewritten by inserting the expressions for the constants P, b, and c of Eqs. (B-17), (B-18), and (B-19) of Appendix B as follows:

$$F_B = \int_0^{D_C/2} \frac{B}{\Gamma(c+1)} (bR)^c e^{-br} \, dR \quad , \tag{57}$$

where D_C represents the critical bubble diameter, i.e., the diameter of the maximal size bubble which can be entrained.

If $bR = v$ and $c = p_1$, Eq. (57) becomes

$$F_B = \int_0^{bD_c/2} \frac{1}{\Gamma(p_1+1)} (v)^{p_1} e^{-v} dv \quad . \tag{57a}$$

By substituting $u_1 \sqrt{p_1+1}$ for the upper limit of the integral, one obtains

$$F_B = \int_0^{u_1\sqrt{p_1+1}} \frac{(v)^{p_1} e^{-v}}{\Gamma(p_1+1)} dv = I_1(u_1, p_1) \quad , \tag{57b}$$

where $I_1(u_1, p_1)$ represents an incomplete Gamma Function with the parameters

$$u_1 = bD_c/2\sqrt{p_1+1}\,; \quad p_1 = c \quad . \tag{57c}$$

The critical bubble diameter D_c is determined by the first entrainment condition. This condition states that only bubbles having a terminal velocity smaller than the true liquid velocity in the downcomer can be entrained. So, by means of the true liquid velocity in the downcomer as an upper limit, the critical bubble diameter can be obtained from the proposed relationship bubble size versus terminal bubble velocity as given in Appendix A, Fig. A-1.

The proper values of the incomplete gamma function are tabulated as functions of the parameter u and p in Ref. (4).

6. In order to compute the radii ratio $(\overline{X}_1/\overline{X}_2)^3$ it is necessary to determine the average bubble radius in the riser and upper downcomer. By means of bubble size distribution, as described in Appendix B, the average bubble radius $\overline{X}$ in the riser is given by

$$\overline{X}_1 = \int_0^\infty \frac{b}{\Gamma(c+1)} (bR)^c e^{-bR} R\, dr \Bigg/ \int_0^\infty \frac{b}{\Gamma(c+1)} (bR)^c e^{-bR} dR \quad . \tag{58}$$

To be correct, the upper limit of the integral should be R_{max}, the largest bubble radius found. To simplify the computation, infinity was used as the upper limit. This simplification does not introduce any significant error, since the distribution function approaches zero very rapidly for $R > R_{max}$.

Substituting $bR = t$ and noting that

$$\Gamma(c+1) = \int_0^\infty t^c e^{-t}\, dt$$

$$\Gamma(c+2) = \int_0^\infty t^{c+1} e^{-t}\, dt \quad ,$$

Eq. (58) yields

$$\overline{\chi}_1 = \Gamma(c+2)/b\Gamma(c+1) \quad . \tag{58a}$$

Similarly, the average bubble radius $\overline{\chi}_2$ in the upper downcomer becomes

$$\overline{\chi}_2 = \int_0^{D_c/2} \frac{b}{\Gamma(c+1)} (bR)^c e^{-bR} R\,dR \Bigg/ \int_0^{D_c/2} \frac{b}{\Gamma(c+1)} (bR)^c e^{-bR}\, dR \quad . \tag{59}$$

Here the upper limit of the integrals is again the critical bubble radius as defined by the first entrainment condition in Section III. Therefore, the denominator yields $I_1(u_1, p_1)$, as shown in item 5. By means of the same procedure as before, the numerator proves to be

$$\frac{\Gamma(c+2)}{b\Gamma(c+1)} I_2(u_2, p_2) \quad , \tag{59a}$$

where $I_2(u_2, p_2)$ again stands for an incomplete gamma function with the parameters

$$u_2 = \frac{bD_c/2}{\sqrt{c+2}} \; ; \qquad p_2 = c + 1 \quad . \tag{59b}$$

Therefore, the average bubble radius $\overline{\chi}$, reduces to

$$\overline{\chi}_2 = \frac{\Gamma(c+2)}{b\Gamma(c+1)} \frac{I_2(u_2, p_2)}{I_1(u_1, p_1)} \quad , \tag{59c}$$

and the radii ratio $(\overline{\chi}_2/\overline{\chi}_1)$ simplifies to

$$\overline{\chi}_2/\overline{\chi}_1 = I_2(u_2, p_2)/I_1(u_1, p_1) \quad , \tag{60}$$

where the expressions for the parameter u_1, u_2, p_1, and p_2 are given in Eqs. (57c) and (59b).

7. The factors k_1 and k_2, which take care of the height effects, were found to be negligible for the parameter range studied (interface height 7 and 15 in.).

The calculated volumetric entrainment ratios for the 30 runs are compared with the measured values in Table I.

Table I

CALCULATED AND MEASURED VOLUMETRIC ENTRAINMENT RATIOS

H, in.	W_{H_2O}, lb/sec	$(W_{Air})_R$ ft/sec	V_R, ft/sec	V_D, ft/sec	α_R	α_D	α_D/α_R	
							Meas	Calc
15	15.422	0.02362	1.503	0.917	0.3135	0.211	0.6733	1.3318
7	15.422	0.02362	1.503	0.917	0.3137	0.2738	0.8618	1.2346
15	15.422	0.03161	1.503	0.917	0.3720	0.2404	0.6462	1.9409
7	15.422	0.03161	1.503	0.917	0.3720	0.2822	0.7586	1.7048
15	21.841	0.00462	2.128	1.299	0.0732	0.1411	1.9289	0.4317
7	21.841	0.00462	2.128	1.299	0.0752	0.1630	2.1676	0.3258
15	21.919	0.01346	2.136	1.304	0.1881	0.1797	0.9553	0.9580
7	21.702	0.01361	2.115	1.291	0.1933	0.1965	1.0166	1.1278
15	21.702	0.02240	2.115	1.291	0.2675	0.2017	0.7540	1.3337
7	21.702	0.02240	2.115	1.291	0.2717	0.2497	0.9190	1.4452
15	21.702	0.03341	2.115	1.291	0.3250	0.2289	0.7043	1.5289
7	21.702	0.03341	2.115	1.291	0.3302	0.2289	0.7817	1.5669
15	21.702	0.04279	2.115	1.291	0.3678	0.2445	0.6648	1.6340
15	28.129	0.00565	2.741	1.673	0.0690	0.1108	1.6058	0.8113
7	28.129	0.00565	2.741	1.673	0.0752	0.1233	1.6396	0.8194
15	28.129	0.01711	2.741	1.673	0.1986	0.1777	0.8947	1.2944
7	28.129	0.01711	2.741	1.673	0.1965	0.2132	1.0851	1.2316
15	28.129	0.0287	2.741	1.673	0.2529	0.1965	0.7769	1.3749
7	28.129	0.0287	2.741	1.673	0.2633	0.2362	0.8986	1.3144
15	28.129	0.04291	2.741	1.673	0.3093	0.2257	0.7297	1.4340
7	28.129	0.04291	2.741	1.673	0.3093	0.2362	0.7635	1.4088
15	21.70	0.00457	2.115	1.291	0.0804	0.1350	1.6791	0.3482
7	21.83	0.00457	2.127	1.298	0.0825	0.1790	2.1697	0.3947
15	21.88	0.01322	2.132	1.301	0.1771	0.2050	1.1582	0.9282
7	21.51	0.01344	2.096	1.279	0.1820	0.2520	1.3846	0.9482
15	21.64	0.02249	2.109	1.278	0.2480	0.227	0.9153	1.2308
7	21.55	0.02249	2.100	1.282	0.2570	0.262	1.0194	1.2302
15	21.65	0.03392	2.110	1.288	0.3150	0.257	0.8195	1.4014
7	21.81	0.03392	2.125	1.297	0.3170	0.306	0.9653	1.3018
15	21.79	0.04314	2.123	1.296	0.3520	0.284	0.8068	1.4304

The agreement between the experimental and predicted values of entrainment was good only over a very limited parameter range, namely, the medium riser void volume fraction and velocity range. Sharp deviations between the calculated and measured values were obtained in the low and high ranges of void volume fraction.

The major uncertainty in the analysis was the choice of the proper terminal velocity versus bubble size relationship, which is described in Appendix A. The calculated volume fraction ratio of entrainment void is extremely sensitive to the buoyancy velocity V_0. Small changes in V_0

produce large variations in the final calculated results. The quantities f_1, $\bar{\alpha}_c/\bar{\alpha}_R$, A_c, $(V_{L_1} + V_0)/(V_{L_2} - V_0)$, and $2V_0/(2V_0 + V_{L_1} - V_{L_2})$ all are affected. The use of the proposed bubble velocity-size relationship in the analysis is certainly questionable. As assumed in Appendix A, this relationship was developed from data obtained with systems for which the rise of a single bubble in a stagnant fluid was studied. It would, indeed, be surprising if the same relationship would apply when a large number of bubbles are moving in a flowing fluid. An attempt was made to develop a bubble velocity versus bubble size correlation which would be applicable to such a system. The true gas velocities were computed from the measured void volume fractions and were then coupled to the proper bubble size by utilizing the bubble size versus true liquid velocity correlation described in Appendix B. The curve derived in this manner is shown in Fig. 13. As is shown, the bubble velocity increases as the bubble size decreases, which relationship differs substantially from the correlation derived for the rise of single bubbles in a stagnant fluid where the bubble velocity increases as the bubble size increases. This apparently contradictory relationship results from the unique characteristics of 2-phase flow. It has been shown in Appendix B that, as the true liquid velocity increases, the bubble size decreases. Also, as the true liquid velocity increases the pressure drop increases. One can then postulate that the gas phase is then accelerated to maintain a constant pressure drop for each phase.

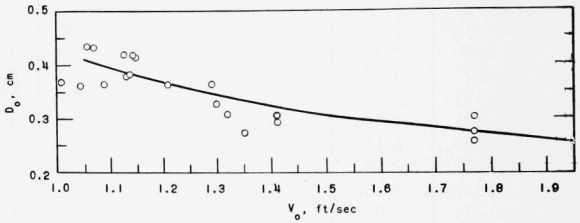

Fig. 13. Average Bubble Size Versus Terminal or Relative Gas Velocity.

A study of photographs and a visual observation indicates that the term $\bar{\alpha}_c/\bar{\alpha}_R$ in the analysis was likewise subject to question. The void fraction $\bar{\alpha}_c$ did not appear to decrease markedly near the riser wall at the riser exit as Eq. (34) would predict. In fact, at times it appeared that the gaseous phase tended to concentrate there. A study of the fluid streamline and velocity gradients near the top of the riser and downcomer, as shown in Figs. 2 and 3, also suggests that the void fraction near the riser wall should not drop abruptly. The fluid streamlines bend toward the riser wall, and the velocity increases as the fluid completes the 180° turn from riser to downcomer. The velocity profile was essentially dependent on the distance from the riser wall, and a strong velocity gradient was established in this region. Bankhoff[5] has proposed that the voids

tend to migrate toward the region of the highest velocity because of the Bernoulli force on the bubble. Such a process would account for the void profiles that have been shown to have the highest void fraction in the center of the conduit in the region of high velocity. Similarly, at the riser exit, one would expect the voids to migrate to some extent to the peripheral region of the riser and thus flatten the void distribution across the conduit. Since the magnitude of this effect was unknown, the ratio $\bar{\alpha}_c/\bar{\alpha}_R$ was set equal to unity.

The entrainment ratios were then recalculated by means of the buoyancy velocities obtained from Fig. 13 to evaluate the factors η, a, f, and A_c/A_D. The remaining factors were computed as described previously except for the ratio $\bar{\alpha}_c/\bar{\alpha}_R$. The agreement between the measured and calculated values improved markedly with these modifications and, in fact, may be considered good over a substantial range of the parameters studied. A comparison is given in Fig. 14 by means of an error plot. The calculations showed that the carryunder emanated from the extreme peripheral region of the riser. This was confirmed by visual observations during actual tests and by trace photographs of the type shown in Fig. 5. The points that do deviate widely are subject to question. The 6 points that have a much lower calculated value of the α_D/α_R ratio than measured are representative of very low riser void fractions. They may be in error because of a distorted void distribution. As mentioned previously, the air was introduced into the riser by means of a peripheral injection system. For a very low air rate it was observed that the air tended to remain at the periphery. Such a distribution could lead to excessive carryunder. The 4 data points for which calculated values were much too high covered conditions for which the downcomer velocity was low and was almost equal to the bubble buoyancy velocities. Under such conditions, the slip ratios were extremely low and their accuracy was extremely sensitive to measured void fractions, which are then reflected in the velocity ratio V_g/V_{ent}. As discussed in Appendix D, it is

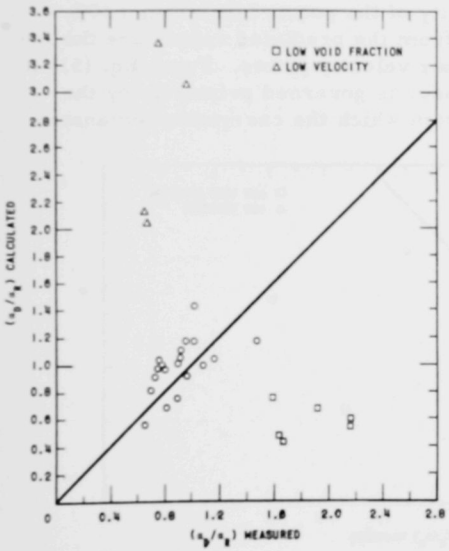

Fig. 14. Error Plot of the Predicted Versus Measured Volumetric Carryunder Ratio α_D/α_R

believed that the measured void fractions in this range may be in error. It was observed that under these conditions some of the air escaped as a result of coalescence after having been entrained. This could lead to abnormally high void fractions and then to excessively low slip ratios and high velocity ratios. Abnormally high velocity ratios V_g/V_{ent} were obtained for these points, so that the calculated values of $\bar{\alpha}_D/\bar{\alpha}_R$ were extremely high and are subject to question.

The percent carryunder by weight was then calculated by means of Eq. (51) with the above-mentioned modifications.

Good agreement between the calculated and measured values of the quality ratio X_D/X_R was obtained. The comparison is shown by means of an error plot in Fig. 15. The majority of the points fall within ±20%. Again, the data that deviate greatly from the predicted values are the low riser void fraction and low downcomer velocity points. From Eq. (51) it can be seen that the percent carryunder is governed primarily by the factor A_C, which is the riser area from which the carryunder emanates.

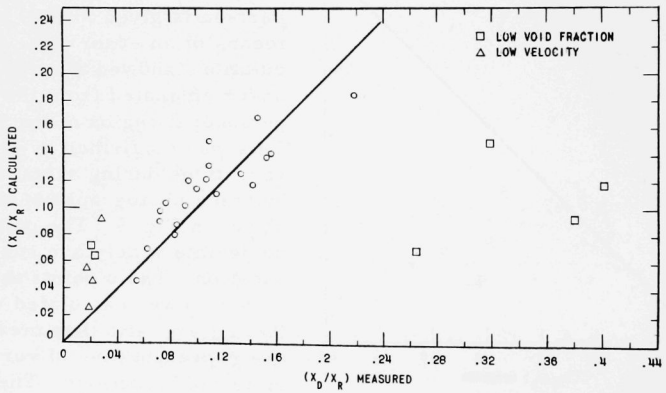

Fig. 15. Error Plot of the Predicted Versus Measured Weight Fraction Carryunder Ratio

The good agreement obtained between the predicted and measured values suggest that the proposed highly simplified carryunder model does describe the actual physical conditions existing in the plenum; however, its validity is far from established. Additional tests and data are needed with widely varying geometrical arrangement and extended parameter ranges so that the effectiveness of the model may be judged more certainly. Aside from the desired objective of predicting the carryunder, the analysis proved extremely helpful in outlining the pertinent parameters in the study of the carryunder problem and aided considerably in the empirical correlation of the data.

No attempt was made to compare the analysis with the high-pressure data because of the lack of information on the actual bubble size, phase distribution in the pipe, bubble size versus terminal velocity relationship, etc., at the increased temperatures and pressures.

VI. EMPIRICAL CORRELATION OF CARRYUNDER DATA

The discussion of the empirical correlations and trends which were obtained from the carryunder data is presented in 2 sections: (1) air-water, and (2) steam-water studies. The air-water study was run primarily to study the effects of the various system variables, such as downcomer velocity, mixture quality, interface height, and system temperature. Each of these parameters was varied individually while holding the remaining parameters constant. Data were then taken with the high-pressure steam-water loop to study the effects of pressure and fluid properties.

Air-Water Study

The first series of air-water tests were run to study the effects of interface height on carryunder. The liquid and gas flow rates were set and then the interface height was varied from H/D = 4 to H/D = 0.75. For each steady-state setting, the volumetric ratio of carryunder and the weight fraction of carryunder were measured. The procedure was repeated for a series of air and water flow rates until a substantial cross section of the voids and velocity ranges was covered. Typical results from these tests, in which the downcomer velocity was held constant, are shown in Figs. 16 and 17. Volumetric carryunder and weight fraction carryunder ratios are plotted as a function of the interface height and, as can be seen, a family of curves is obtained for the varying qualities. The volumetric carryunder ratio is defined as α_D/α_R, where α_D is the void volume fraction in the downcomer and α_R is the void volume fraction in the riser. The weight fraction carryunder ratio is defined as X_D/X_R, where X_D is the weight fraction of the gas phase in the downcomer and X_R is the weight fraction of the gas phase in the riser. The ratio is actually equivalent to the percentage of the gas phase which is carried under, since $X_D/X_R = W_{gD}/W_{gR}$. It is apparent from Figs. 16 and 17 that there is very little effect of interface height on the magnitude of carryunder beyond a height of ~6-8 in., which is reasonably close to H/D = 1. This fact is in good agreement with the studies of fluid-flow streamline (discussed previously in Section II) which showed similar characteristics. The larger voids in the downcomer than in the riser, as seen in Fig. 16, stem from the unique characteristics of 2-phase flow in downflow. As the downcomer velocity approaches the buoyancy velocity of the gas bubbles, the volume fraction

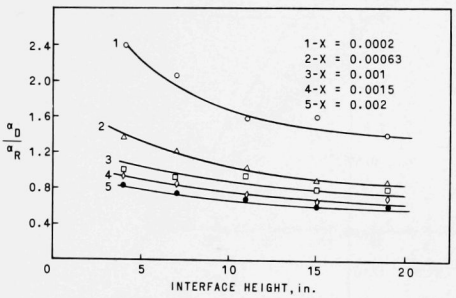

Fig. 16. Effect of Interface Height on the Volumetric Carryunder.

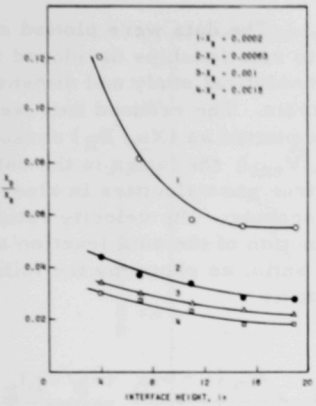

Fig. 17. Effect of Interface Height on the Weight Fraction Carryunder.

increases sharply, since the relative velocity of the 2 phases is approaching zero. Thus, for conditions in which downcomer flow velocities are very close to the buoyancy velocity of the gas bubble, the downcomer void fractions become very large and, in fact, much larger than riser void fractions.

A second series of runs were then made to study the effect of temperature, since it was observed that, unless the temperature of the water was held to within rather narrow limits, the data were not reproducible. Although the temperature of the system could not be varied over a wide range, a large effect was found over the temperature interval from 60 to 115°F, as shown in Fig. 18. The data shown in this figure are for constant mixture quality and flow rate. As can be seen, the quantity of the gas phase carried under decreases sharply as the temperature is increased. Since all the physical properties of the system remain virtually constant or varied very little, except for the viscosity, the change in carryunder is attributed to the change in viscosity.

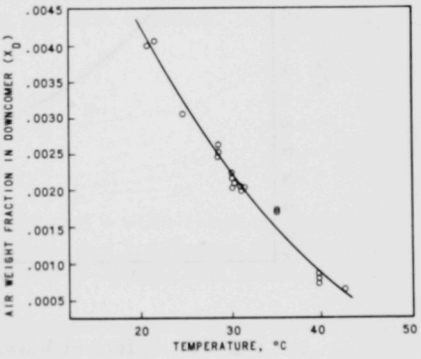

Fig. 18. Effect of Temperature on Carryunder.

A strong effect of the liquid-phase mass velocity on carryunder is shown in Fig. 19. In Fig. 19 the weight fraction ratio, which is equivalent to the % carryunder, is plotted as a function of the superficial liquid-phase downcomer velocity for a fixed gas-phase flow rate and interface height. As can be seen, the carryunder increased sharply once the velocity threshold was surpassed and continued to rise steadily, but at a lesser rate, as the downcomer velocity increased further.

An opposite effect was observed as the gas-phase mass velocity increased (see Fig. 20). For a constant liquid-phase mass velocity and interface height, the percent carryunder decreased as the gas-phase flow rate increased. The same behavior pattern was found for each of the liquid mass velocities studied.

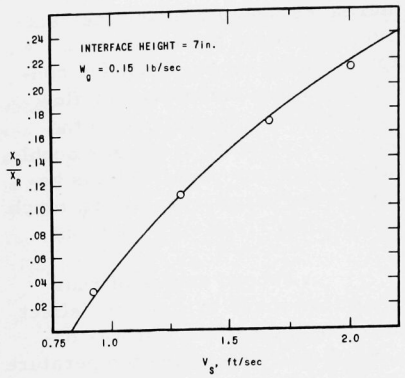

Fig. 19. Effect of Superficial Downcomer Velocity on Carryunder.

The data were plotted according to relationships developed from the analytical study and dimensional analysis. The reduced data were first plotted as (X_D/X_R) versus (V_g/V_{ent}); the latter is the ratio of the true gas velocities in riser and downcomer. The velocity ratio is a function of the void fraction and slip ratio, as shown by the following equation:

$$\frac{V_g}{V_{ent}} = \frac{A_D}{A_R}\frac{(1-\alpha)_D}{(1-\alpha)_R}\frac{(V_g/V_L)_R}{(V_g/V_L)_D} \qquad (61)$$

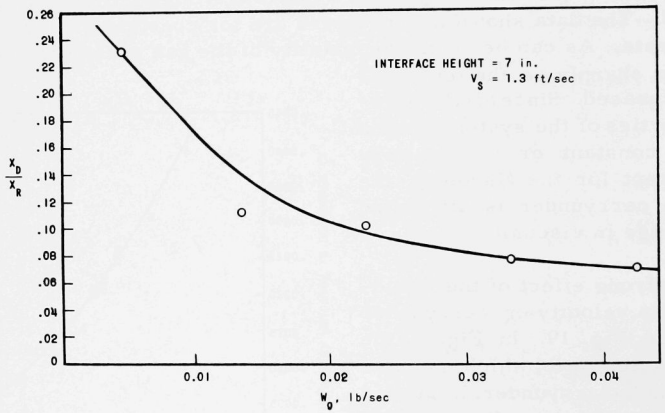

Fig. 20. Effect of Riser Quality on Carryunder.

As can be seen in Fig. 21, the percent carryunder is a function of the velocity ratio, but a family of curves is obtained for the different liquid mass velocities. The data plotted in the figure were taken at constant temperature and from a single geometrical arrangement. However, the interface height varied from 4 to 19 in. Similar curves were obtained for the different temperatures.

The data were then plotted as a function of the dimensionless groupings that were derived through dimensional analysis, namely,

$$V_g/V_{ent} \quad , \quad \sigma/\mu V \quad , \quad \text{and} \quad gD/V^2 \quad .$$

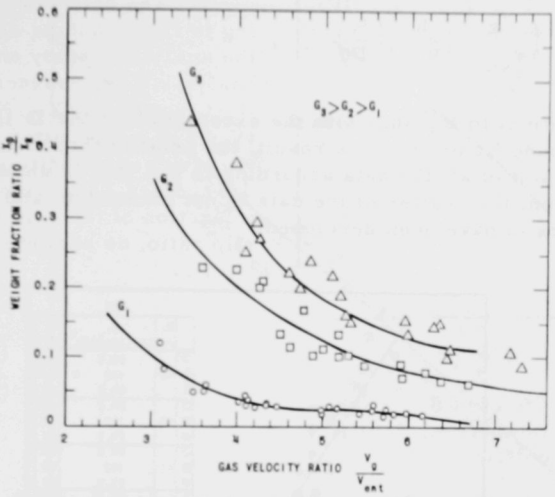

Fig. 21. The Weight Fraction Carryunder Ratio Versus V_g/V_{ent}.

Initial plots indicated that an exponent of $\frac{1}{2}$ was required on the reciprocal of the Froude Number to bring the data together. A plot of data according to the relationship

$$X_D/X_R = f\left[\left(\frac{\sigma}{\mu V}\right)\left(\frac{V_g}{V_{ent}}\right)\left(\frac{gD}{V^2}\right)^{1/2}\right] \qquad (62)$$

is given in Fig. 22. The data shown represent a wide range of mixture qualities, 3 different liquid mass velocities, and 2 different temperatures. As can be seen, the data are correlated fairly well by this relationship.

Another series of runs were then made to study the effect of system geometry. Due to limited volumetric air and water capacities the system could not be enlarged; as a result, a smaller geometrical arrangement was studied. Data were taken at a constant temperature and varying mixture qualities, interface heights, and mass velocities. The data were plotted according to the same relationship used to correlate the previous sets of data, Eq. (62), and a separation occurred; that is, the data points fell below the data points for the larger system. The separation was found to be due to the diameter factor in the Froude Number. It was determined that the 2 sets of data could be brought together essentially by the following relationship

$$\frac{X_D}{X_R} = \left(\frac{V_g}{V_{ent}}\right)\left(\frac{K}{V^2\mu}\right)\left(\frac{H}{D}\right)^{1/2} , \qquad (63)$$

which is identical to Eq. (62) with the exception that the D is removed from the Froude Number. As a result, the relationship is no longer dimensionless. A plot of all the data according to Eq. (63) is shown in Fig. 23. As can be seen, the scatter of the data is not excessive, and a basic correlation appears to have been developed.

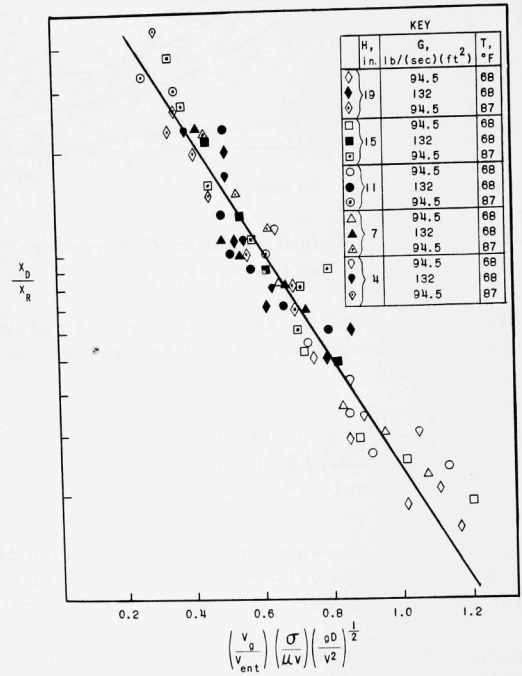

Fig. 22. Dimensionless Correlation of Air-Water Carryunder Data.

The air-water study has thus demonstrated the dependence of carryunder on a number of the system and fluid variables, and therein lies its value. The variables are: (1) system geometry factors, such as area ratio between downcomer and riser, diameter of the riser, and height of the 2-phase mixture interface above the riser; (2) water and air mass velocities and their relative velocities (the carryunder is especially sensitive to the liquid-phase mass velocity); (3) the temperature-dependent physical properties of the fluids, such as viscosity, density, and surface tension.

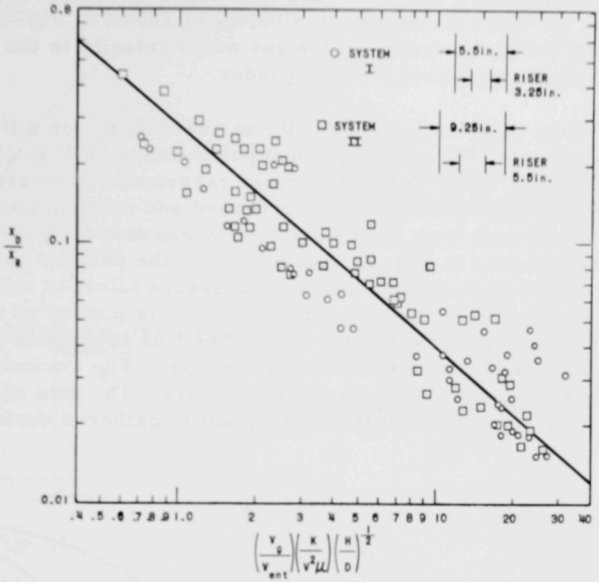

Fig. 23. Nondimensionless Correlation of Air-Water Carryunder Data.

The latter group represented the variables that were believed to be quite important and which required substantial additional study. As a result, it was decided to explore the effects of these parameters further on a high-pressure steam-water system in which they could be varied conveniently with pressure. The results of these studies are given in the following section.

High-pressure Steam-Water Study

Three series of data were taken at pressures of 600, 1000, and 1500 psi. The interface height and the vapor and liquid mass velocities were varied in a manner similar to that described in the air-water studies.

In general, similar trends were developed in the high-pressure data as were observed in the air-water data. The notable exception was the variation of the percentage carryunder with increasing gas-phase mass flow rate. The air-water data, shown previously in Fig. 20, indicated that the carryunder decreased as the gas-phase mass velocity increased. However, the high-pressure data showed a somewhat different trend (see Fig. 24). For a fixed pressure and liquid mass velocity, as the gas-phase flow rate was increased (by increasing power), the carryunder initially

decreased and reached a minimum and then began to increase. The trend was the same for the 2 pressures studied, as is shown in Fig. 24. It is possible that a further increase in the gas mass velocity in the air-water system would have increased the carryunder.

The effect of downcomer velocity on carryunder for a fixed power and for pressures of 600, 1000, and 1500 psi is shown in Fig. 25. Again as noted for the air-water data the percent carryunder increases sharply once the velocity threshold has been surpassed and continues to rise steadily but at a lesser rate as the velocity increases. The pressure effect can also be seen in Fig. 25. As expected, the percent carryunder was greater at the higher pressure. The pressure effect is shown more clearly in Fig. 26. Here, the percent carryunder is plotted as the system pressure for a constant downcomer velocity of 1.65 ft/sec and an approximately constant steam volume fraction at the exit. The amount of carryunder increases rapidly with increasing pressure. The data shown in the previous figures are typical of the large quantity gathered during the study.

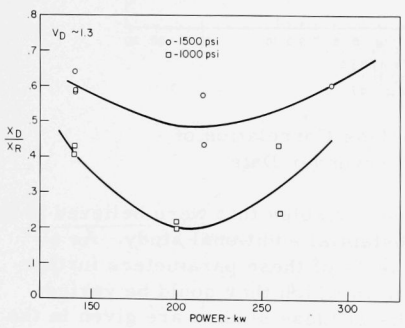

Fig. 24. Effect of Power on the Weight Fraction Carryunder Ratio

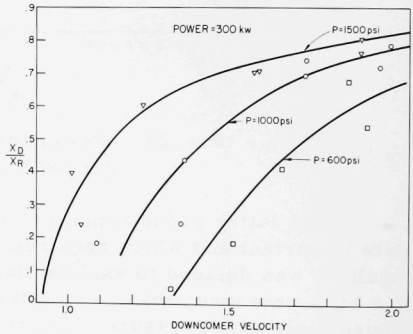

Fig. 25. Effect of Superficial Downcomer Velocity on the Weight Fraction Carryunder Ratio

Each set of the high-pressure data was adequately correlated by the dimensionless groupings given in Eq. (63), as shown in Figs. 27, 28, and 29. A family of curves was obtained that separate slightly with pressure and whose slopes, however, are essentially the same. The pressure separation was removed by adding the dimensionless ratio $(\rho_g/\rho_L)^{1/2}$, as shown in Fig. 30. All the high-pressure data for the one geometrical arrangement are correlated by the following dimensionless groupings:

$$\frac{X_D}{X_R} = f\left[\left(\frac{V_g}{V_{ent}}\right)\left(\frac{g_c\sigma}{\mu V}\right)\left(\frac{gD}{V^2}\right)^{1/2}\sqrt{\frac{\rho_g}{\rho_L}}\sqrt{\frac{H}{D}}\right] . \qquad (64)$$

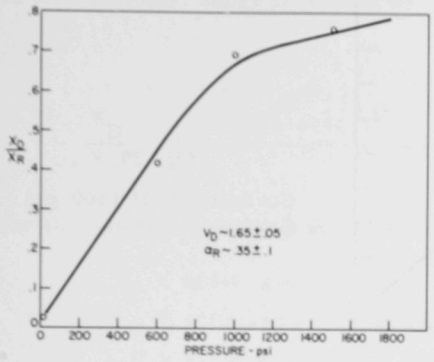

Fig. 26

Effect of Pressure on the Weight Fraction Carryunder Ratio

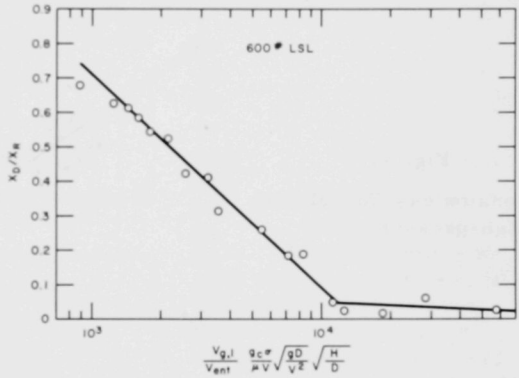

Fig. 27

Correlation of 600-psi Carryunder Data

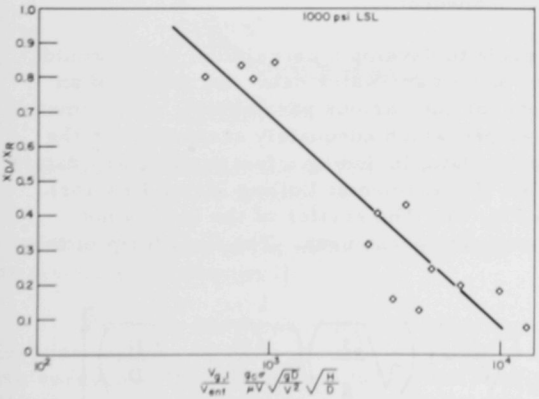

Fig. 28

Correlation of 1000-psi Carryunder Data

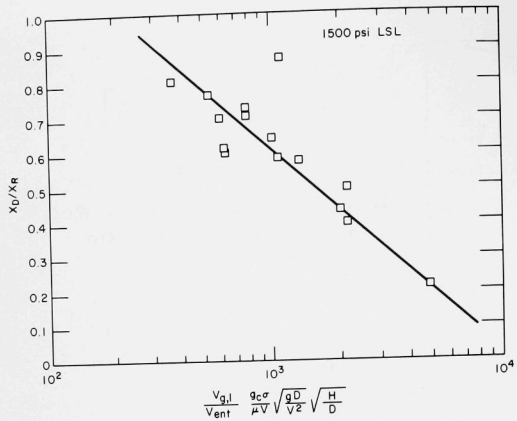

Fig. 29

Correlation of 1500-psi Carryunder Data

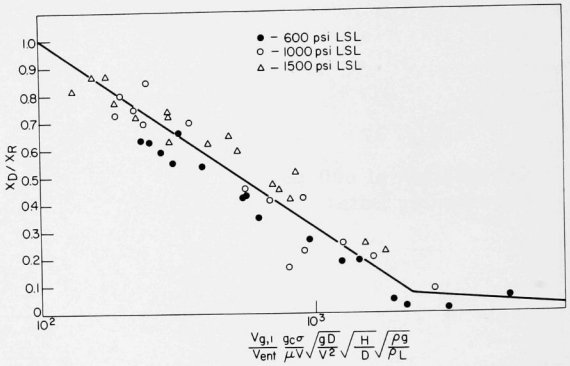

Fig. 30

Dimensionless Correlation of High-pressure Data

The atmospheric air-water data, however, deviated greatly from the correlation, which indicated a basic inadequacy.

An attempt was then made to develop a correlation which would encompass both the air-water and steam-water data. By means of an extensive series of cross plots for the various parameters, a nondimensionless correlation was developed which adequately accounted for the large majority of the carryunder data, including a few preliminary data points obtained from the EBWR (Experimental Boiling Water Reactor). This correlation is shown in Fig. 31. The scatter of the data is not exceptionally bad for such a complex phenomena. The final form of this equation is

$$\frac{X_D}{X_R} = -0.04 \frac{\ln\left[\left(\frac{V_g}{V_{ent}}\right)\left(\frac{\sigma^{2/3}}{G^2\mu}\right)\left(\sqrt{\frac{\rho_L}{\rho_g}}\right)\left(\sqrt{\frac{D}{H}} + \sqrt{\frac{H}{D}}\right)\right]}{64} \qquad (65)$$

in the functional range from 3 to 64 and

$$\frac{X_D}{X_R} = -0.6 \frac{\ln\left[\left(\frac{V_g}{V_{ent}}\right)\left(\frac{\sigma^{2/3}}{G^2\mu}\right)\left(\sqrt{\frac{\rho_L}{\rho_g}}\right)\left(\sqrt{\frac{D}{H}} + \sqrt{\frac{H}{D}}\right)\right]}{3.7} \qquad (65a)$$

for the functional range from 0.1 to 3, where

V_g = actual gas velocity

V_{ent} = actual gas velocity in downcomer

σ = surface tension of liquid, lb/ft

G = liquid mass velocity in riser, lb/(sec)(ft^2)

μ = liquid viscosity, lb/ft sec

ρ_L = density of liquid, lb/ft^3

ρ_g = density of gas, lb/ft^3

D = diameter of riser, ft

H = actual interface height, ft.

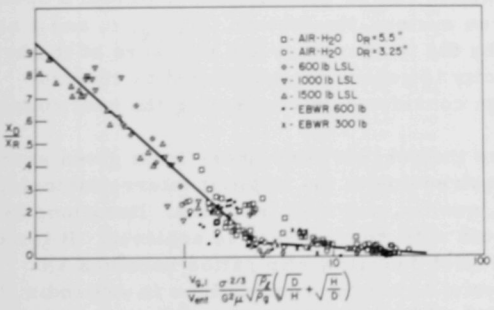

Fig. 31. Nondimensionless Correlation of all Carryunder Data

It is interesting to note that there are several groupings which are the same or very similar to those of the dimensionless correlation shown in Fig. 30. Also, it should be noted that a rather sharp break point exists, suggesting 2 distinct sets of carryunder conditions. It is postulated that the break point represents the threshold for carryunder, and that the data points to the right represent that fraction of the vapor flow which is located near the periphery of the riser and which is extremely difficult to separate, as discussed in Section II.

Probably the most important question concerning the correlation is the size factor. One can argue from intuition that in very large systems the carryunder should be less, since for conditions of equal flow in geometrically similar systems the mean turning radius (and hence escape time)

for the gas bubbles is larger. On the other hand, in the large-diameter systems the interface height of the operating mixture is generally held to much smaller levels and thus the average cross-flow velocities are higher. Therefore, one has competing size factors. The geometrical factors in this correlation are given by the term $\left(\sqrt{H/D} + \sqrt{D/H}\right)$ and indirectly through V_g/V_{ent}, which has an area ratio between the downcomer and riser built in [see Eq. (61)]. The factor $\left(\sqrt{H/D} + \sqrt{D/H}\right)$ was derived by comparing the preliminary large-system reactor data with the small-scale loop equipment. Additional data with larger systems are needed to completely establish the validity of the geometry factors in the correlation.

Based on this study, the following relationship can be used for minimizing carryunder:

$$\left(\frac{V_g}{V_{ent}}\right)\left(\frac{\sigma^{2/3}}{G^2\mu}\right)\sqrt{\frac{\rho_L}{\rho_g}}\left(\sqrt{\frac{H}{D}} + \sqrt{\frac{D}{H}}\right) \geq 3 \quad . \tag{66}$$

The function represents the break point beyond which the carryunder is normally 5% or under.

For carryunder analysis, Eq. 66 or Fig. 31 can be used in either of several ways. Either the geometrical characteristics of the system are specified and the expected carryunder can be computed, or the required geometrical dimensions of the system can be estimated to maintain a specified carryunder level. For a given system, the factors, ρ_L, ρ_g, σ, and μ are specified by the fluids used and by the temperature and pressure of the system. Also, the liquid mass velocity is generally established by thermodynamic and hydrodynamic design consideration concerning the heat source.

If it is desired to estimate the percent carryunder for a given system, a trial-and-error analysis is required due to the implicit interrelationship between the downcomer velocity, quality, and void fractions. Iterations between these factors are carried out until convergence is achieved. It is readily apparent that the ability to predict downflow slip ratios becomes an important factor in such an analysis, hence the correlations in Appendix D. The accuracy in the estimates of downflow slip ratio are reflected rather strongly in the carryunder analysis. If it is desired to specify the geometrical characteristics of a system in order to maintain a given carryunder level, the analysis is straightforward and an iterative procedure is not required.

The validity of the carryunder correlation presented cannot be completely specified, primarily because of the system size factor. Prudent usage of the correlation is therefore advisable until further data become available from larger systems. It is believed, however, that at a minimum a "ball park" answer can be obtained from the correlation. The agreement of the preliminary EBWR data with the correlation offers promise that it may, in fact, be fairly accurate. A complete tabulation of the data gathered in this investigation is given in Tables II and III.

Table II

DATA FOR AIR-WATER SYSTEM

Riser Diameter, in.	Wt, lb/sec	V_D, ft/sec	$X_D \times 10^{+3}$	$X_e \times 10^{+3}$	α_D	α_e	Riser Diameter, in.	Wt, lb/sec	V_D, ft/sec	$X_D \times 10^{+3}$	$X_e \times 10^{+3}$	α_D	α_e
5.5	15.53	0.924	0.0104	0.202	0.074	0.104	5.5	21.4	1.28	0.146	0.617	0.186	0.272
	15.53	0.924	0.0106	0.202	0.0732	0.119		21.6	1.29	0.103	1.04	0.247	0.218
	15.53	0.924	0.0111	0.202	0.0732	0.119		21.6	1.29	0.115	1.04	0.248	0.227
	15.53	0.924	0.0164	0.202	0.0773	0.161		21.6	1.29	0.134	1.04	0.255	0.259
	15.53	0.924	0.0164	0.202				21.6	1.28	0.152	1.04	0.257	0.262
	15.53	0.924	0.0242	0.202	0.0773	0.186		21.7	1.29	0.163	1.04	0.255	0.285
	15.422	0.917	0.0181	0.63	0.186	0.165		21.8	1.3	0.125	1.56	0.315	0.248
	15.422	0.917	0.0180	0.63	0.182	0.161		21.6	1.29	0.145	1.57	0.315	0.257
	15.422	0.917	0.0214	0.63	0.184	0.188		21.7	1.29	0.162	1.57	0.317	0.286
	15.422	0.917	0.023	0.63	0.186	0.228		21.8	1.3	0.179	1.56	0.317	0.306
	15.422	0.917	0.0273	0.63	0.186	0.251		21.8	1.3	0.147	1.98	0.351	0.273
	15.422	0.917	0.0218	1.015	0.249	0.178		21.8	1.3	0.164	1.98	0.352	0.284
	15.68	0.932	0.0293	1.003	0.23	0.190							
	15.53	0.924	0.0253	1.012	0.242	0.194							
	15.53	0.924	0.0267	1.012	0.251	0.244	3.25	5.7	0.933	0.6087	0.199	0.076	0.104
	15.53	0.924	0.0307	1.012	0.249	0.23		5.7	0.933	0.0093	0.199	0.065	0.108
	15.53	0.924	0.0342	1.012	0.257	0.253		5.7	0.945	0.0089	0.278	0.076	0.098
	15.53	0.924	0.0197	1.012	0.247	0.178		5.91	0.967	0.01	0.272	0.079	0.115
	15.42	0.917	0.024	1.532	0.32	0.199		5.84	0.955	0.0106	0.275	0.078	0.106
	15.42	0.917	0.0295	1.532	0.314	0.211		5.84	0.956	0.012	0.275	0.075	0.116
	15.42	0.917	0.0365	1.532	0.318	0.24		5.84	0.956	0.015	0.275	0.076	0.134
	15.42	0.917	0.0423	1.532	0.318	0.274		5.91	0.967	0.0178	0.577	0.187	0.151
	15.42	0.917	0.0482	1.532	0.316	0.30		5.91	0.967	0.0189	0.573	0.188	0.163
	15.42	0.917	0.0316	2.019	0.357	0.229		5.91	0.967	0.02	0.573	0.194	0.164
	15.42	0.917	0.0316	2.05	0.376	0.238		5.91	0.967	0.0213	0.573	0.194	0.176
	15.42	0.917	0.0397	2.05	0.36	0.265		5.91	0.967	0.0208	0.573	0.196	0.215
	15.42	0.917	0.0345	2.05	0.372	0.240		5.91	0.967	0.0236	0.961	0.27	0.182
	15.42	0.917	0.0457	2.05	0.372	0.282		5.91	0.967	0.0234	0.961	0.272	0.181
	15.42	0.917	0.0525	2.05	0.37	0.367		5.91	0.967	0.0316	0.961	0.272	0.188
	21.7	1.29	0.0423	0.215	0.0763	0.128		5.91	0.967	0.029	0.961	0.276	0.22
	21.8	1.3	0.0441	0.211	0.0763	0.141		5.91	0.967	0.0339	0.961	0.274	0.244
	21.8	1.3	0.0483	0.211	0.069	0.138		5.91	0.967	0.0254	1.44	0.342	0.195
	21.8	1.3	0.0489	0.211	0.075	0.163		5.88	0.963	0.0253	1.45	0.348	0.198
	21.8	1.3	0.0492	0.211	0.079	0.182		5.91	0.967	0.0258	1.44	0.349	0.205
	21.9	1.304	0.0692	0.614	0.188	0.174		5.77	0.945	0.0273	1.47	0.340	0.198
	21.9	1.304	0.0815	0.614	0.188	0.18		5.91	0.967	0.028	1.44	0.346	0.208
	21.9	1.304	0.0795	0.614	0.196	0.196		5.91	0.967	0.03	1.44	0.352	0.227
	21.8	1.3	0.0625	0.625	0.188	0.178		5.91	0.967	0.0372	1.44	0.352	0.248
	21.7	1.29	0.0691	0.627	0.193	0.197		5.91	0.967	0.0667	1.44	0.352	0.213
	21.7	1.29	0.1055	0.627	0.195	0.225		5.88	0.963	0.0288	1.87	0.395	0.213
	21.7	1.29	0.0737	1.032	0.26	0.189		5.88	0.963	0.0275	1.87	0.399	0.215
	21.7	1.29	0.0889	1.032	0.268	0.202		5.84	0.956	0.0298	1.88	0.397	0.229
	21.7	1.29	0.0885	1.032	0.271	0.216		5.91	0.967	0.0349	1.86	0.400	0.253
	21.7	1.29	0.1037	1.032	0.272	0.25		5.84	0.956	0.0596	1.88	0.400	0.220
	21.7	1.29	0.0894	1.54	0.322	0.173		7.96	1.304	0.0382	0.193	0.777	0.109
	21.7	1.29	0.0963	1.54	0.325	0.229		7.96	1.304	0.0401	0.199	0.0815	0.107
	21.7	1.29	0.111	1.54	0.330	0.258		7.96	1.304	0.0407	0.199	0.0836	0.111
	21.7	1.29	0.121	1.54	0.330	0.274		7.96	1.304	0.0443	0.199	0.0857	0.111
	21.7	1.29	0.125	1.54	0.330	0.280		7.96	1.304	0.0495	0.199	0.0899	0.128
	21.7	1.29	0.101	1.972	0.368	0.235		7.91	1.296	0.0612	0.595	0.203	0.159
	21.7	1.29	0.107	1.972	0.368	0.244		7.91	1.296	0.0625	0.595	0.207	0.16
	21.7	1.29	0.119	1.972	0.360	0.261		7.91	1.296	0.0640	0.595	0.209	0.184
	21.7	1.29	0.138	1.972	0.364	0.299		7.91	1.296	0.0916	0.595	0.209	0.217
	28.2	1.68	0.0509	0.2005	0.063	0.121		7.91	1.296	0.0749	1.003	0.284	0.144
	21.8	1.3	0.0424	0.211	0.0763	0.123		7.91	1.296	0.0754	1.003	0.29	0.198
	21.8	1.3	0.0534	0.209	0.0815	0.136		7.91	1.296	0.0787	1.003	0.29	0.196
	21.7	1.29	0.0559	0.211	0.0804	0.135		7.91	1.296	0.094	1.003	0.293	0.23
	21.6	1.28	0.0632	0.212	0.0825	0.149		7.91	1.296	0.0929	2.01	0.414	0.225
	21.8	1.3	0.0797	0.209	0.0825	0.179		7.91	1.296	0.0952	2.01	0.43	0.225
	21.7	1.29	0.0935	0.21	0.09	0.207		7.91	1.296	0.107	2.01	0.435	0.263
	21.9	1.3	0.0912	0.609	0.18	0.198		7.91	1.296	0.089	1.5	0.347	0.22
	21.9	1.3	0.0945	0.604	0.177	0.205		7.91	1.296	0.0879	1.5	0.35	0.217
	21.6	1.28	0.116	0.612	0.182	0.227		7.91	1.296	0.0935	1.5	0.353	0.229
	21.5	1.28	0.136	0.62	0.182	0.252		7.91	1.296	0.172	1.5	0.355	0.253

Table III

HIGH-PRESSURE DATA

Pressure, psi	Wt, lb/sec	Power, Kw	V_{SD}, ft/sec	X_D	X_e	α_D	α_e
600	7.39	250.8	1.48	0.0076	0.0286	0.497	0.361
	8.33	301.3	1.66	0.015	0.0363	0.62	0.412
	8.32	343.	1.65	0.0167	0.0396	0.678	0.429
	9.82	351.6	1.94	0.0266	0.0429	0.703	0.451
	9.6	351.4	1.89	0.0308	0.0494	0.764	0.484
	9.84	351.4	1.94	0.026	0.0446	0.697	0.473
	7.43	353.2	1.47	0.0024	0.0414	0.648	0.441
	7.34	353.2	1.43	0.0171	0.054	0.613	0.499
	7.46	401.7	1.44	0.0339	0.0648	0.768	0.541
	7.55	396.4	1.5	0.0071	0.0385	0.536	0.43
	7.58	299.	1.51	0.00637	0.034	0.536	0.401
	9.64	299.	1.92	0.0204	0.0377	0.65	0.434
	5.71	309.8	1.13	0.0008	0.0423	0.079	0.433
	5.7	309.8	1.13	0.0009	0.0423	0.089	0.435
	6.65	311.5	1.32	0.0018	0.0378	0.165	0.414
	6.14	199.9	1.24	0.0008	0.0234	0.102	0.384
	8.72	200.2	1.76	0.0134	0.0209	0.589	0.358
	6.14	299.3	1.22	0.00014	0.0377	0.109	
1000	4.58	150.5	0.987	0.00427	0.0265	0.0934	0.220
	6.29	150.5	1.35	0.0114	0.0281	0.378	0.228
	6.3	149.9	1.35	0.0122	0.028	0.377	0.225
	8.11	149.9	1.75	0.0172	0.0217	0.37	0.184
	6.2	225.4	1.33	0.00635	0.0316	0.362	0.286
	6.18	225.4	1.32	0.0074	0.0333	0.342	0.288
	4.95	224.6	1.05	0.00512	0.0371	0.132	0.336
	4.95	224.6	1.058	0.0031	0.0386	0.254	0.297
	8.36	224.6	1.78	0.03097	0.0394	0.63	0.356
	9.15	224.6	1.93	0.0239	0.0285	0.414	0.248
	9.25	224.6	1.99	0.0223	0.028	0.447	0.249
	4.96	302.1	1.04	0.010	0.0542	0.598	0.380
	6.18	300.1	1.3	0.0121	0.0487	0.431	0.355
	6.38	300.1	1.32	0.03	0.068	0.669	0.464
	8.0	300.1	1.68	0.0386	0.0522	0.622	0.424
	9.13	300.1	1.94	0.032	0.0406	0.528	0.334
	9.01	300.1	1.91	0.0325	0.0454	0.552	0.356
1500	4.44	224.9	1.01	0.01095	0.0513	0.270	0.283
	4.49	224.9	1.0	0.036	0.0724	0.49	0.336
	5.41	224.7	1.22	0.0362	0.0627	0.506	0.327
	5.6	224.9	1.27	0.023	0.0528	0.356	0.285
	7.12	224.9	1.63	0.0322	0.044	0.481	0.344
	7.11	224.9	1.62	0.0371	0.0498	0.399	0.259
	8.39	224.1	1.94	0.0341	0.0392	0.33	0.217
	8.36	224.9	1.94	0.0325	0.0376	0.344	0.21
	4.64	171.8	1.06	0.021	0.0457	0.329	0.253
	5.6	150.1	1.3	0.0191	0.0326	0.284	0.214
	5.59	150.1	1.3	0.0208	0.0324	0.378	0.208
	7.03	185.	1.61	0.0268	0.043	0.368	0.274
	7.04	300.4	1.59	0.04	0.0564	0.436	0.336
	6.98	300.4	1.57	0.0443	0.0629	0.485	0.36
	8.44	300.4	1.90	0.0432	0.0534	0.468	0.348
	8.4	300.4	1.9	0.0424	0.0554	0.444	0.337
	5.49	300.4	1.23	0.0408	0.0675	0.513	0.396
	4.54	300.4	1.01	0.027	0.0679	0.449	0.403
	4.6	300.4	1.04	0.0143	0.0597	0.345	0.374

ACKNOWLEDGEMENTS

This report is the result of an intensive 2-year study. During its course, a number of people became involved with the research program. Their suggestions, discussions, and contributions aided greatly in bringing the research to a successful conclusion.

Particular recognition need be given to the following people:

Mr. Peter Zaleski carried the brunt of the tedious work load which is inherent in a study of this type. He was responsible for the major portion of the data reduction, tabulation, plotting, and correlation. Mr. Zaleski also developed a large portion of the bubble-size distribution correlation virtually on his own and aided in the final compilation of the report.

Professor Nejat Abyers performed a preliminary analysis of the carryunder problem, which he compared with the early air-water studies. His analysis served as the basis on which the final carryunder model presented was built. He also made a study of the behavior of single bubbles rising in a fluid. Appendix A essentially comprises a report he wrote on the problem.

E. A. Spleha designed and built the air-water apparatus with which the initial studies were carried out. He supervised a portion of the data taking with the loop and reduced a portion of the air-water data.

Professor Bates Chao devised the analytical procedures used in correlation of the bubble sizes and distributions which are given in Appendix B.

Mr. George Lambert helped reduce the phase-distribution data to a form which was used in developing the phase-distribution correlations. It was necessary for him to handle, sort, and compare extremely large quantities of data in order to perform this task.

Fred Nentwich became associated with the study in its final phase, but he made very significant contributions to the final results. He made the final comparison between the theoretical analysis and the air-water data. This involved numerous, complex, and tedious computations. He also assisted in the final editing of the report.

Thanks are also due to M. Gats, J. Chase, D. Giarrante, W. Jeans, A. Stodsdill, and W. Brewer, who operated the loops and took the data.

Appendix A

TRANSPORT OF GAS BUBBLES THROUGH A STAGNANT FLUID

Consider the case of a free-falling body. The forces acting on this body are: (1) an acceleration force due to gravity, whose magnitude is represented by F_G, (2) a buoyancy force of magnitude F_b, resulting from the displacement of the fluid through which the solid is falling, and (3) a retarding force of magnitude, F_R, which is caused by the frictional resistance due to the relative motion of the solid and the fluid.

If it is assumed that: (1) the particle is a spherical solid, (2) the fluid is incompressible and of sufficient extent to eliminate wall effects, and (3) there are no other particles affecting the motion of the particle under consideration, the resultant force tending to move the particle of mass M downward is

$$M \frac{dv}{dt} = (M - M_L)\, g - F_R \quad , \tag{A-1}$$

where $(M - M_L)$ is the apparent mass of the particle.

For the case of the rising bubble, the above assumptions lead to

$$M_g \frac{dv}{dt} = (M_L - M_g)\, g - F_R \quad . \tag{A-2}$$

If it can be assumed also that the motion of the bubble will be turbulent in nature, then the expression for the magnitude of the resisting force F_R is given by Newton's Law[6]

$$F_R = f_D\, A\, \rho_L\, V^2/2 \quad , \tag{A-3}$$

where A is the projected area.

If this value of F_R is substituted in Eq. (A-2) for a spherical shape, there is obtained

$$\left(\frac{\pi D_0^3}{6}\right) \rho_g \frac{dv}{dt} = \left(\frac{\pi D_0^3}{6}\right) \left(\rho_L - \rho_g\right) g - f_D \pi \frac{D_0^2\, \rho_L\, V^2}{8} \tag{A-4}$$

and

$$\frac{dv}{dt} = \frac{(\rho_L - \rho_g)}{\rho_g}\, g - \frac{3 f_D\, \rho_L\, V^2}{4\, D_0\, \rho_g} \quad . \tag{A-5}$$

The frictional resistance increases with increasing velocity until the accelerating and resisting forces are equal. Then the bubble continues to move at a constant maximum speed V_0 generally referred to as the terminal velocity. At the terminal velocity V_0, $dv/dt = 0$; hence

$$\left(\frac{\rho_L - \rho_g}{\rho_g}\right) g = \frac{3 f_D \rho_L V_0^2}{4 D_0 \rho_g}$$

and

$$V_0 = \sqrt{4 (\rho_L - \rho_g) g D_0 / 3 \rho_L f_D} \quad . \tag{A-6}$$

For very small bubbles it is probable that the motion of the bubbles would be in the laminar region. For this case, Stokes[7] showed that the resistance to the motion of a spherical particle is

$$F_R = 3\pi D \mu V \quad . \tag{A-7}$$

If Eq. (A.7) is used instead of Eq. (A-3) in the above analysis, the following equation is obtained for the terminal velocity in viscous or laminar flow:

$$V_0 = (\rho_L - \rho_g) g D_0^2 / 18 \mu \quad . \tag{A-8}$$

Consider the case of turbulent motion and Eq. (A-5). Let

$$a = g(\rho_L - \rho_g)/\rho_g; \quad b^2 = 4 D_0 g (\rho_L - \rho_g)/3 f_D \rho_L \quad .$$

The differential equation for the bubble motion is then

$$\frac{dv}{dt} = a\left(1 - \frac{V^2}{b^2}\right) \quad . \tag{A-9}$$

Integration of Eq. (A-9) gives the time elapsed until the bubble reaches the final speed V_0:

$$t = \frac{b}{2a} \ln \frac{b + V_0}{b - V_0} \quad . \tag{A-10}$$

Since

$$\frac{dV}{dt} = \frac{dL}{dt}\frac{dV}{dL} = V \frac{dV}{dL} \quad , \tag{A-11}$$

Eq. (A-9) becomes

$$V\frac{dV}{dL} = a\left(1 - \frac{V^2}{b^2}\right) \quad . \tag{A-12}$$

Integration of Eq. (A-12) gives the length of the path traveled by the bubble relative to the surrounding liquid:

$$L = \frac{b^2}{2a} \ln \frac{b^2}{b^2 - V^2} \quad . \tag{A-13}$$

If V_L denotes the speed of the liquid, then the absolute path length traveled by a bubble until it reaches the speed V_0 is

$$L_0 = \frac{b^2}{2a} \ln\left(\frac{b^2}{b^2 - V_0^2}\right) + V_L t \quad . \tag{A-14}$$

Rearrangement of Eq. (A-13) gives the speed as function of the length of the path traveled:

$$V = b\sqrt{1 - \exp\left(-2a\, L/b^2\right)} \quad . \tag{A-15}$$

Eq. (A-15) states also that the bubble speed tends towards a final constant value within a relatively small value of L if a is large and b is in the usual region. Thus

$$V_0 = b = \sqrt{4\left(\rho_L - \rho_g\right) g D_0 / 3\rho_L f_D} \quad . \tag{A-16}$$

It is known that the final speed of the bubble in a given system depends not only on the bubble diameter, but also upon the shape and on the type of motion of the bubble.

Relation between Bubble Size and the Terminal Velocity of Bubble

Since the motion of gas bubbles is an important factor in many mass and heat transfer operations, the problem has been studied intensively by numerous investigators.

From the measurement of terminal velocities of small bubbles, Allen[8] has concluded that the terminal velocity acquired by a small bubble ascending through a viscous fluid is the same as that which would be acquired by a solid sphere, and that when the motion is very slow the measured velocity of the bubble agrees with the value given by Stokes' equation:[7]

$$V_0 = \frac{g D_0^2}{18}\left(\frac{\rho_L - \rho_g}{\mu_L}\right)\left(\frac{\beta D_0 + 6\mu_L}{\beta D_0 + 2\mu_L}\right) \quad . \tag{A-17}$$

If it be assumed that the coefficient of sliding friction, β, is infinite, Eq. (A-17) reduces to Eq. (A-8), which shows that the terminal velocity varies as the square of the diameter of the sphere in the laminar region.

For $Re > 2$, the departure from Stokes' law was found to be significant, and for $2 < Re < 200$, Allen[8] deduced the formula

$$V_0 = \frac{1}{2}\left(\frac{\rho_L - \rho_g}{\rho_L}\right)^{2/3} \left\{ \frac{D_0}{2\sqrt{\mu_L}} - \frac{2}{5}\left[\frac{g\mu_L \rho_L}{2g(\rho_L - \rho_g)}\right]^{1/3} \right\} , \quad (A\text{-}18)$$

which states that the terminal velocity varies directly as the diameter of the bubble in a transition region between the laminar and turbulent regions. For $Re > 500$, for which Allen's equation does not apply, the general practice has been to use drag coefficients based on experimental data. The drag coefficient is usually defined by Newton's Law, Eq. (A-3), and is correlated as a function of the Reynolds number Re:

$$Re = D_0 V_0 \rho_L / \mu_L \quad . \quad (A\text{-}19)$$

Setting the friction factor f_D equal to 0.858 in Eq. (A-6) gives

$$V_0 = 0.405\sqrt{\frac{\rho_L - \rho_g}{\rho_L}}\, D_0 \ (D_0 \text{ in mm and } V_0 \text{ in ft per sec}), \quad (A\text{-}20)$$

which agrees with Rittinger's formula for turbulent motion of bubbles as reported by Martin.[9]

Pavlushenko[10] made an attempt to generalize the above relationships for the free motion of an individual particle in a stationary unlimited medium. Depending upon the fluid regime, as characterized by either Archimedes' criterion or by Reynolds number, he proposed that

(1) in the laminar regime Stokes' formula (A-8) be used;

(2) in the transition regions Allen's simplified formula be employed, and

(3) in the turbulent regime the following form of Rittinger's formula be used:

$$V_0 = 0.57\,(\rho_L - \rho_g)\, D_0 / \rho_L \quad .$$

Here D_0 is again in millimeters and V_0 is in feet per second. The limits reported by Pavlushenko in Archimedes numbers correspond to a Reynolds number of $Re_1 = 1.6$ for the boundary between the laminar and transition region and of $Re = 420$ for the boundary between the transition and turbulent regions.

Miyagi[1] studied the rate of rise of single air bubbles in water over a size range of $0.5 < D_0 < 8$mm. His data on the terminal velocity as a function of bubble size indicated a maximum speed of about 0.91 ft/sec at a limit of 0.75 ft/sec (see Fig. A-1). For bubbles of larger size the terminal velocity seemed to be independent of size. Bryn[11] and Luchsinger[12] report data which are in fair agreement with Miyagi's[1] results for bubble diameters exceeding 2 mm.

However, there is some evidence that the wall effect or the ratio D_0/D_1, where D is pipe diameter, has a marked effect on the terminal velocity. Several experimenters have established the existence of a region of bubble behavior in which the bubble velocity is independent of size. This may be due to an appreciable wall effect in most of the experiments involving large gas bubbles moving in 1- or 2-in. ID tubes.

O'Brien and Gosline[13] carried out experiments in tubes of diameters from 1.18 to 6 in. and showed that the wall effect in the case of narrow tubes tended to exert a retarding effect on the rise of bubbles. Thus, in a tube of diameter of 6 in., they did not obtain a maximum terminal velocity (see Fig. A-1). It is interesting to note that in no case do the authors obtain a clearly defined velocity maximum, and no explanation can be found for the inconsistency in these observations.

Rosenberg[14] performed extensive experiments on the velocity and shape of air bubbles in water. His results when plotted as the drag coefficient versus the Reynolds number deviated from the data for solid spheres and were similar to the results obtained by O'Brien and Gosline[13] and by Van Krevelin and Hoftijzer.[15] The drag coefficient of gas bubbles seems to be higher than that of solid spheres above some critical value. Measurements on the bubble shapes indicated that 4 general categories exist which are a function of the Reynolds number:

(1) spherical bubbles, $Re < 400$;

(2) oblate spheroids of varying geometric proportions, $400 < Re < 1100$;

(3) oblate spheroids of constant geometric proportions, $1100 < Re < 5000$;

(4) mushroom shape with spherical caps, $Re < 5000$.

For very large bubbles, in the range $5000 < Re < 40{,}000$, the data of Rosenberg[14] agreed with the results of Davies and Taylor.[16] Their data can be represented by the following equation:

$$V_0 = 5.45\sqrt{D_s} \quad , \qquad \text{(A-22)}$$

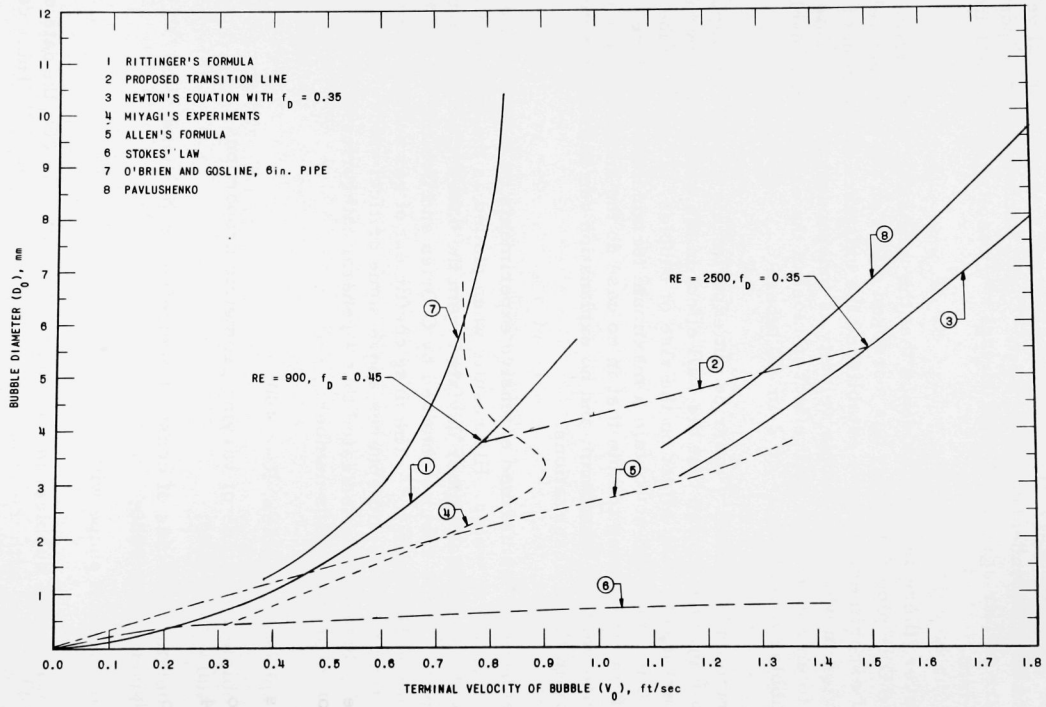

Fig. A-1. Bubble Size Versus Bubble Velocity

where

D_s = diameter of curvature of the spherical cap on a mushroomlike gas bubble, mm

V_0 = velocity, ft/sec.

The equivalent spherical diameter based on the gas bubble volume is given by

$$D_0 = 2.3\, D_s \quad . \tag{A-23}$$

Hence,

$$V_0 = 0.237 \sqrt{D_0} \quad . \tag{A-24}$$

It can be seen that for small bubbles, in the region $Re < 400$, the discrepancies are not large. But for medium-sized bubbles, in the range $400 < Re < 5000$, the wide discrepancy in the measured velocity of the gas bubbles remains to be explained. It appears that there may have been an error in the measurement of velocities arising from the fact that medium-sized bubbles with $1.5 < D_0 < 8$mm do not rise vertically in the liquid column, but take a zig-zag or spiral path. The instantaneous velocities are, therefore, usually greater than the average velocity which is recorded.

As the above far-from-complete list shows, a considerable amount of data exists on the motion of bubbles. However, it is by no means complete or even concordant. Because of the inconsistency of the data and the resulting inability to establish the bubble diameter-velocity relationship, it was assumed that the gas bubbles behave as solid spheres in the region of interest ($400 < Re < 2500$). Also, since the radius at which a gas bubble in water ceases to behave as a solid particle is not known accurately and may well vary from system to system, it was further assumed that the solid-sphere drag-coefficient data can be extended to the medium-sized bubble region without introducing great errors. Since the turbulent region is of primary interest, Rittinger's formula [Eq. (A-20)] was used to predict the terminal velocity of the gas bubbles. However, the same form of the equation does not apply over entire turbulent regions, since Rittinger's formula was derived by using a constant value of 0.858 for the drag coefficient f_d.

This can be seen by studying a plot of the drag coefficient as a function of the Reynolds number in Fig. A-2. The friction factor or the drag coefficient, f_D, in laminar flow is represented by a straight line with logarithmic coordinates. This condition exists up to a Reynolds number of about 3, at which value the drag coefficient begins to decrease as the value of Re becomes greater. However, the rate of decrease with increasing Reynolds number becomes less and less until a minimum of 0.35 is

reached at a Reynolds number of about 4000. In the interval $500 < Re < 2500$, the value of the friction factor becomes nearly constant and independent of Reynolds number, as indicated by the horizontal part of the line. The reason Rittinger's formula Eq. (A-20) has been used with some success in steam boilers is due to the fact that generally the conditions are such that the bubble diameters are in the limits of 1 to 4 mm and, as can be seen in Fig. A-2, $f_d = 0.858$ is an average value in this region.

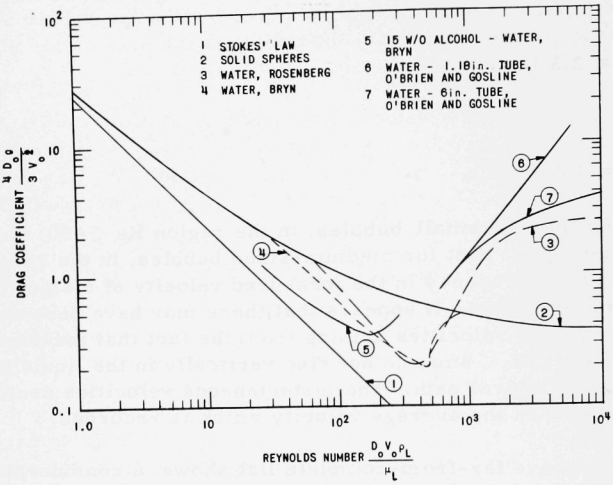

Fig. A-2. Drag Coefficient as a Function of the Reynolds Number

Data reported by several investigators have tended to support the use of Rittinger's formula in the vicinity of $D_0 = 4$ mm. Miyagi[1] reported a terminal velocity of 0.87 ft/sec for $D_0 = 4.1$ mm. Jakob[17] reported 0.85 ft/sec as the average velocity of 6 bubbles having diameters between 1 and 8 mm. Peebles and Garber[18] have also reported a velocity of 0.85 ft/sec for $D_0 = 3.75$ mm. Even though a convincing accumulation of data exists about the point $D_0 = 4$ mm, it does not appear feasible to continue using this equation much beyond this point, since for $D_0 = 4$ mm, $Re = 1000$ and $f_d = 0.43$, instead of the proposed value of 0.858.

In view of the wide variance in the data, a new bubble diameter versus terminal velocity relationship is proposed. The relationship evolved after a scrutiny of the data available as well as visual observation of the system, which showed the existence of relatively large semispherical bubbles. A comparison between the different formulae and the proposed relationship is given in Fig. A-1. Hopefully, excessive error is eliminated by this relationship in the range $1 \text{ mm} < D_0 < 10$ mm, the region of interest in this investigation.

Appendix B

BUBBLE SIZE AND DISTRIBUTION

At the outset of the carryunder investigation it became apparent that the nature of the existence of the gaseous phase in the liquid phase would have to be established. The results of a limited study of this problem are given in Appendices B and C. Data on the bubble size and distribution are presented in this Appendix and the data on the phase distributions are presented in Appendix C.

The investigation of bubble size and distribution was carried out in an atmospheric air-water loop, a schematic of which is shown in Fig. 6. A detailed description of the loop is given in Section IV. The downcomer and a portion of the upcomer were made of Lucite so that photographs of the bubbles could be obtained.

The photographs of the 2-phase mixture were taken with a Polaroid Camera with a Specification Equipment Comet Repeating Flash light source with a flash duration of ~1/1500 sec. The flash was used as the motion-stopping device rather than the shutter, whose speed was ~1/200 sec. The lighting techniques employed varied with the flow rate and void volume fraction. As an example, for a 2-phase mixture with a high void content, the lighting was done from the front, whereas for low void content side lighting was employed. The depth of focus of the camera was ~1 in.; the radius in the riser was ~2.5 in.; and the thickness of the downcomer was 2 in. Although the photos were essentially peripheral in nature, it is believed that they are representative of the true bubble size in the mixture, since large transverse macroscopic movements of the bubbles were observed.

The bubble sizes were developed by measuring and counting those bubbles in focus on the photograph. At least 2 photos per run were obtained and analyzed. As a check on the data-reduction technique, sample photographs were periodically analyzed by 4 individuals. The agreement on the average bubble size and on the distribution curves obtained was good. The maximum disparity between the average bubble size was ~25% with the majority of the comparisons being within 10%. The most significant errors were in the small-bubble range of 1 mm and less.

A series of runs were taken for varying flow rates and mixture qualities to study the effect on the bubble size and distribution. The parameter range studied was: void fraction from 0.1 to 0.4; liquid velocity upflow from 2 to 5 ft/sec; and liquid velocity downflow from 1 to 2.5 ft/sec. Photographs were taken for each condition, and the distribution of bubble sizes and mean bubble size were derived from the photo. The shape of the bubbles ranged from spheroids to spherical caps. The maximum dimension was taken

as the bubble diameter. A minimum of 400 bubbles per photo were counted to determine the distribution of bubble size.

The photos showed that the gaseous phase was dispersed throughout the liquid phase in the form of discrete bubbles, even in the higher void range studied. To the human eye in many instances the mixture appeared to be in segregated flow.

A series of photographs are given in Figs. B-1 to B-4. These are typical and show the nature of the phase dispersion as a function of the void volume fraction and true liquid velocity.

The average bubble size was determined by the following relationship.

$$\bar{D}_B = \frac{\sum n_i D_{Bi}}{\sum n_i} , \qquad \text{(B-1)}$$

where

D_{Bi} = diameter of a gas bubble

n_i = number of gas bubbles of diameter D_{Bi}.

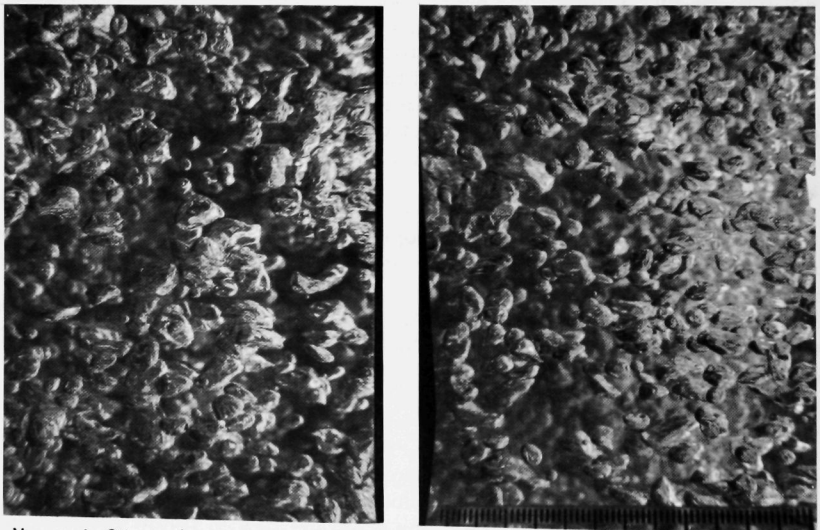

Fig. B-1. Typical Bubble Photograph

V_T = 1.27 ft/sec α_D = .19

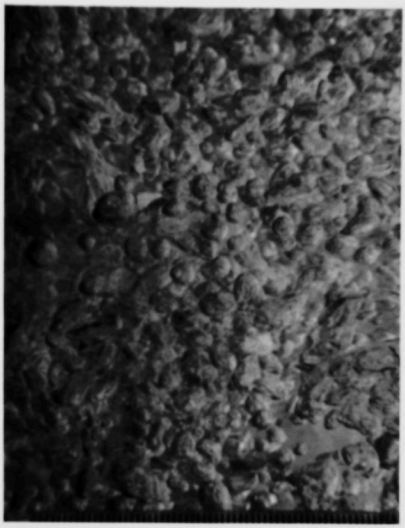

V_T = 1.70 ft/sec α_D = .23

Fig. B-2. Typical Bubble Photograph

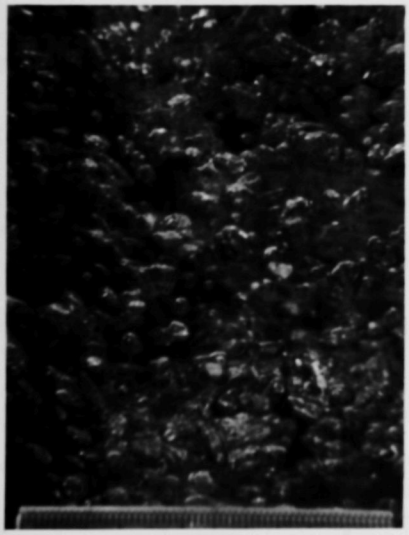

V_T = 1.6 ft/sec α_R = .0637

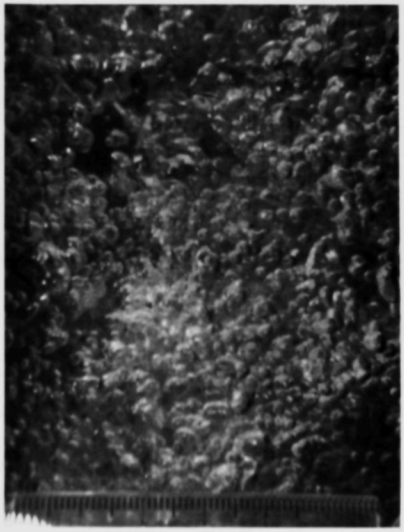

V_T = 3.34 ft/sec α_R = .1750

Fig. B-3. Typical Bubble Photograph

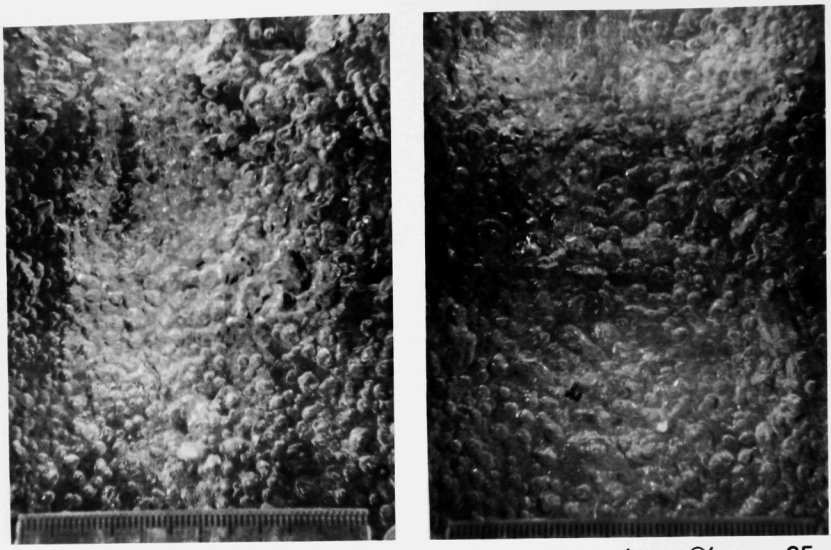

Fig. B-4. Typical Bubble Photograph

The average bubble diameter is a function of the mixture quality (see Figs. B-5 and B-6). As can be seen, a series of curves was obtained for different velocities. The average bubble size was then plotted versus the true liquid velocity, which is defined as

$$V_T = V_s/(1-\alpha) \quad . \tag{B-2}$$

When plotted in this manner, the correlation was rather good, and a single-valued relationship was obtained (see Fig. B-7). The fit of the data is represented by the following equation:

$$D_B = 5.2/V_T^{0.666} \text{ for } 0.5 < V_T < 5 \quad , \tag{B-3}$$

which represented the range of the data. As can be seen, the data from the riser and downcomer both fall along the same curve.

In a 2-phase mixture in which the dispersion of the gaseous phase in the liquid phase occurs through turbulence, the breakup and coalescence of the dispersed phase occurs continuously. The breakup may be caused by either viscose shear forces or by turbulent pressure fluctuations. If it is assumed that the process is random in nature, the bubble-size distribution

may be described by Poisson's distribution, which states that the probability of finding n points lying within any subinterval ζ is

$$P_{(n,\zeta)} = \frac{(k\zeta)^n}{n!} e^{-k\zeta} \quad , \tag{B-4}$$

where $k\zeta$ is the expected number of points within the subinterval.

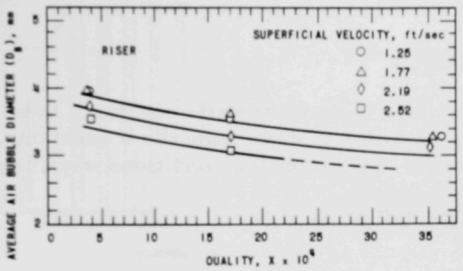

Fig. B-5. Bubble Diameter Versus Quality in Riser

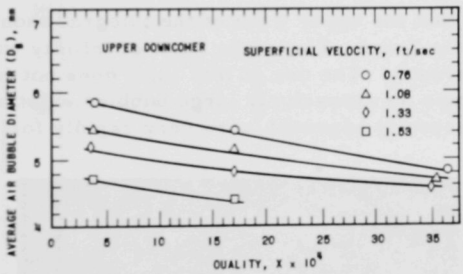

Fig. B-6. Bubble Diameter Versus Quality in Downcomer

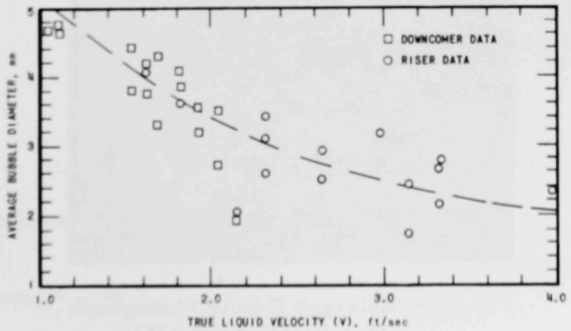

Fig. B-7. Bubble Diameter Versus True Liquid Velocity

To describe the bubble-size distribution, it is convenient to define a normalized distribution function $N_n(\chi)$ such that $N_n(\chi)\, d\chi$ gives the fraction of bubbles of the air-water mixture lying between χ and $\chi + d\chi$.

One of the many photographs taken of 2-phase mixture is shown on Fig. B-8. A plot of the distribution of bubble sizes as determined from this photograph is given in Fig. B-9. The radius interval of $\Delta\chi = 0.069$ in. was selected and the normalized distribution plot was constructed as shown in Fig. B-10. Poisson's law may now be written as

$$N_n(\chi) = P(b\chi)^c\, e^{-b\chi} \quad , \tag{B-5}$$

where P, b, and c are the 3 characteristic constants to be determined from the measured data. In order to determine the 3 constants, it is necessary to specify 3 conditions. The following conditions were imposed:

(a) From the definition of $N_n(\chi)$ it follows that

$$\int_0^\infty N_n(\chi)\, d\chi = 1 \quad . \tag{B-6}$$

It should be noted that the upper limit of the integral should be χ_{max} - the largest bubble radius found. The upper limit of infinity was used to simplify the computations greatly. The use of this limit does not introduce any appreciable error since no excessively large bubbles exist and the distribution function must necessarily approach zero very rapidly for $\chi > \chi_{max}$.

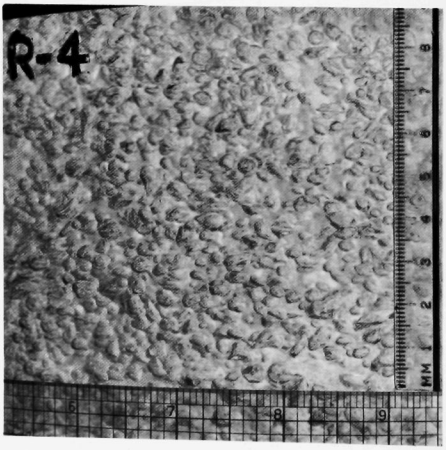

Fig. B-8. Enlarged Bubble Photograph
(Magnification - 2.175)

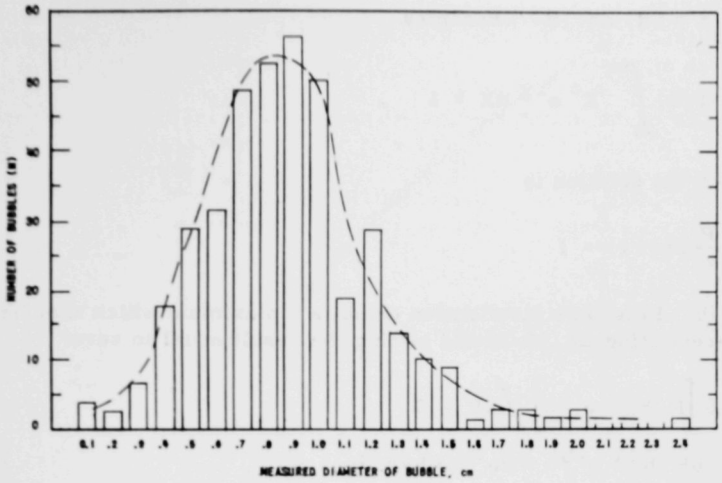

Fig. B-9. Distribution of Bubble Sizes Obtained from Fig. B-8

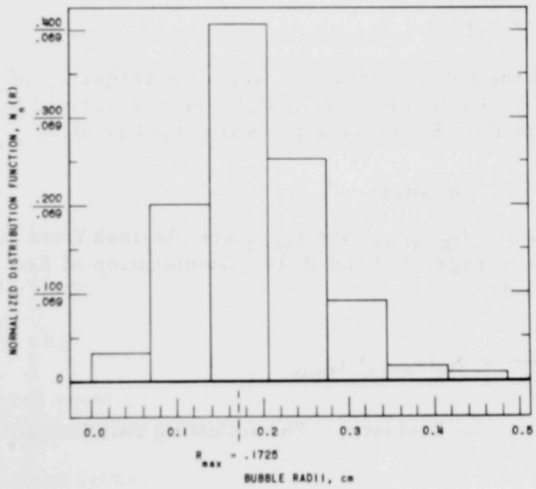

Fig. B-10. Normalized Bubble-size Distribution

Substitution of Eq. (B-5) into Eq. (B-6) yields

$$\int_0^\infty P(b\chi)^c \, e^{-b\chi} \, d\chi = 1 \quad . \tag{B-7}$$

Letting X = bR, Eq. (B-7) becomes

$$(P/b)\int_0^{\infty} X^c e^{-X} dX = 1 \quad , \tag{B-8}$$

for which the solution is

$$\frac{P}{b}\Gamma(c+1) = 1 \quad . \tag{B-9}$$

(b) Poisson's distribution exhibits a maximum which may be located by differentiating Eq. (B-5) and setting the result equal to zero:

$$d\left[P(b\chi)^c e^{-b\chi}\right] \Big/ dR = 0 \tag{B-10}$$

$$-bP(b\chi)^c e^{-b\chi} + Pe^{-b\chi}c(b\chi)^{c-1}b = 0 \quad , \tag{B-11}$$

which yields

$$\chi_{max} = c/b \quad . \tag{B-12}$$

Here χ_{max} is the bubble radius for which the frequency of occurrence is a maximum. The maximum value of $N_n(\chi)$ is then derived by substituting Eq. (B-12) into Eq. (B-5). This gives the third relation:

$$Pc^c e^{-c} = N_n(\chi_{max}) \quad . \tag{B-13}$$

The factor $N_n(\chi_{max})$ and χ_{max} are obtained from the plot of the data as shown in Figs. B-9 and B-10. Combination of Eqs. (B-9), (B-12), and (B-13) yields

$$\frac{c^{c+1} e^{-c}}{\Gamma(c+1)} = N_n(\chi_{max})\,\chi_{max} \quad , \tag{B-14}$$

from which c can be evaluated. The following relationships are used for evaluating P and b:

$$P = b/\Gamma(c+1) \tag{B-15}$$

$$b = c/\chi_{max} \quad .$$

Since Eq. (B-14) is a transcendental equation in c, the graph shown in Fig. B-11 has been prepared to facilitate computations.

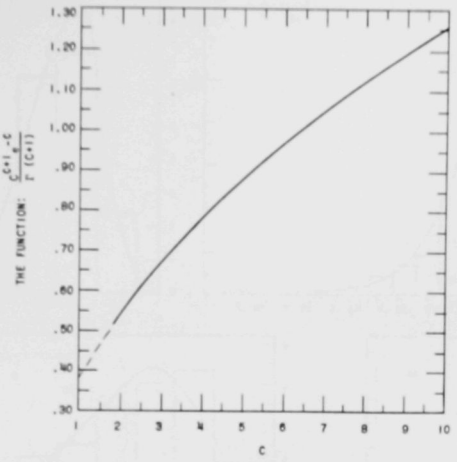

Fig. B-11. C Versus $\frac{c^{c+1}e^{-c}}{\Gamma(c+1)}$

Each of the distributions obtained from this series of test runs (described previously) was fitted to a Poisson's distribution, and the constants P, b, and c were evaluated. The constants were then correlated as a function of system parameters such as mass velocity and void fraction. Through a series of plots and cross plots the constants were determined to be

$$c = 17.7 \times 10^3 V_T^{1.5}/G^2 \qquad \text{(B-17)}$$

$$b = 15.34/(1-\alpha)^3 \qquad \text{(B-18)}$$

$$P = b/\Gamma(c+1) \quad . \qquad \text{(B-19)}$$

The general equation for predicting the bubble size distribution is therefore obtained by inserting the above values into Eq. (B-5).

A comparison between Eq. (B-5) and the actual distribution obtained from the photographic studies is shown in Figs. B-12 through B-16. The fit of the data is in general fairly good. As can be seen in the figures and as indicated by Eq. (B-5), the most probable bubble size decreases as the mass velocity and void volume fraction increases. In fact, the most probable diameter is a strong function of the void volume fraction.

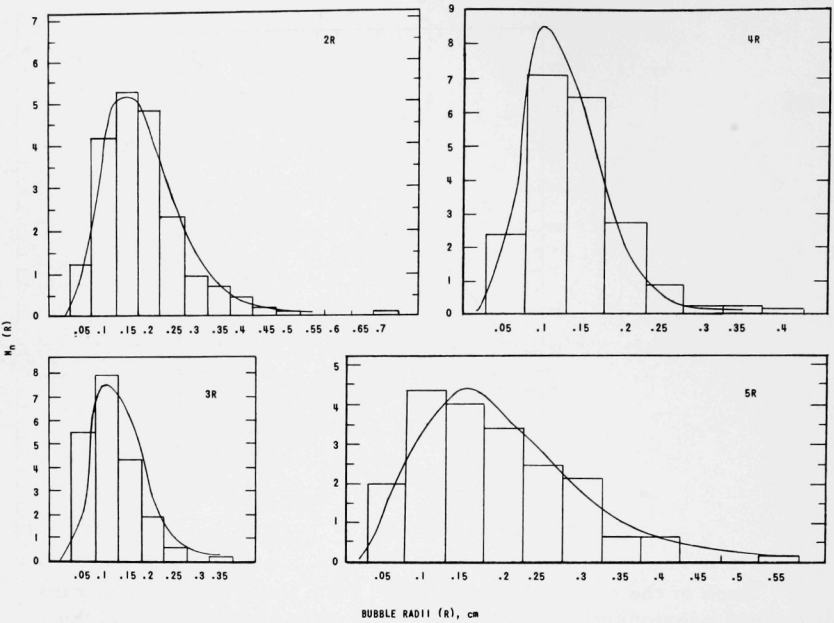

Fig. B-12. Comparison of Measured Bubble Sizes and Correlation

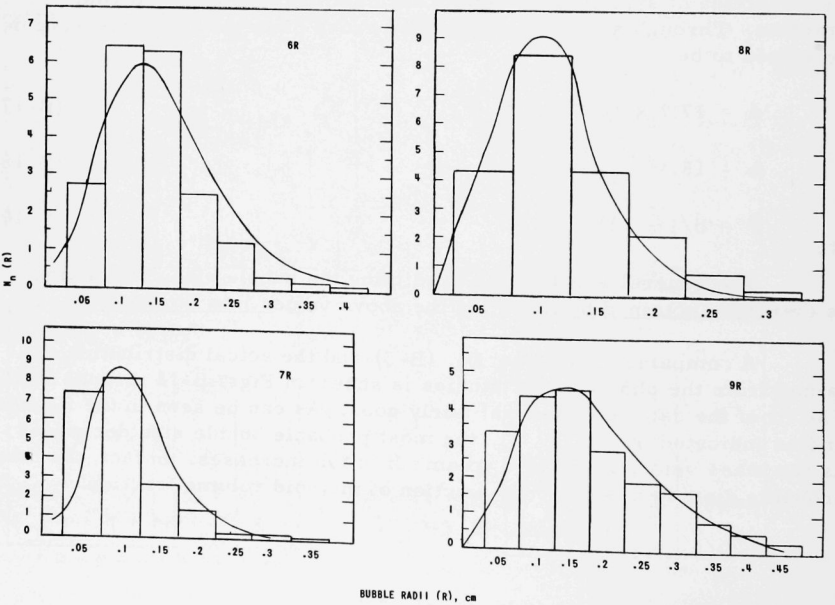

Fig. B-13. Comparison of Measured Bubble Sizes and Correlation

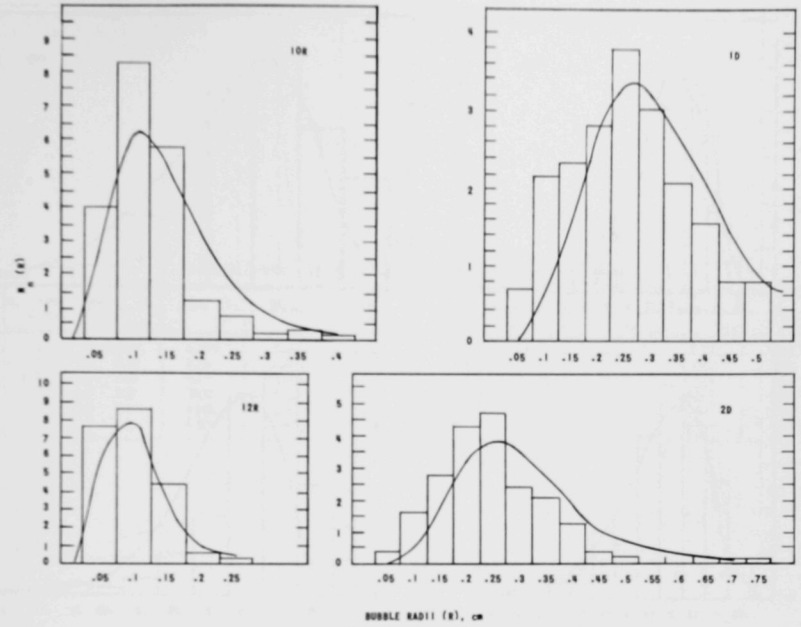

Fig. B-14. Comparison of Measured Bubble Sizes and Correlation

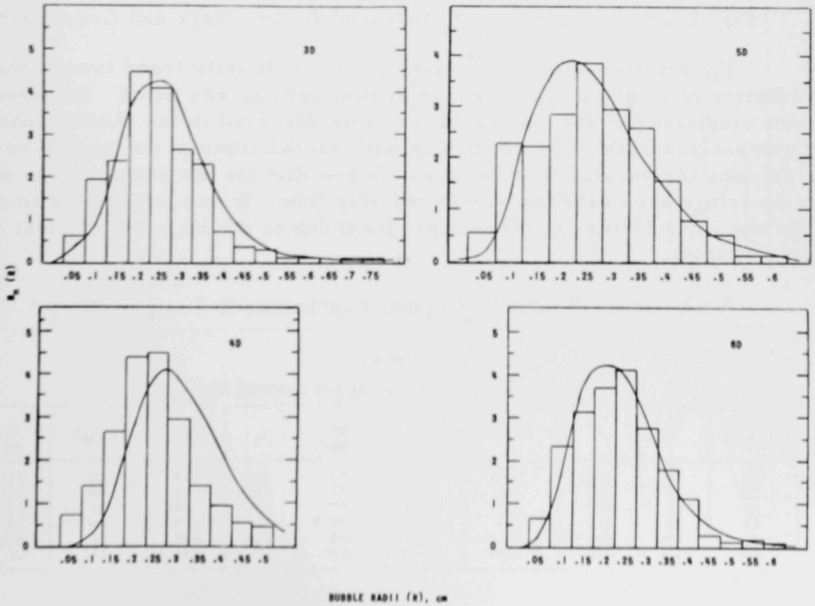

Fig. B-15. Comparison of Measured Bubble Sizes and Correlation

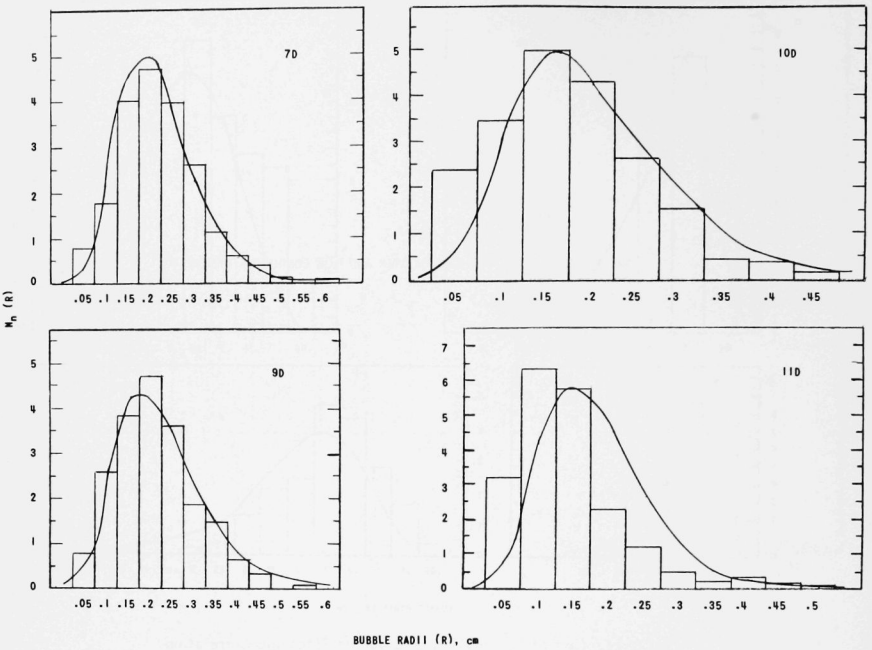

Fig. B-16. Comparison of Measured Bubble Sizes and Correlation

Up to a void volume fraction of 0.40 no definite trend toward the formation of slugs or in the change of flow pattern was noted. However, some clustering of gaseous bubbles can be observed in the photographs. A comparison of the flow conditions with correlations in the literature for predicting the various flow regimes showed that the majority of runs were in the fringe area between bubble and slug flow. It was impossible to extend the voids further in the test program due to the lack of sufficient air flow capacity.

A tabulation of data is presented in Tables B-I and B-II.

Table B-1

AVERAGE BUBBLE SIZE IN THE RISER AND FLOW CONDITIONS THEREIN

Run Number	V_s	α	X x 10^3	$\bar{X}$, mm	Run Number	V_s	α	X x 10^3	$\bar{X}$, mm
1 R	1.5	0.0637	0.2	4.14	7 R	2.15	0.316	1.52	2.1
2 R	1.5	0.170	0.61	3.63	8 R	2.15	0.351	1.96	2.66
3 R	1.5	0.303	1.53	2.05	9 R	2.75	0.0763	0.2	3.17
4 R	1.5	0.346	2.01	2.6	10 R	2.75	0.176	0.61	2.77
5 R	2.15	0.077	0.2	3.3	11 R	2.75	0.307	1.5	2.33
6 R	2.15	0.188	0.62	2.7	12 R	2.75	0.335	2.0	-

Table B-2

AVERAGE BUBBLE SIZE IN THE DOWNCOMER AND FLOW CONDITIONS THEREIN

Run Number	V_s	α	$X \times 10^3$	$\bar{X}$, mm	Run Number	V_s	α	$X \times 10^3$	$\bar{X}$, mm
1 D	0.92	0.0899	0.0142	4.97	7 D	1.3	0.199	0.0796	3.98
2 D	0.92	0.137	0.0164	4.71	8 D	1.3	0.23	0.0983	3.82
3 D	0.92	0.177	0.0228	4.74	9 D	1.6	0.111	0.0579	3.86
4 D	0.92	0.184	0.026	4.64	10 D	1.6	0.165	0.083	3.58
5 D	1.3	0.106	0.0366	5.02	11 D	1.6	2.16	0.106	3.52
6 D	1.3	0.155	0.0574	4.11	12 D	1.6	2.46	0.116	1.91

Appendix C

PHASE DISTRIBUTIONS

The distribution of the phases within the channel was believed to be an important aspect of the carryunder problem since, as mentioned previously, initial preliminary analysis indicated that the major fraction of carryunder would emanate from the peripheral region of the riser. This point is illustrated in a trace photograph taken of the separation process in a typical plenum (see Fig. 5). As can be seen, the trajectory of the air bubbles carried under starts from the peripheral region of the riser. As the distance to the center of the riser decreases, the bubble trajectory intercepts the outer vessel wall, and the probability of bubble escape increases. Progressing further toward the center of the riser, the bubble trajectory intercepts the water surface and the bubble escapes. Thus, it became necessary to establish the distribution of the gas phase if analytical studies of the carryunder problem were to be realistic. If the void distribution across the riser were highly skewed, the weight fraction of the gas phase present in the peripheral region would be much less than if the void distribution were essentially flat. One would therefore expect the carryunder to be less in this instance.

A search of available literature was made, and very little quantitative information could be obtained on the effects of gas and liquid mass velocities, void volume fraction, etc., on the phase distributions. As a result, phase distributions that had been derived during a previous investigation[3] but had not been thoroughly studied, were re-examined. The first set of phase-distribution data was taken with a series of rectangular channels of varying spacings, namely $\frac{1}{8}$, $\frac{1}{4}$, $\frac{1}{2}$, $\frac{3}{4}$, and 1 in. The depth of the channels was 2 in. and their length 4 ft. The distributions were measured by traversing the channel with a collimated gamma beam to obtain a series of average spatial densities. From this variation of spatial density, the distribution of void volume fraction was then computed. An inherent assumption in the analysis was that the void distribution across the depth of the channel was essentially flat. No measurements were made to verify this assumption, since at the time the phase distributions were measured the true void distribution was of secondary importance. However, it is believed that the assumption is a fairly valid one because of the dimension of the channel depth.

The data were correlated by assuming a power-law distribution between local void fraction and position in the channel:

$$\alpha_{\ell} = \alpha_{max} \left(\frac{\ell}{s/2} \right)^{m} \qquad \text{for } 0 < \ell < s/2 \quad , \tag{C-1}$$

where

α_ℓ = local void volume fraction at a distance ℓ

ℓ = the distance from the channel wall

s = the channel spacing

α_{max} = maximum void fraction at s/2 .

A mean symmetrical void distribution was obtained for each run by plotting the distributions over the intervals $0 < \ell < s/2$ and $s/2 < \ell < s$ and drawing a curve which represented the best fit of the data. When substantial deviations existed between the 2 profiles, the run was discarded. Typical runs, in which the procedure was followed, are shown in Fig. C-1. The mean curves were then plotted on logarithmic paper and the slope m of Eq. (C-1) was evaluated. When the distribution was highly skewed, it was impossible to obtain a true slope, since the data did not plot as a linear function. However, mean slopes were faired in even though in some instances they did deviate substantially from the actual phase distribution over certain intervals of $\ell/(s/2)$.

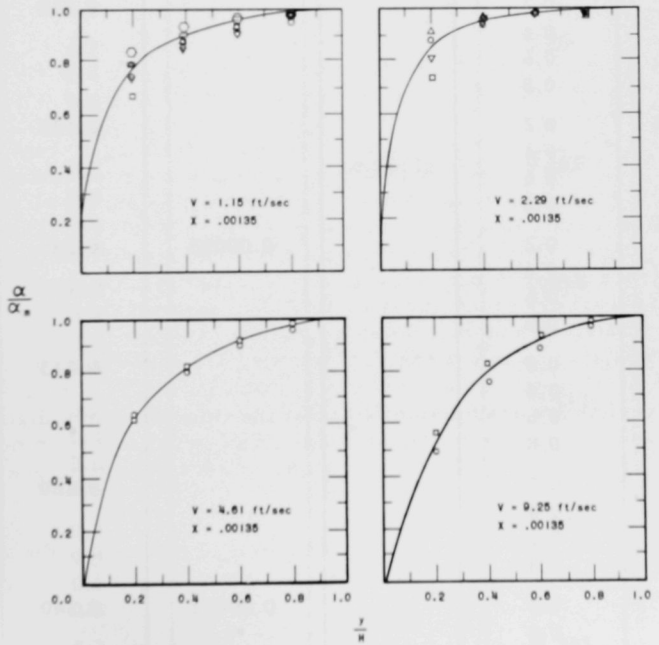

Fig. C-1. Typical Phase Distribution in a Rectangular System

The slopes do, however, represent adequately the trends of the change in the phase distribution as a function of the system parameters, and this was primarily the information that was desired. A tabulation of the local void fractions and the values of the slope m for the series of runs studied is given in Tables C-I through C-III. The effect of the various fluid parameters can readily be seen. It should be noted that a small numerical value of the exponent signifies a flat distribution and a large value a highly skewed distribution.

Table C-I

PHASE DISTRIBUTIONS AND FLOW CONDITIONS
FOR A RECTANGULAR SECTION

α_i	$\ell/(s/2)$	V_s	X	α_{max}	$\bar{\alpha}$
0.0863	0.2	1.15	0.00037	0.144	0.115
0.116	0.4				
0.131	0.6				
0.141	0.8				
0.132	0.2			0.210	0.171
0.168	0.4				
0.188	0.6				
0.202	0.8				
0.0775	0.2			0.133	0.105
0.105	0.4				
0.121	0.6				
0.131	0.8				
0.213	0.2		0.00055	0.285	0.237
0.255	0.4				
0.273	0.6				
0.283	0.8				
0.137	0.2			0.213	0.18
0.187	0.4				
0.205	0.6				
0.212	0.8				
0.163	0.2			0.220	0.184
0.20	0.4				
0.212	0.6				
0.218	0.8				
0.235	0.2		0.00082	0.340	0.288
0.283	0.4				
0.317	0.6				
0.334	0.8				

Table C-I (Cont'd.)

α_i	$\ell/(s/2)$	V_s	X	α_{max}	$\bar{\alpha}$
0.262	0.2	1.15	0.00082	0.363	0.314
0.316	0.4				
0.342	0.6				
0.355	0.8				
0.263	0.2			0.348	0.304
0.317	0.4				
0.341	0.6				
0.346	0.8				
0.233	0.2			0.307	0.272
0.275	0.4				
0.295	0.6				
0.305	0.8				
0.213	0.2			0.287	0.258
0.255	0.4				
0.275	0.6				
0.283	0.8				
0.173	0.2			0.20	0.196
0.189	0.4				
0.196	0.6				
0.194	0.8				
0.352	0.2		0.00125	0.465	0.410
0.410	0.4				
0.440	0.6				
0.455	0.8				
0.363	0.2			0.453	0.410
0.410	0.4				
0.435	0.6				
0.448	0.8				
0.238	0.2			0.353	0.299
0.312	0.4				
0.345	0.6				
0.350	0.8				
0.28	0.2			0.350	0.312
0.323	0.4				
0.342	0.6				
0.347	0.8				
0.257	0.2			0.335	0.296
0.295	0.4				
0.317	0.6				
0.330	0.8				

Table C-I (Cont'd.)

α_i	$\ell/(s/2)$	V_s	X	α_{max}	$\bar{\alpha}$
0.237	0.2	1.15	0.00125	0.285	0.266
0.270	0.4				
0.280	0.6				
0.283	0.8				
0.393	0.2		0.00175	0.493	0.442
0.455	0.4				
0.478	0.6				
0.487	0.8				
0.387	0.2			0.513	0.450
0.450	0.4				
0.488	0.6				
0.505	0.8				
0.422	0.2			0.517	0.468
0.475	0.4				
0.495	0.6				
0.510	0.8				
0.482	0.2			0.591	0.536
0.550	0.4				
0.577	0.6				
0.587	0.8				
0.395	0.2		0.00255	0.517	0.454
0.470	0.4				
0.498	0.6				
0.512	0.8				
0.410	0.2			0.550	0.476
0.482	0.4				
0.523	0.6				
0.543	0.8				
0.390	0.2			0.510	0.452
0.450	0.4				
0.485	0.6				
0.500	0.8				
0.338	0.2			0.455	0.390
0.395	0.4				
0.430	0.6				
0.448	0.8				

Table C-I (Cont'd.)

α_i	$\ell(s/2)$	V_s	X	α_{max}	$\overline{\alpha}$
0.553	0.2	1.15	0.0033	0.620	0.578
0.585	0.4				
0.60	0.6				
0.610	0.8				
0.472	0.2		0.0043	0.663	0.568
0.570	0.4				
0.623	0.6				
0.650	0.8				
0.485	0.2			0.60	0.550
0.555	0.4				
0.585	0.6				
0.595	0.8				
0.40	0.2			0.491	0.470
0.465	0.4				
0.488	0.6				
0.490	0.8				
0.513	0.2			0.618	0.556
0.573	0.4				
0.598	0.6				
0.612	0.8				
0.121	0.2	1.54	0.00037	0.188	0.143
0.161	0.4				
0.179	0.6				
0.186	0.8				
0.113	0.2			0.168	0.143
0.148	0.4				
0.159	0.6				
0.165	0.8				
0.215	0.2		0.00055	0.283	0.247
0.263	0.4				
0.277	0.6				
0.280	0.8				
0.308	0.2		0.00082	0.358	0.335
0.342	0.4				
0.352	0.6				
0.357	0.8				
0.460	0.2		0.00135	0.519	0.475
0.495	0.4				
0.505	0.6				
0.515	0.8				

Table C-I (Cont'd.)

α_i	$\ell/(s/2)$	V_s	X	α_{max}	$\overline{\alpha}$
0.445	0.2	1.54	0.00135	0.497	0.475
0.482	0.4				
0.490	0.6				
0.495	0.8				
0.302	0.2			0.369	0.340
0.343	0.4				
0.357	0.6				
0.364	0.8				
0.310	0.2			0.367	0.340
0.355	0.4				
0.364	0.6				
0.366	0.8				
0.488	0.2		0.00175	0.558	0.442
0.537	0.4				
0.548	0.6				
0.555	0.8				
0.503	0.2			0.564	0.442
0.540	0.4				
0.552	0.6				
0.562	0.8				
0.425	0.2		0.00257	0.512	0.472
0.483	0.4				
0.500	0.6				
0.510	0.8				
0.485	0.2		0.0043	0.660	0.594
0.580	0.4				
0.625	0.6				
0.650	0.8				
0.525	0.2			0.658	0.594
0.605	0.4				
0.635	0.6				
0.653					
0.182	0.2	2.29	0.00037	0.214	0.205
0.205	0.4				
0.213	0.6				
0.213	0.8				
0.170	0.2			0.215	0.205
0.193	0.4				
0.208	0.6				
0.213	0.8				

Table C-I (Cont'd.)

α_i	$\ell/(s/2)$	V_s	X	α_{max}	$\bar{\alpha}$
0.356	0.2	2.29	0.00082	0.388	0.365
0.375	0.4				
0.383	0.6				
0.387	0.8				
0.354	0.2			0.377	0.365
0.373	0.4				
0.376	0.6				
0.376	0.8				
0.273	0.2			0.353	0.336
0.325	0.4				
0.338	0.6				
0.347	0.8				
0.440	0.2		0.00135	0.5	0.452
0.477	0.4				
0.492	0.6				
0.498	0.8				
0.435	0.2			0.475	0.452
0.460	0.4				
0.470	0.6				
0.474	0.8				
0.308	0.2			0.420	0.394
0.398	0.4				
0.415	0.6				
0.418	0.8				
0.330	0.2			0.410	0.394
0.4	0.4				
0.408	0.6				
0.409	0.8				
0.488	0.2		0.00175	0.557	0.542
0.532	0.4				
0.548	0.6				
0.555	0.8				
0.500	0.2			0.60	0.570
0.568	0.4				
0.590	0.6				
0.598	0.8				

Table C-I (Cont'd.)

α_i	$\ell/(s/2)$	V_s	X	α_{max}	$\bar{\alpha}$
0.530	0.2	2.29	0.00257	0.618	0.584
0.587	0.4				
0.603	0.6				
0.612	0.8				
0.550	0.2			0.622	0.58
0.590	0.4				
0.610	0.6				
0.620	0.8				
0.435	0.2			0.538	0.55
0.516	0.4				
0.535	0.6				
0.537	0.8				
0.440	0.2			0.588	0.55
0.525	0.4				
0.568	0.6				
0.585	0.8				
0.498	0.2		0.0033	0.615	0.56
0.575	0.4				
0.598	0.6				
0.610	0.8				
0.530	0.2			0.620	0.56
0.585	0.4				
0.610	0.6				
0.615	0.8				
0.498	0.2		0.0043	0.615	0.6
0.568	0.4				
0.600	0.6				
0.608	0.8				
0.552	0.2			0.637	0.6
0.602	0.4				
0.622	0.6				
0.630	0.8				
0.315	0.2	4.61	0.00125	0.430	0.4
0.390	0.4				
0.415	0.6				
0.425	0.8				

Table C-I (Cont'd.)

α_i	$\ell/(s/2)$	V_s	X	α_{max}	$\overline{\alpha}$
0.308	0.2	4.61	0.00125	0.440	0.4
0.395	0.4				
0.422	0.6				
0.432	0.8				
0.458	0.2		0.00175	0.553	0.54
0.532	0.4				
0.550	0.6				
0.553	0.8				
0.453	0.2			0.610	0.54
0.518	0.4				
0.555	0.6				
0.588	0.8				
0.465	0.2		0.0033	0.562	0.51
0.520	0.4				
0.548	0.6				
0.555	0.8				
0.542	0.2		0.00255	0.665	0.59
0.605	0.4				
0.640	0.6				
0.658	0.8				
0.528	0.2			0.628	0.59
0.588	0.4				
0.612	0.6				
0.626	0.8				
0.412	0.2			0.578	0.56
0.448	0.4				
0.538	0.6				
0.562	0.8				
0.408	0.2			0.652	0.56
0.520	0.4				
0.572	0.6				
0.615	0.8				
0.420	0.2		0.0033	0.55	0.51
0.508	0.4				
0.538	0.6				
0.548	0.8				

Table C-I (Cont'd.)

α_i	$\ell/(s/2)$	V_s	X	α_{max}	$\overline{\alpha}$
0.250	0.2	4.61	0.00082	0.325	0.31
0.295	0.4				
0.315	0.6				
0.322	0.8				
				0.360	0.31
0.227	0.2				
0.275	0.4				
0.324	0.6				
0.345	0.8				
0.270	0.2		0.00135	0.424	0.35
0.345	0.4				
0.390	0.6				
0.415	0.8				
				0.413	0.35
0.255	0.2				
0.355	0.4				
0.380	0.6				
0.403	0.8				
0.353	0.2		0.00257	0.542	0.504
0.470	0.4				
0.518	0.6				
0.540	0.8				
				0.558	0.504
0.380	0.2				
0.500	0.4				
0.535	0.6				
0.552	0.8				
0.425	0.2		0.0043	0.620	0.59
0.548	0.4				
0.590	0.6				
0.612	0.8				
				0.670	0.59
0.448	0.2				
0.570	0.4				
0.630	0.6				
0.638	0.8				
0.227	0.2		0.00082	0.370	0.32
0.295	0.4				
0.335	0.6				
0.360	0.8				

Table C-I (Cont'd.)

a_i	$\ell/(s/2)$	V_s	X	a_{max}	$\overline{a}$
0.245	0.2	4.61	0.00082	0.365	0.32
0.312	0.4				
0.335	0.6				
0.352	0.8				
0.145	0.2	9.25	0.00082	0.3	0.37
0.225	0.4				
0.268	0.6				
0.290	0.8				
0.225	0.2			0.422	0.37
0.333	0.4				
0.383	0.6				
0.404	0.8				
0.183	0.2		0.00135	0.370	0.406
0.280	0.4				
0.377	0.6				
0.360	0.8				
0.255	0.2			0.450	0.406
0.370	0.4				
0.418	0.6				
0.442	0.8				
0.515	0.2		0.00257	0.728	0.53
0.640	0.4				
0.70	0.6				
0.723	0.8				
0.315	0.2			0.598	0.53
0.468	0.4				
0.555	0.6				
0.590	0.8				
0.395	0.2		0.0043	0.550	0.61
0.480	0.4				
0.525	0.6				
0.545	0.8				
0.420	0.2			0.667	0.61
0.558	0.4				
0.628	0.6				
0.655	0.8				

Table C-I (Cont'd.)

α_i	$\ell/(s/2)$	V_s	X	α_{max}	$\overline{\alpha}$
0.196	0.2	9.25	0.00082	0.296	0.306
0.270	0.4				
0.292	0.6				
0.295	0.8				
0.220	0.2			0.321	0.31
0.273	0.4				
0.300	0.6				
0.315	0.8				
0.250	0.2			0.323	0.32
0.307	0.4				
0.320	0.6				
0.321	0.8				
0.277	0.2			0.328	0.32
0.320	0.4				
0.326	0.6				
0.327	0.8				
0.268	0.2		0.00125	0.403	0.39
0.340	0.4				
0.375	0.6				
0.395	0.8				
0.307	0.2			0.414	0.39
0.375	0.4				
0.397	0.6				
0.408	0.8				
0.260	0.2			0.425	0.41
0.340	0.4				
0.380	0.6				
0.410	0.8				
0.260	0.2			0.468	0.41
0.370	0.4				
0.420	0.6				
0.450	0.8				
0.306	0.2		0.00175	0.450	0.446
0.383	0.4				
0.422	0.6				
0.440	0.8				

Table C-I (Cont'd.)

α_i	$\ell/(s/2)$	V_s	X	α_{max}	$\overline{\alpha}$
0.365	0.2	9.25	0.00255	0.473	0.5
0.420	0.4				
0.445	0.6				
0.463	0.8				
0.337	0.2			0.460	0.5
0.402	0.4				
0.432	0.6				
0.450	0.8				
0.332	0.2			0.535	0.51
0.448	0.4				
0.502	0.6				
0.530	0.8				
0.378	0.2			0.545	0.51
0.480	0.4				
0.518	0.6				
0.54	0.8				
0.370	0.2		0.0043	0.531	0.53
0.472	0.4				
0.518	0.6				
0.529	0.8				
0.410	0.2			0.587	0.53
0.502	0.4				
0.548	0.6				
0.572	0.8				
0.388	0.2			0.578	0.6
0.485	0.4				
0.533	0.6				
0.563	0.8				
0.390	0.2			0.655	0.6
0.542	0.4				
0.610	0.6				
0.642	0.8				

Table C-II

TABLE OF THE EXPONENT m IN EQ. (C-1) AND CORRELATING PARAMETERS FOR A PRESSURE OF 14.7 PSI

Velocity, ft/sec	Mean Void Fraction	m	Velocity, ft/sec	Mean Void Fraction	m
1.35	0.135	0.25	4.61	0.30	0.185
1.35	0.142	0.16	4.61	0.32	0.215
1.35	0.20	0.123	4.61	0.35	0.225
1.35	0.247	0.089	4.61	0.4	0.14
1.35	0.27	0.113	4.61	0.5	0.17
1.35	0.30	0.098	4.61	0.52	0.107
1.35	0.335	0.060	4.61	0.54	0.12
1.35	0.35	0.060	4.61	0.58	0.14
1.35	0.39	0.060	9.25	0.365	0.315
1.35	0.41	0.060	9.25	0.40	0.24
1.35	0.45	0.110	9.25	0.41	0.28
1.35	0.455	0.083	9.25	0.45	0.175
1.35	0.465	0.073	9.25	0.50	0.170
1.35	0.53	0.091	9.25	0.53	0.225
1.35	0.535	0.052	9.25	0.57	0.18
1.35	0.57	0.061	9.25	0.62	0.165

Table C-III

PHASE DISTRIBUTIONS AND FLOW CONDITIONS IN A CIRCULAR PIPE

(P = 600 psi)

Pipe Size	αmax	α at r/R = 0.4	α at r/R = 0.6	α at r/R = 0.8	αmeas	X	Superficial Velocity, ft/sec
2	0.633	0.456	0.311	0.177	0.262	0.017	2.3
2	0.325	0.264	0.222	0.172	0.189	0.013	2.03
2	0.651	0.501	0.358	0.197	0.280	0.021	2.08
2	0.696	0.566	0.446	0.300	0.364	0.031	2.21
2	0.815	0.671	0.539	0.361	0.433	0.043	2.21
2	0.641	0.59	0.482	0.283	0.33	0.0262	1.63
3/4	1.0	0.868	0.694	0.42	0.542	0.0262	5.58
2	0.851	0.813	0.698	0.438	0.481	0.067	1.63
3/4	1.0	0.92	0.82	0.473	0.576	0.0685	5.56
2	0.639	0.625	0.528	0.307	0.36	0.031	1.66
2	0.585	0.514	0.383	0.190	0.25	0.014	1.59
3/4	0.859	0.662	0.454	0.225	0.355	0.0139	5.45
3/4	0.924	0.748	0.532	0.266	0.417	0.0306	5.80
2	0.675	0.598	0.464	0.260	0.360	0.031	1.70
2	0.566	0.486	0.364	0.187	0.264	0.017	1.63
3/4	0.874	0.709	0.495	0.23	0.366	0.0173	5.56

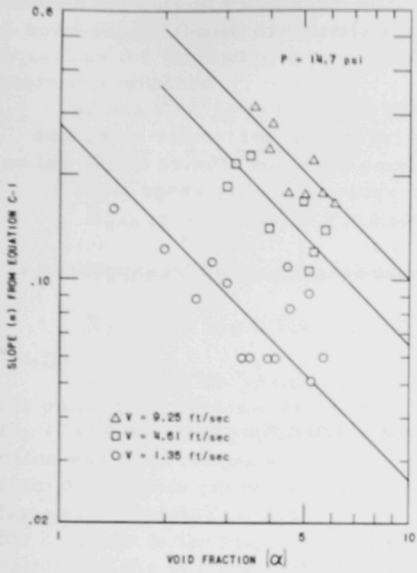

Fig. C-2. Effect of Void Fraction and Liquid Velocity on Slope m of Eq. (C-1).

The slope m as a function of the mean void fraction $\bar{\alpha}$ and the liquid velocity is shown in Fig. C-2. A family of curves is obtained for different superficial liquid velocities. The exponent m decreases as the average void content of the fluid increases, and increases as the superficial liquid velocity increases. It is believed, however, that as $\bar{\alpha}$ continued to increase the slope m would reach an asymptotic value. By cross plotting with respect to velocity, the following relationship for the slope m was obtained:

$$m = 0.024\ (V_s)^{0.666/\bar{\alpha}} \quad . \quad (C\text{-}2)$$

As a result, the phase distribution for air-water mixtures at atmospheric pressure may be estimated from the following expression:

$$\frac{\alpha_\ell}{\alpha_{max}} = \left(\frac{\ell}{s/2}\right)^{0.024(V_s)^{0.666/\bar{\alpha}}} \quad , \quad (C\text{-}3)$$

where

α_ℓ = void fraction at ℓ

α_{max} = maximum void fraction at $s/2$

s = the channel spacing

ℓ = distance from edge of the channel

$\bar{\alpha}$ = mean void fraction

V_s = superficial liquid velocity

Some information on the phase distribution at higher pressures has recently become available. Haywood et al.,[19] published the results of an extensive study of 2-phase flow including data on the phase distributions in a circular pipe. The true local void distribution was not measured but was deduced from chordal density measurements taken at 4 positions across the pipe. Sufficient profile data were not included to yield quantitative effects of system parameters which could be compared with the data from rectangular channels. A cursory analysis of the 600-lb void profile data,

however, indicated that the phase distribution became flatter as the mixture quality or void fraction increased. This is similar to the effect observed on the air-water loop.

A technique similar to that used by Haywood et al.,[19] and by Schwarz[20] to obtain void profiles from traverses of circular tubes was applied to a second set of data obtained from previous studies at 600 psi on pipes of 2-in. and $\frac{3}{4}$-in. diameters and covering a quality range from 0 to 0.07.

It was assumed that the void volume fraction could be expressed as a function of the polynomial

$$\alpha_r = \sigma + a\left(\frac{r}{R}\right)^2 + b\left(\frac{r}{R}\right)^4 + c\left(\frac{r}{R}\right)^6 \quad . \tag{C-4}$$

Therefore, at any chord at distance Z from the center (see Fig. C-3),

$$\overline{\alpha}_Z = \int_0^Y \alpha_r \, dy/Y \quad , \tag{C-5}$$

where

$$y = r \sin [\arccos Z/r] \quad .$$

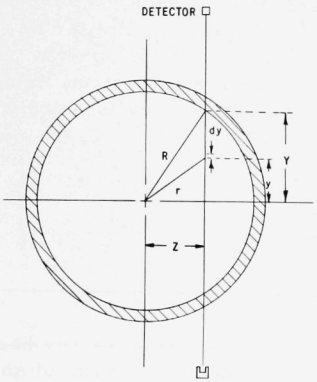

Fig. C-3
Cross-sectional Diagram of Circular Conduit

Substituting Eq. (C-4) into Eq. (C-5) and integrating,

$$\overline{\alpha}_Z = \sigma + \frac{a}{R^2}\left(\frac{Y^2}{3} + Z^2\right) + \frac{b}{R^4}\left(\frac{Y^4}{5} + \frac{2}{3}Y^2Z^2 + Z^4\right) + \frac{c}{R^6}\left(\frac{Y^6}{7} + \frac{3}{5}Y^4Z^2 + Y^2Z^4 + Z^6\right) \quad . \tag{C-6}$$

The 4 constants are evaluated by taking mean density readings at Z = 0, Z = 0.4 R, Z = 0.6 R, and Z = 0.8 R. Substituting the mean $\bar{\alpha}$ into the equations for the 4 chordal positions and solving them simultaneously, there are obtained

$$\bar{\alpha}_{z=0} = \sigma + \frac{a}{3} + \frac{b}{5} + \frac{c}{7} \qquad \text{(C-7)}$$

$$\bar{\alpha}_{z=0.4R} = \sigma + 0.44a + 0.256b + 0.1779c \qquad \text{(C-8)}$$

$$\bar{\alpha}_{z=0.6R} = \sigma + 0.573a + 0.365b + 0.255c \qquad \text{(C-9)}$$

$$\bar{\alpha}_{z=0.8R} = \sigma + 0.76a + 0.587b + 0.465c \qquad \text{(C-10)}$$

To check the validity of the void profiles obtained in this manner, the polynomial obtained from the simultaneous solution of Eq. (C-7) through Eq. (C-10) was integrated to obtain a mean void volume fraction. This value was then compared with the mean steam volume fraction obtained from a complete traverse of the channel. The 2 mean steam volume fractions are tabulated in Table C-IV. As can be seen, the agreement between the 2 values in the majority of the cases is excellent, thus attesting to the validity of the derived void profiles. The void profiles were then reduced to dimensionless form and plotted in the same manner as the data from rectangular channels. The slopes of the α/α_{max} versus r/R plots were obtained in the same manner mentioned earlier and plotted versus the mean void fraction as shown in Fig. C-4, and tabulated in Table C-V. As can be seen, a family of curves was derived which is very similar to that obtained from the air-water data. Again, the slope m was found to vary inversely with the mean void fraction $\bar{\alpha}$ and with the superficial liquid velocity to the two-thirds power. The 600-psi family of curves is merely displaced upward in relation to the air-water data.

Table C-IV

COMPARISON OF $\bar{\alpha}_{meas}$ VERSUS $\bar{\alpha}_{calc}$ FOR A CIRCULAR SECTION USING THE METHOD OF HAYWOOD ET AL., AND OF SCHWARZ

Run	α_{meas}	α_{calc}	Run	α_{meas}	α_{calc}
62	0.262	0.252	168	0.488	0.499
55	0.189	0.187	169	0.36	0.398
52	0.280	0.284	170	0.25	0.304
45	0.364	0.366	171	0.355	0.367
44	0.433	0.429	172	0.417	0.425
164	0.33	0.367	173	0.36	0.36
165	0.542	0.537	174	0.264	0.286
166	0.481	0.525	175	0.366	0.395
167	0.576	0.628			

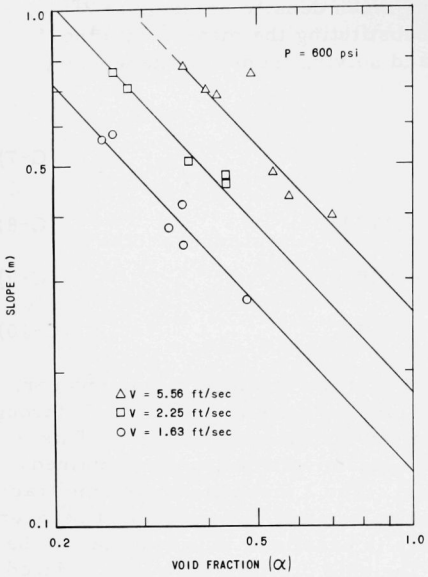

Fig. C-4

Effect of Steam Volume Fraction and Liquid Velocity on Slope m of Eq. (C-11)

Table C-V

TABLE OF VALUES FOR THE EXPONENT m IN EQ. (C-11) AND CORRELATING PARAMETERS
(P = 600 psi)

V	$\overline{\alpha}$	m
1.63	0.264	0.575
1.63	0.360	0.45
1.63	0.25	0.562
1.63	0.36	0.32
1.63	0.48	0.275
1.63	0.34	0.375
2.25	0.433	0.48
2.25	0.433	0.475
2.25	0.364	0.5
2.25	0.28	0.70
2.25	0.262	0.755
5.56	0.40	0.70
5.56	0.42	0.687
5.56	0.36	0.78
5.56	0.575	0.43
5.56	0.542	0.483

The higher values of m indicate the void profiles at 600 psi are more highly skewed. The function describing the phase distribution data at 600 psi is

$$\alpha_r/\alpha_{max} = (r/R)^{0.1(V_s)^{0.666}/\bar{\alpha}} \qquad \text{(C-11)}$$

It should be noted that there may be some geometrical effect on the phase distribution because of the manner in which the data were taken for the air-water study. The larger values of m obtained for liquid velocities of 4.61 and 9.25 ft/sec are associated with channel widths of $\frac{1}{4}$ and $\frac{1}{8}$ in. The lower values of m corresponding to a velocity of ~1.35 ft/sec are associated with the $\frac{3}{4}$-in. and 1-in.-width channel. The same holds true for the 600-psi data. Unfortunately, virtually no data were obtained for varying velocities in the individual channels. The fact, however, that the geometric range covered was quite large ($\frac{1}{8}$-in. spacing to 2-in. pipe) and that the velocity effect was the same indicates that the geometrical effect, if one exists, is quite small.

The relationship between the chordal-mean void volume fraction obtained at the center line of the tube cross section and the mean void volume fraction for the whole pipe was also investigated. It has been proposed by a number of investigators that the mean void volume fraction of a pipe can be estimated with sufficient accuracy if the centerline value is known. The values of the ratio that has been proposed range from ~0.80 to 0.86. The values of the ratio derived from the 600-psi data are tabulated in Table C-VI and plotted in Fig. C-5 as a function of the average void volume fraction.

Table C-VI

COMPARISON OF AVERAGE VOIDS WITH MAXIMUM AND CENTERLINE VOIDS

$\bar{\alpha}_{meas}$	α_{max}	$\bar{\alpha}/\alpha_{max}$	$\bar{\alpha}_{C_L}$	$\bar{\alpha}/\bar{\alpha}_{C_L}$	Superficial Velocity, ft/sec
0.189	0.325	0.582	0.23	0.822	2.03
0.262	0.633	0.414	0.37	0.708	2.3
0.280	0.651	0.43	0.40	0.700	2.08
0.364	0.696	0.522	0.472	0.771	2.21
0.433	0.815	0.531	0.555	0.780	2.21
0.33	0.641	0.515	0.468	0.705	1.63
0.542	1.000	0.542	0.700	0.774	5.58
0.481	0.851	0.565	0.653	0.736	1.63
0.576	1.00	0.576	0.800	0.72	5.56
0.488	1.00	0.488	0.712	0.685	5.69
0.36	0.639	0.563	0.493	0.730	1.66
0.25	0.585	0.427	0.400	0.625	1.59
0.355	0.859	0.413	0.520	0.683	5.45
0.417	0.924	0.451	0.586	0.711	5.80
0.360	0.675	0.533	0.470	0.765	1.70
0.264	0.566	0.466	0.380	0.695	5.75
0.366	0.874	0.418	0.550	0.665	5.56

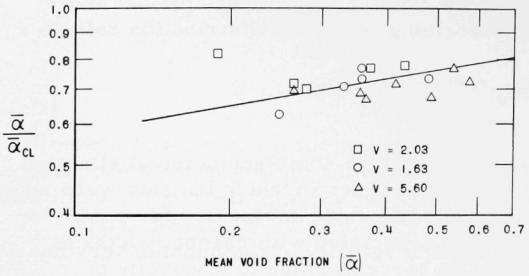

Fig. C-5

Variation of the Ratio $\bar{\alpha}/\bar{\alpha}_{C_L}$ with $\bar{\alpha}$

It is apparent that there is a substantial variation in the ratio (0.625-0.82) over the void and velocity parameter range studied. The ratio appears to increase as the average channel void fraction increases and the superficial velocity decreases. The variations are not great, but it appears doubtful that a mean value of the ratio could be utilized over wide parameter range and still yield accurate information.

Appendix D

SLIP RATIOS IN DOWN FLOW

The magnitude of carryunder which occurs in a given system is strongly affected by the slippage between the phases in the downcomer. The downcomer void fraction is especially sensitive to the downflow slip ratio. In downflow, the gas-liquid velocity ratio may vary between 0 and 1. If flow conditions are such that the buoyancy velocity of the bubbles very nearly equals the downward liquid velocity, the slip ratio approaches zero and the void fraction increases sharply. If the downward liquid velocity is very large in comparison with the upward buoyancy of the bubbles, the slip ratio would then tend toward unity.

A separate study was undertaken to provide information on the effects of parameters such as velocity, mixture quality, and pressure on the downflow slip ratio. The initial phase of the study was carried out on the atmospheric air-water loop. Data on downflow slip ratios were obtained as part of the carryunder study. The downcomer mixture quality and void fractions were measured, and the slip ratio was calculated from the continuity equation.

High-pressure data were obtained from the 2500-psi Heat Transfer and Fluid Flow Test Facility. A series of tests were made in which data were taken randomly over a velocity range from 0.5 to 5 ft/sec at pressures of 600, 1000, and 1500 psi. A schematic of the loop arrangement used in these tests is given in Fig. D-1. The downflow slip ratios were obtained from the adiabatic segment of piping denoted as the downflow test section. The void volume fraction α was determined by 3 methods: namely, by Potter Meter,[21] gamma traversing, and from differential static pressure measurements. The 3 techniques were employed to insure the accuracy of the data. The values of the mean void fraction determined by the 3 methods checked very well. As a result, the differential static pressure-drop technique was used for determining the steam volume fraction in the majority of runs, since it was the simplest. The measurements were taken in the lower portion of the section to allow the flow to stabilize after completing the 180° turn at the top of the section. The steam weight fractions X were determined by a heat balance on the heated test section and checked by a heat balance on the downcomer cooler.

The correlating techniques that were used on upflow slip ratio data were applied to the downflow data. Initially, the slip ratio was plotted versus the superficial and true liquid velocity in the hope of obtaining simplified relationships. Substantial success had been obtained with such plots for the upflow air-water data.

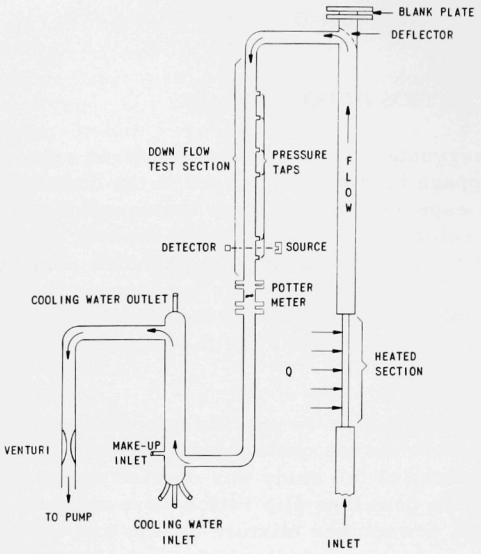

Fig. D-1

Schematic of Loop Arrangement

A plot of the air-water slip ratios versus the superficial liquid velocity is shown in Fig. D-2. As can be seen, there is considerable scatter, but it is not excessive except in the region of about 1.5 ft/sec. The exceptional scatter in this velocity region is unexplained. The scattering itself is due primarily to the mixture quality, that is, the data points "stack up" with increasing quality.

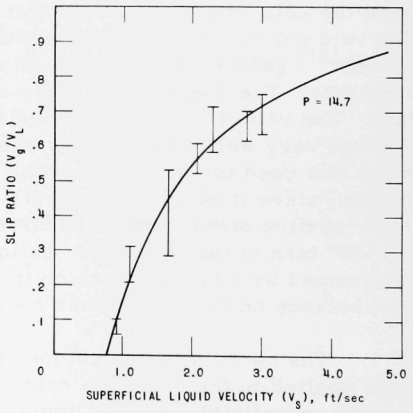

Fig. D-2

Air-Water Slip Ratios Versus Superficial Downcomer Velocity

The slip ratios were then plotted as a function of the true liquid velocity in an attempt to eliminate the quality effect. As the mixture quality is increased for a fixed superficial liquid velocity, the true liquid velocity increases due to the corresponding increase in the void fraction. The limited success obtained from this correlation attempt is shown in Fig. D-3. The "stacking" is reduced somewhat, especially in the lower velocity range, but the effect was not large enough.

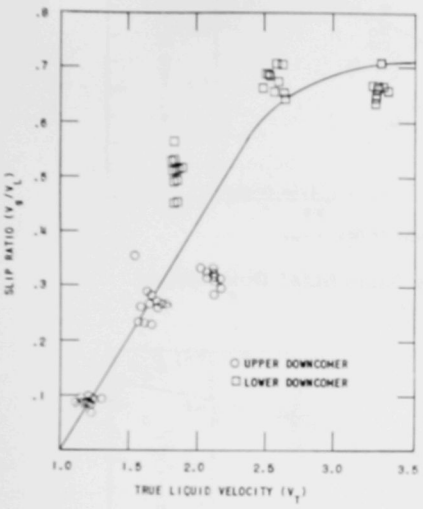

Fig. D-3. Air-Water Slip Ratios Versus True Downcomer Liquid Velocity

Plots of the high-pressure slip ratios versus the superficial velocities for downflow are shown in Figs. D-4 to D-6. As can be seen, a relationship appears to exist between the 2 variables. The scatter of the data, again, while large, is not excessive. Virtually the same line can be drawn through each set of data, that is, no significant pressure effect appears to exist, although the 600-psi data are slightly lower in the low-velocity range and slightly higher in the higher-velocity range. The air-water data shown in Fig. D-2 likewise fall within the range of the high-pressure data. These results are somewhat surprising, since a significant pressure effect on the slip ratio has been found for upflow conditions when the data were plotted in this manner. There are numerous indications of this trend in the available literature. A similar pressure effect on the slip ratio was expected in downflow. As the critical point is approached, the slip ratio must approach unity. Also, it should be noted that the buoyancy forces decrease with increasing pressure. Therefore, one would expect increasing downflow slip ratios as the pressure is increased. A study of the bubble sizes and coalescence as the temperature and pressure is raised might shed some light on this matter.

Plots of the slip ratios as a function of the true liquid velocity for high-pressure data are shown in Figs. D-7, D-8, and D-9. A random pressure effect appears to exist. For a given true liquid velocity the smallest slip ratios are obtained at 600 psi, and the highest at atmospheric conditions, 14.7 psi and 80°F. The 1000-psi and 1500-psi data are virtually the same and fall between the 600-psi and 14.7-psi sets of data. It should also be noted that there is a considerable increase in the scatter of the slip-ratio data when plotted as a function of the true liquid velocity.

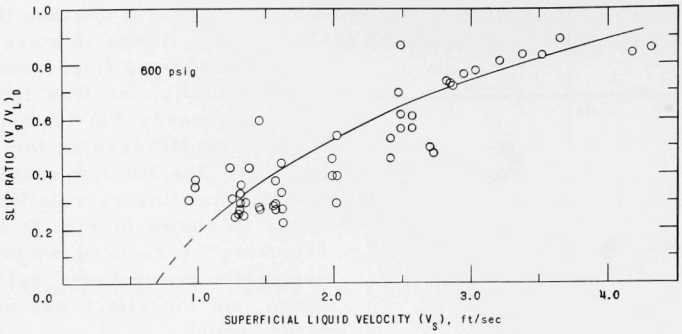

Fig. D-4. Slip Ratio Versus Superficial Downcomer Velocity at 600 psi

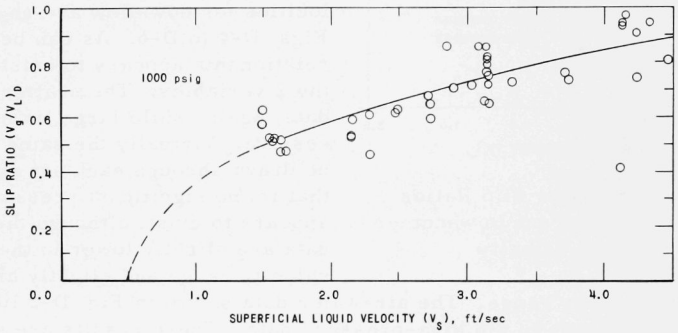

Fig. D-5. Slip Ratio Versus Superficial Downcomer Velocity at 1000 psi

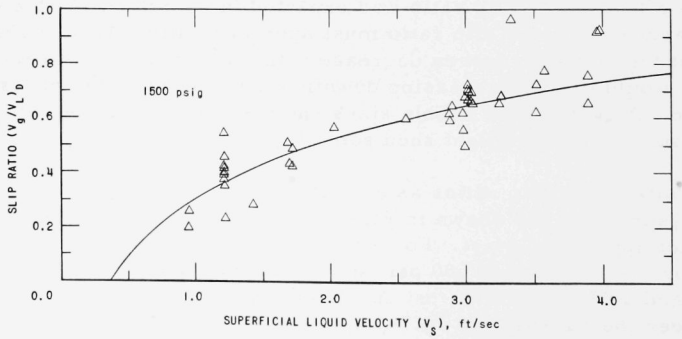

Fig. D-6. Slip Ratio Versus Superficial Downcomer Velocity at 1500 psi

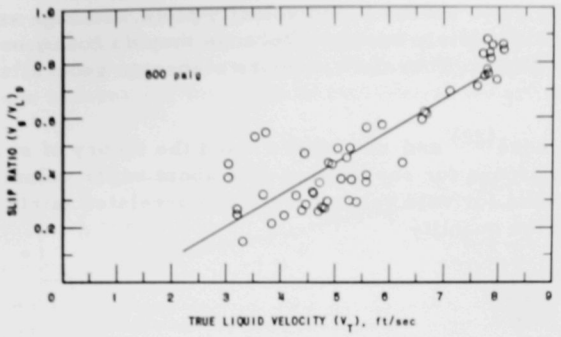

Fig. D-7. Slip Ratio Versus True Downcomer Velocity at 600 psi

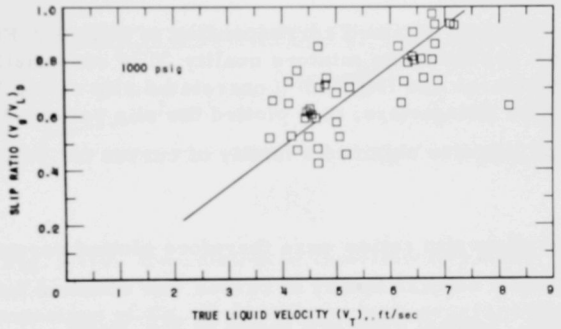

Fig. D-8. Slip Ratio Versus True Downcomer Velocity at 1000 psi

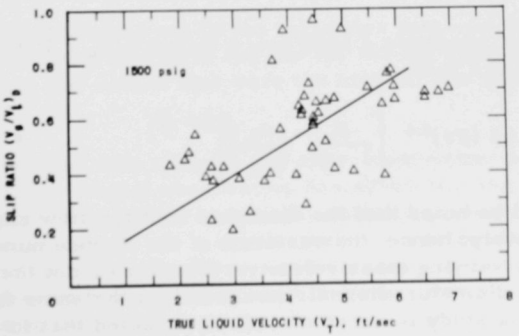

Fig. D-9. Slip Ratio Versus True Downcomer Velocity at 1500 psi

The slip ratio versus liquid velocity plots, although very useful, are not considered completely adequate because they do not incorporate the observed quality effect. Therefore, a more elaborate generalized correlation was attempted.

Kutateladze[22] and coworkers used the theory of similarity to derive dimensionless groups for correlating data about vapor volume fraction. They found that the data for void volume fraction correlated fairly well when plotted versus the quantity

$$\frac{X}{1 - X}\left(\frac{\rho_L}{\rho_g}\right) \quad ,$$

where

X = Weight flow rate of gas/Weight flow rate of liquid.

A family of curves was obtained corresponding to different Froude Numbers, V^2/gD. For low gas rates the mixture quality X is essentially equal to X. Recently, Marchaterre and Hoglund[3] correlated slip ratios by means of virtually the same parameters; they plotted the slip ratios versus the quantity $\frac{X}{1 - X}\left(\frac{\rho_L}{\rho_g}\right)$ and likewise obtained a family of curves for various Froude numbers.

The downflow slip ratios were therefore plotted versus the quantity $\frac{X}{1 - X}\left(\frac{\rho_L}{\rho_g}\right)$, and a similar family of curves was obtained for the various Froude numbers. Typical plots are shown in Fig. D-10.

By a series of cross plots, the following empirical relationship was obtained for calculating the downflow slip ratios over the parameter ranges:

14.7 psi < pressure < 1500 psi, 1 ft/sec < V_s < 7 ft/sec, and $0.0005 < X < 0.10$:

$$\frac{V_g}{V_L} = 0.63\,(Fr)^{0.4}\left[\frac{X}{1 - X}\left(\frac{\rho_L}{\rho_g}\right)\right]^{0.2} \quad . \qquad \text{(D-1)}$$

It should be noted that the diameter D of the flow channels was not changed extensively; hence, the variation of the Froude number was due primarily to the varying mass velocity. Whether or not the data taken on widely differing diameter channels would fall on the same family of curves derived from this study is uncertain. It is expected that for very low flow rates and large equivalent diameters this correlating technique would not hold and large deviations would be encountered. A number of investigators have reported that wall effects on the rise of vapor bubbles in pipes diminish

when a certain diameter of pipe is reached. Analysis of upflow slip ratio data has shown that the diameter effect decreases rapidly above D = 2 in. Marchaterre[23] has suggested that for a channel diameter greater than 3 in. the Froude number for this type of correlation should be evaluated with D = 3 in.

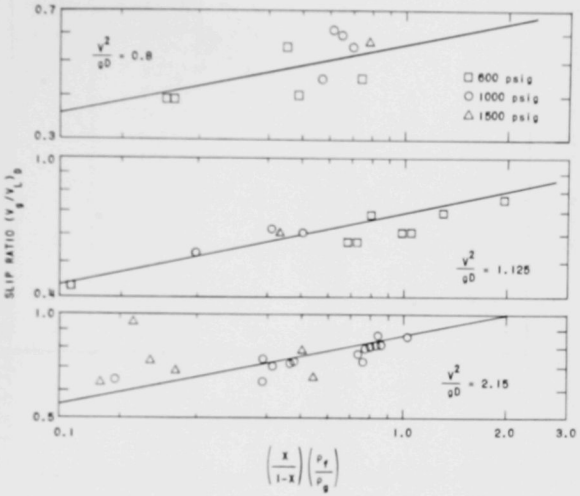

Fig. D-10. Correlation of Downflow Slip Ratio

A comparison of Eq. (D-1) with the high-pressure data is shown on an error plot in Fig. D-11. Over 85% of the calculated values fall within ±20% of the measured data. For slip-ratio data such agreement is considered quite good.

The correlation did not fit the air-water data very well. The correlation predicted values that were too low for the set of data taken in the lower downcomer and values that were too high for the set taken in the upper downcomer.

The air-water data taken in the upper downcomer are thought to be somewhat in error. Visual observation has shown that not all air carried under in the upper downcomer is actually entrained. Some of the air escapes due to coalescence. As a result, the void fraction in this region, which is derived from the differential pressure-drop measurement, is artificially high. This high void fraction when used in conjunction with the measured mixture quality in the continuity equation to calculate the slip ratios yields abnormally low values of slip ratio. If this postulation is true, it could well account for the large scatter of the data in the empirical carryunder correlation described previously in Section VI.

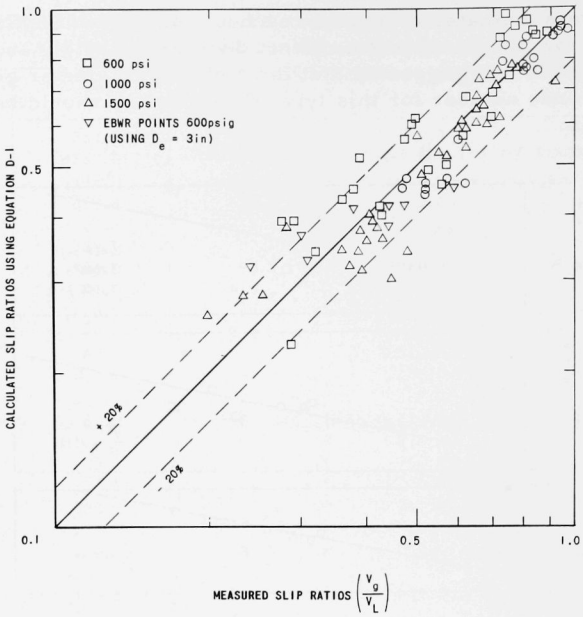

Fig. D-11. Comparison between the High Pressure Downflow Slip Ratio Data and the Correlation

The pressure effect in Eq. (D-1) is inherent in the term $[X\rho_L/(1-X)\rho_g]^{0.2}$. A first glance indicates that the slip ratio decreases with increasing pressure. However, upon closer inspection, the opposite effect is evident. For a fixed void volume fraction, the mixture quality increases more sharply with pressure than the ρ_L/ρ_g decreases. Hence the product $[X/(1-X)]/(\rho_L/\rho_g)$ would tend to increase and thus yield higher slip ratios with increasing pressure and constant void fraction.

Equation (D-1) is recommended for computing the slip ratio in downflow for steam-water mixtures over the parameter range specified. For flow channels of large diameter, it is suggested that D = 3 in. be used for calculating the Froude number. A few data points obtained from a 3-ft-diameter system were calculated in this manner, and they are shown in Fig. D-11. As can be seen, the agreement between the measured and predicted values is good.

A tabulation of data is presented in Table D-1 through D-III.

Table D-I

600-psi DOWNFLOW SLIP DATA

Run No.	X	V_s	V_T	V_g/V_L
D-49	0.0422	0.985	5.125	0.3894
D-50	0.0356	0.9825	4.7236	0.3604
D-51	0.0293	0.945	4.311	0.3153
D-52	0.0194	2.578	5.876	0.5753
D-53	0.02583	2.578	6.752	0.608
D-54 A	0.0330	2.86	7.72	0.7464
D-54 B	0.0309	2.89	7.662	0.718
D-55	0.0348	2.834	7.99	0.738
D-56	0.0327	2.95	7.82	0.7613
D-57	0.0316	3.018	7.76	0.771
D-58	0.0305	3.203	7.86	0.806
D-59	0.0378	3.38	7.71	0.830
D-60	0.0267	3.52	7.826	0.833
D-61	0.0263	3.635	7.76	0.8855
D-62	0.0182	2.49	5.54	0.5623
D-63	0.0271	2.49	6.66	0.6192
D-64	0.0339	2.48	7.108	0.6995
D-65	0.0497	2.49	8.058	0.8695
D-66	0.0277	4.51	8.904	1.087
D-67	0.0207	4.185	8.081	0.8427
D-68	0.0187	4.32	7.883	0.8606
D-69	0.0553	1.415	6.611	0.5921
D-70	0.0401	1.388	6.252	0.4232
D-71	0.0294	1.33	5.526	0.357
D-15	0.0030	2.41	3.04	0.4251
D-16	0.00654	2.42	3.55	0.525
D-17	0.0079	2.74	4.45	0.4712
D-18	0.01097	2.74	5.06	0.4864
D-20	0.0008	2.75	3.3	0.149
D-21	0.0119	2.77	5.27	0.494
D-22	0.0214	2.41	5.23	0.696
D-23	0.0232	1.58	5.30	0.3774
D-24	0.0240	1.32	5.39	0.2964
D-25	0.0330	1.24	4.92	0.4273
D-26	0.0168	1.45	4.80	0.2752
D-30	0.0008	1.57	1.73	0.2864
D-31	0.02355	1.608	4.902	0.4381
D-32	0.0163	1.608	4.614	0.3295
D-33	0.01485	1.582	4.820	0.2737
D-34	0.01408	1.558	4.4705	0.2878
D-35	0.01754	1.309	4.732	0.2536
D-36	0.02138	1.322	4.579	0.3325
D-37	0.02049	1.35	4.858	0.2990
D-38	0.01626	1.309	4.404	0.2596
D-39	0.01434	1.281	4.074	0.2477
D-40	0.00797	1.636	3.864	0.219
D-41	0.00714	1.615	3.2126	0.2700
D-42	0.01587	1.266	3.698	0.312
D-43	0.00911	1.35	3.211	0.2477
D-44	0.00554	1.992	3.046	0.39124
D-45	0.00589	2.01	5.629	0.396
D-46	0.01203	2.03	3.71	0.5467
D-47	0.01301	2.01	5.312	0.2983
D-48	0.0201	1.99	5.298	0.4585

Table D-II

1000-psi DOWNFLOW SLIP DATA

Run No.	X	V_s	V_T	V_g/V_L
D-72	0.0197	2.497	4.133	0.623
D-73	0.0231	2.845	4.438	0.856
D-74	0.01892	3.153	4.824	0.7389
D-75	0.0203	3.01	4.79	0.711
D-76	0.0192	2.775	4.63	0.5955
D-77	0.0243	2.467	4.496	0.6148
D-78	0.0310	2.15	4.494	0.5961
D-79	0.0245	2.75	6.217	0.6428
D-80	0.01925	3.152	9.260	0.6387
D-81	0.0228	3.147	5.250	0.7078
D-82	0.0278	2.705	5.002	0.6842
D-83	0.0335	2.171	5.071	0.527
D-84	0.0058	3.718	4.292	0.7630
D-85	0.0038	3.745	4.14	0.727
D-86	0.00275	4.133	4.681	0.4214
D-87	0.0071	3.12	3.811	0.6599
D-88	0.0212	2.89	4.69	0.705
D-89	0.2074	2.281	5.177	0.4511
D-90	0.0288	2.281	4.57	0.6014
D-91	0.0406	1.665	4.659	0.4797
D-92	0.0362	1.642	4.29	0.4726
D-93	0.033	1.616	3.775	0.518
D-94	0.0398	1.595	4.17	0.5203
D-95	0.0459	1.57	4.5	0.523
D-96	0.0582	1.50	4.52	0.6237
D-97	0.062	1.499	5.022	0.572
D-98	0.0289	4.161	6.76	0.970
D-99	0.0294	4.33	7.17	0.9383
D-100	0.01995	4.477	6.763	0.808
D-101	0.0203	4.224	6.642	0.7379
D-102	0.025	4.224	6.642	0.9083
D-103	0.0293	4.118	6.82	0.934
D-104	0.0325	4.118	7.12	0.9361
D-105	0.0352	3.147	6.25	0.751
D-106	0.0398	3.062	6.16	0.8516
D-107	0.0376	3.147	6.30	0.792
D-108	0.0402	3.147	6.411	0.8185
D-109	0.0395	3.147	6.4	0.805
D-110	0.0369	3.326	6.89	0.7253
D-111	0.0415	3.147	6.58	0.8065
D-112	0.0471	3.147	6.82	0.8601

Table D-III

1500-psi DOWNFLOW SLIP DATA

Run No.	X	V_s	V_T	V_g/V_L
126	0.0103	4.081	4.517	1.03
127	0.0152	3.341	4.486	0.9685
128	0.0173	3.523	4.432	0.7228
129	0.0231	3.046	4.217	0.6504
130	0.0196	4.375	5.142	1.21
131	0.0222	3.970	3.852	0.9266
132	0.0330	3.053	4.72	0.6598
133	0.0103	3.9	4.56	0.6530
134	0.0125	3.505	4.26	0.6244
135	0.0204	3.25	4.30	0.681
136	0.0282	2.898	4.39	0.598
137	0.0389	2.567	4.39	0.6038
138	0.0602	2.035	4.466	0.5686
139	0.0787	1.693	4.694	0.5107
140	0.0348	3.887	5.842	0.7585
141	0.0452	3.594	5.903	0.780
142	0.0499	3.24	5.984	0.657
143	0.0114	1.747	2.187	0.4835
144	0.0186	0.736	2.545	0.4299
145	0.0243	1.718	2.783	0.4258
146	0.0624	1.704	3.014	0.9175
147	0.0838	1.693	3.714	0.8121
148	0.0335	2.875	4.585	0.6185
149	0.0560	2.90	5.704	0.6497
150	0.0146	2.983	3.84	0.5546
151	0.0241	2.983	4.24	0.6211
152	0.0221	2.994	4.437	0.4967
153	0.0379	2.996	4.85	0.6739
154	0.0536	3.004	5.548	0.708
155	0.0617	3.018	5.942	0.7195
156	0.0684	3.076	6.54	0.690
157	0.0652	3.099	6.53	0.6672
158	0.0723	3.081	6.76	0.6913
159	0.0762	3.086	6.915	0.705
160	0.0198	1.216	1.821	0.4289
161	0.0295	1.216	2.073	0.457
162	0.0431	1.208	2.26	0.5465
163	0.0394	1.216	2.627	0.3739
164	0.0525	1.216	3.069	0.3850
165	0.0595	1.216	3.489	0.359
166	0.0704	1.216	3.654	0.400
167	0.0827	1.216	4.167	0.3938
168	0.1051	1.216	4.89	0.4115
169	0.1118	1.216	5.19	0.408
170	0.1227	1.218	5.792	0.3947
171	0.0509	1.438	4.804	0.285
172	0.0548	0.968	3.320	0.253
173	0.0366	0.968	2.94	0.198
174	0.0371	1.209	2.46	0.3941
175	0.0248	1.209	2.612	0.232

BIBLIOGRAPHY

1. O. Miyagi, The Motion of Air Bubbles Rising in Water, Technology Reports of the Tohoku Imperial University, 5, No. 3 (1925); Phil. Mag., (6), 50, 112-139, (1925).

2. H. H. Hooker and G. F. Popper, A Gamma-ray Attenuation Method for Void Fraction Determination in Steam-Water Mixtures, ANL-5766, (Nov. 1958).

3. M. Petrick, Two-phase Air-Water Flow Phenomena, ANL-5787 (March 1958).

4. Tables of the Incomplete Γ Function, Edited by K. Pearson, University of London, University College, London, 2nd Edition (1934).

5. S. G. Bankhoff, A Variable Density Single-fluid Model for Two-phase Flow with Particular Reference to Steam-Water Flow, Trans. ASME 82 C (1960).

6. Isaac Newton, Mathematical Principles of Natural Philosophy, Book II.

7. G. G. Stokes, Mathematical and Physical Papers (1901), Trans. Cambridge Phil. Soc., 9 Part II (1851).

8. H. S. Allen, The Motion of a Sphere in a Viscous Fluid, Phil. Mag., (5) 50, 323-338, 519-534 (1900).

9. G. Martin, A Treatise on Chemical Engineering, Lockwood and Son, London, Ch 30.

10. I. S. Pavlushenko, Free Motion of Individual Particles in Stationary Unlimited Medium, Journal of Applid Chem. of the USSR, 29 901 (1956).

11. Byrn, Forschungsgebeite der Ingineur Wissenschaften, 4, No. 1, 27 (1933).

12. Luchsinger, Kolloid Zeitschrift, 81, 180 (1937).

13. M. O'Brien and E. J. Gosline, Velocity of Large Bubbles in Vertical Tubes, Ind. Eng. Chem., 27, 1436 (1935).

14. B. Rosenberg, NDR-727 (1950).

15. D. W. von Krevelen and P. J. Hoftijzer, Studies of Gas Bubble Formation - Calculation of Interfacial Area and Bubble Contactors, Chem. Eng. Progress, 46, 29 (1950).

16. R. M. Davies and G. Taylor, The Mechanics of Large Bubbles Rising through Extended Liquids and through Liquids in Tubes, Proc. Roy. Soc., A200, 375 (1950).

17. M. Jakob, Heat Transfer, John Wiley and Sons, Inc., New York, p. 631.

18. F. N. Peebles and H. J. Garber, Studies on the Motion of Gas Bubbles in Liquid, Chem. Eng. Progress, 49, No. 2, 88 (1953).

19. R. W Haywood, G. A. Knights, G. E. Middleton, and J. R. S. Thorn, Experimental Study of the Flow Conditions and Pressure Drop of Steam-Water Mixtures at High Pressures in Heated and Unheated Tubes. Paper presented at the Institution of Mechanical Engineers, March, 1961.

20. K. Schwarz, 1954 V.D.I. Forschungs B.20, No. 445, P. 1, Investigations of the Distribution of Specific Gravity, The Water and Steam Velocities and the Frictional Pressure Drop in Vertical and Horizontal Boiler Tubes, VDI Forschung auf dem Gebiete des Ingenieuwesens.

21. G. F. Popper, Lecture Notes on In-core Instrumentation for the Measurement of Hydrodynamic Parameters in Water-cooled Reactors, ANL-6452 (Nov 1961).

22. S. S. Kutateladze, Heat Transfer in Condensation and Boiling, AEC-tr-3770 (Aug 1959).

23. J. F. Marchaterre and B. M. Hoglund, Velocity Ratios in Vertical Two-phase Flow, Nucleonics, 20, No. 8 (Aug 1962).